

JOINT TRANSPORTATION RESEARCH PROGRAM

INDIANA DEPARTMENT OF TRANSPORTATION
AND PURDUE UNIVERSITY



Control Guidelines for Aggregate Drainage Layers and Evaluation of In-Situ Permeability Testing Methods for Aggregates



**Luis Garzon-Sabogal, Amy Getchell, Peter J. Becker,
Philippe Bourdeau, Marika Santagata**

RECOMMENDED CITATION

Garzon-Sabogal, L., Getchell, A., Becker, P. J., Bourdeau, P. L., & Santagata, M. (2024). *Control guidelines for aggregate drainage layers and evaluation of in-situ permeability testing methods for aggregates* (Joint Transportation Research Program Publication No. FHWA/IN/JTRP-2024/28). West Lafayette, IN: Purdue University. <https://doi.org/10.5703/1288284317769>

AUTHORS

Luis Garzon-Sabogal

Graduate Research Assistant
Lyles School of Civil and Construction Engineering
Purdue University

Amy Getchell

Graduate Research Assistant
Lyles School of Civil and Construction Engineering
Purdue University

Peter J. Becker, PhD, PE

Research Engineer
Indiana Department of Transportation
Division of Research and Development

Philippe L. Bourdeau, PhD

Emeritus Professor of Civil Engineering
Lyles School of Civil and Construction Engineering
Purdue University

Marika Santagata, PhD

Professor of Civil Engineering
Lyles School of Civil and Construction Engineering
Purdue University
(765) 494-0697
mks@purdue.edu
Corresponding Author

JOINT TRANSPORTATION RESEARCH PROGRAM

The Joint Transportation Research Program serves as a vehicle for INDOT collaboration with higher education institutions and industry in Indiana to facilitate innovation that results in continuous improvement in the planning, design, construction, operation, management and economic efficiency of the Indiana transportation infrastructure. <https://engineering.purdue.edu/JTRP/index.html>

Published reports of the Joint Transportation Research Program are available at <http://docs.lib.purdue.edu/jtrp/>.

NOTICE

The contents of this report reflect the views of the authors, who are responsible for the facts and the accuracy of the data presented herein. The contents do not necessarily reflect the official views and policies of the Indiana Department of Transportation or the Federal Highway Administration. The report does not constitute a standard, specification or regulation.

ACKNOWLEDGEMENTS

Several people and organizations played a role in making this project a success. In particular, the authors would like to acknowledge the following contributors:

- US Aggregates of Delphi, IN, for donating the aggregate used to construct the experimental strips at the SBRITE site;
- Propex Geosolutions for donating the geotextile used at the SBRITE site;
- Chad Clark and Brent Winter of Irving Materials, Inc. for providing materials and support for casting the pervious concrete pads;
- The Indianapolis office of Terracon for the support in conducting the nuclear density testing programs;
- Clint Bryant of INDOT's Crawfordsville District for supplying the field equipment used to construct the strips at the SBRITE site;
- Ross Bucher, Dustin Leslie, and Brent Richter of INDOT R&D for help during construction and testing of the SBRITE strips;
- Ramon Delreal of BF&S and the City of West Lafayette for providing access to the Cherry Lane construction site;
- Don Thornton and Kelly Jacob of INDOT who facilitated access to the Bloomington construction site;
- Jacob Cunningham and Chris Allen of Parsons who provided access and worked with the research team at the I-65 construction site; and
- José Capa Salinas, a Purdue Civil Engineering PhD student, who took drone pictures of the experimental strips at the SBRITE site.

Graduate students Movey Sasar, Matthew Halverson, and Alex Long contributed to the research at various stages of the project. Additional graduate students—Kanika Gupta, SungSoo Park, and Hala El Fil—lent a hand during testing at the SBRITE site.

Finally, the project benefited from the involvement and dedication of the following undergraduate students: Elise Tessero, Gavin Baisa, Alex Landyshev, Caroline (Mimi) Wadley, Claire Middendorf, and Clay Jarosinsky.

TECHNICAL REPORT DOCUMENTATION PAGE

1. Report No. FHWA/IN/JTRP-2024/28	2. Government Accession No.	3. Recipient's Catalog No.	
4. Title and Subtitle Control Guidelines for Aggregate Drainage Layers and Evaluation of In-Situ Permeability Testing Methods for Aggregates		5. Report Date September 2024	
		6. Performing Organization Code	
7. Author(s) Luis Garzon-Sabogal, Amy Getchell, Philippe L. Bourdeau, Peter J. Becker, and Marika Santagata		8. Performing Organization Report No. FHWA/IN/JTRP-2024/28	
9. Performing Organization Name and Address Joint Transportation Research Program Hall for Discovery and Learning Research (DLR), Suite 204 207 S. Martin Jischke Drive West Lafayette, IN 47907		10. Work Unit No.	
		11. Contract or Grant No. SPR-4327	
12. Sponsoring Agency Name and Address Indiana Department of Transportation (SPR) State Office Building 100 North Senate Avenue Indianapolis, IN 46204		13. Type of Report and Period Covered Final Report	
		14. Sponsoring Agency Code	
15. Supplementary Notes Conducted in cooperation with the U.S. Department of Transportation, Federal Highway Administration.			
16. Abstract <p>This project examined the use of the light weight deflectometer (LWD) and the air permeameter test (APT) for control of the state of compaction and hydraulic conductivity of aggregate drainage layers. The investigation included an extensive program of LWDs, APTs, and nuclear density tests on two testing strips constructed at an experimental site—one on an untreated subgrade and the other on cement-treated subgrade. The project also included additional field tests at three construction sites in Indiana and a laboratory testing program for calibration and validation of the field data. Statistics and correlation studies of the collected data are presented and serve as a basis for assessing the testing methods and the influence of statistical sample size on the reliability of QA/QC outputs. The main outcomes address the spatial variability in the measured properties, the evaluation of materials and methods used to construct the strips, and the methods used for characterizing the layers. These findings highlight opportunities for assessing uncertainty, as measured by the dispersion of the data as part of a QA/QC campaign, and for reformulating guidelines in probabilistic terms.</p>			
17. Key Words pavement drainage layers, aggregates, hydraulic conductivity, compressibility, compaction, dry density, aggregate segregation, light weight deflectometer, air permeameter test, image analysis, subgrade, cement treated soils		18. Distribution Statement No restrictions. This document is available through the National Technical Information Service, Springfield, VA 22161.	
19. Security Classif. (of this report) Unclassified	20. Security Classif. (of this page) Unclassified	21. No. of Pages 105 including appendices	22. Price

EXECUTIVE SUMMARY

Introduction

This research project evaluated methods for measuring performance parameters of aggregate drainage layers in-situ to provide INDOT guidance for developing performance-based specifications for these layers. The work focused on two particular experimental methods: the light weight deflectometer (LWD) and the air permeameter test (APT).

Findings

The work performed included the following.

- An extensive field-testing program conducted on two experimental testing strips constructed at Purdue University's SBRITE facility. The strips were comprised of a layer of Indiana #53 (IN #53) constructed over either the compacted natural soil or the cement-treated subgrade. Testing on the aggregate was performed with high spatial density on a 3 ft × 3 ft grid and included LWDs, APTs, nuclear density tests, and imaging of the aggregate surface.
- Similar testing programs at three construction sites in Indiana. At one of the sites additional APTs were performed on two bound drainage layers: a cement treated base and an open graded asphalt base.
- An extensive program of constant and falling head laboratory tests and APTs on laboratory prepared samples of IN #53 and on pervious concrete. The latter was used as model material.

Statistical analyses of the data collected at the SBRITE site, enabled by the large size of the statistical sample, showed that the parameters measured exhibited different dispersion, as measured by the coefficient of variation (CV). Of the data collected on the aggregate layers, the greatest dispersion was observed in the hydraulic conductivity (k) values, followed by the LWD deflections, and the dry density. At all sites, the range of the k data exceeded a few thousand ft/day.

The observed spatial variability in the properties of the compacted aggregate can be, at least in part, ascribed to material heterogeneity, produced by segregation, which in this work was quantified through a parameter termed median feature size (MFS) extracted from images of the aggregate surface. Linear correlation analyses demonstrate a strong correlation between the MFS and the in-situ hydraulic conductivity (k), supporting the hypothesis that the MFS parameter is an indicator of local material heterogeneities that drive variability in hydraulic conductivity at the local scale.

Cement-treatment of the subgrade reduced LWD deflections, including those measured on the overlying aggregate layer, facilitated compaction of the aggregate, and promoted more homogenous conditions, both in the subgrade and in the overlying aggregate.

Based on APT and nuclear density tests, coarse aggregates such as IN #53 appear to be valid options as drainage layers. The compaction procedure (static passes, followed by vibratory and additional static passes) employed on the strips promoted adequate relative compaction, and the k values measured after

compaction demonstrate their suitability for exercising a drainage function. Laboratory tests indicate, however, that variation in the percentage of fines and material heterogeneity caused by segregation may lead to lower values of k . Laboratory hydraulic conductivity tests on compacted IN #53 also suggest that the applicability of Darcy's law to this material may be limited to small gradients, and that the aggregate may be susceptible to internal erosion.

Although both LWD deflections and nuclear density measurements are being used in practice for quality assessment of compacted subbase granular layers, across both strips at the SBRITE site the two measurements were not found to be strongly correlated. Moreover, the LWD data showed significantly greater dispersion than the ρ_d measurements. For the untreated strip, measurements performed on the aggregate layer were found to be controlled by deformations in the underlying subgrade, with weak information provided on the state of compaction of the aggregate layer.

The sturdy and compact design of the APT apparatus and the simplicity of operation are well suited for rapid and frequent measurements in the field. Moreover, extensive testing performed as part of this project demonstrates that measurements using the APT can be consistently performed on compacted IN #53 aggregate. However, in its current configuration, it cannot be reliably used to test materials with higher k , such as Indiana #8.

Values of saturated hydraulic conductivity derived from the APT are highly sensitive to the degree of saturation of the aggregate, and the correction for the in-situ degree of saturation (S) leads to an increase in the value of k that exceeds an order of magnitude for S greater than ~ 0.65 .

Concurrent measurements of the degree of saturation are therefore needed to map spatial variability of the in-situ degree of saturation.

Stochastic analysis of the LWD data collected at the experimental SBRITE site on both the subgrade and the aggregate layer demonstrates that small statistical samples are generally not reliable for quality control, and that the estimate of the population mean based on such samples carries great uncertainty. The degree of uncertainty is dependent on the distribution of the population and increases for datasets characterized by greater variability.

Moreover, information pertaining to local problematic areas, which are often the source of damage in pavement systems, is not captured when utilizing QA/QC criteria based on the mean of a sample, compromising efforts invested in quality assessment. These observations highlight the importance during a quality assessment campaign of assessing uncertainty evidenced by the dispersion in the data.

Samples of the nonwoven geotextile fabric used as a separator layer over a portion of the two SBRITE strips exhumed following the completion of the testing program showed significant damage, evidence that the geotextile did not survive and could, therefore, not fulfill its intended functions as separator/filter.

Implementation

Based on the work performed, the following primary recommendations for implementation are provided.

- Under conditions similar to those encountered at the SBRITE site, cement-treatment of the subgrade is recommended.
- Construction methods to limit segregation of aggregates in the field should be enforced and aggregate compaction

should be performed using vibratory rollers, with early and final passes in static mode.

- The use of LWD deflection-based criteria is recommended for QA/QC of untreated and cement-treated subgrades and of aggregate layers constructed on cement-treated subgrade.
- The LWD is not recommended for QA/QC of aggregate layers constructed on untreated subgrades.
- In the current state of development, implementation of the APT for QA/QC is not recommended due to issues with the method used to account for the degree of saturation, and the extensive testing required for mapping this property in the field.
- The use of rapid non-destructive tests (e.g., LWD) that can be performed in large number and at high spatial density is recommended for QA/QC.
- Uncertainty as measured by the dispersion of the data should be assessed as part of a QA/QC campaign, and guidelines formulated in probabilistic terms.

- Consideration should be given to assessing material segregation as part of QA/QC protocols for aggregate layers.
- A higher-class geotextile product compared to the one used in this project is recommended to provide separation and filtration functions.

The study also highlighted the following areas where additional research is warranted to further support INDOT's transition towards performance-based specifications:

- investigation of susceptibility of IN #53 and of other candidate aggregates to segregation and internal erosion,
- advancement of image analysis method for segregation quality control,
- improvement in data interpretation and further validation of air permeameter test (APT),
- advancement of LWD test interpretation, and
- development of risk-informed QA/QC.

TABLE OF CONTENTS

1. INTRODUCTION	1
1.1 Project Background and Problem Statement	1
1.2 Project Scope and Research Objectives	1
1.3 Activities and Organization of Report	1
2. BACKGROUND OF TESTING METHODS.	2
2.1 Introduction	2
2.2 Air Permeameter Test	2
2.3 Light Weight Deflectometer (LWD).	8
3. FIELD TESTING AT SBRITE SITE.	10
3.1 Introduction	10
3.2 Construction of Testing Strips	11
3.3 Testing Program.	13
3.4 Results	15
4. FIELD TESTING AT CONSTRUCTION SITES.	29
4.1 Introduction	29
4.2 Site 1: Cherry Lane, West Lafayette, IN.	29
4.3 Site 2: SR 46, Bloomington, IN.	34
4.4 Site 3: I-65, Lebanon, IN	38
4.5 Observations on Compound Field Data and Comparisons Between Sites	45
5. LABORATORY TESTING PROGRAM	56
5.1 Introduction	56
5.2 Air Permeameter Tests on Aggregate Compacted in Large Crates.	56
5.3 Hydraulic Conductivity Tests on IN #53 Aggregate	57
5.4 Tests on Pervious Concrete Pads	63
6. SUMMARY AND CONCLUSIONS	70
6.1 Overview of Work	70
6.2 Summary and Conclusions	70
6.3 Recommendations	74
REFERENCES	76
APPENDICES	
Appendix A. Data Sheet for Geotextile Used at SBRITE Site	78
Appendix B. Plots for Correlation Analyses of SBRITE Data	78
Appendix C. Photos Documenting Geotextile Damage	78

LIST OF TABLES

Table 2.1 Maximum LWD deflection criteria for compacted No. 53 aggregate per INDOT Standard Specification 203.23	9
Table 3.1 Statistics of data from SBRITE site	16
Table 3.2 Results of correlation analyses and bootstrap resampling	21
Table 3.3 Assessment of layers of cement-treated strip based on six different acceptance criteria	24
Table 3.4 Statistics of data from tests on first aggregate lift SBRITE site	25
Table 3.5 Results of second set of correlation analyses (correlations with $ r > 0.5$ and $p < 0.05$)	25
Table 3.6 Summary statistics from single day repeat measurements	26
Table 4.1 Summary of field-testing program at Sites 1–3 (number of tests performed does not include repeat measurements at the same testing location)	30
Table 4.2 Results of sand cone tests at Site 1	32
Table 4.3 Comparison of #53 APT and LWD data before and after compaction	33
Table 4.4 Results of sand cone tests at Site 2	40
Table 4.5 Effect of degree of saturation on value of k derived from APT measurements at select locations at Site 2	41
Table 4.6 Result summary of nuclear density tests performed on Pads 1–5 at Site 3 (numbers represent mean values derived from nine tests performed on each pad)	46
Table 4.7 Key statistical indicators derived from APT measurements of the k of IN #53 at Site 3	48
Table 4.8 Key statistics derived from APT measurements on open graded asphalt and cement-treated permeable base at Site 3	53
Table 4.9 Key statistics derived from repeat APT measurements at testing locations on open graded asphalt and cement-treated permeable base at Site 3	54
Table 4.10 Summary of statistical indicators (mean, CV (%), minimum and maximum values, and range) of data from Sites 1–3 and from SBRITE strips	55
Table 5.1 Crate samples tested using APT	57
Table 5.2 Summary of APT data from tests on Crate I (compacted IN #53)	58
Table 5.3 Summary of APT data for Crate II (two layers of IN #53)	58
Table 5.4 Summary of APT data for Crate III (compacted IN #53 over compacted IN #43)	58
Table 5.5 Summary of APT data for Crate IV (compacted IN #8)	59
Table 5.6 Summary of APT data for Crate V	59
Table 5.7 Summary of tests performed in large permeameter	63
Table 5.8 Summary of APT data from tests performed on a 2 ft × 2 ft pervious concrete pad in March 2022	66
Table 5.9 Summary of APT data from tests performed on a 1.4 ft × 1.4 ft pervious concrete pad in March 2022	67
Table 5.10 Summary of APT data from tests performed on a 2 ft × 2 ft pervious concrete pad in October 2023	68

LIST OF FIGURES

Figure 2.1 Conceptual schematic of APT apparatus	3
Figure 2.2 (a) APT apparatus mounted on cart, (b–c) details of connections inside cylinder housing components (from White et al., 2014); (b) APT mounted on cart; (c) details of connections inside cylinder housing; and (d) view of base plate	4
Figure 2.3 (a) Setup for calibration of orifices, and (b) calibration curves for orifices B and C	6
Figure 2.4 Illustration of the derivation of the saturated hydraulic conductivity from the APT pressure readings	7
Figure 2.5 Results of parametric study showing influence of (a) Brooks-Corey parameter λ , and (b) degree of saturation, S , and residual degree of saturation, S_r , on calculation of saturated hydraulic conductivity	7
Figure 2.6 Typical light weight deflectometer testing setup	8
Figure 2.7 Example surface deflection response measure by LWD (note that output deflection values occur at the initial local maximum)	8
Figure 2.8 LWD testing locations for compacted aggregate construction acceptance in accordance with INDOT Standard Specification 203.23 (construction width \geq to 8 ft)	9
Figure 2.9 LWD testing locations for compacted aggregate construction acceptance in accordance with INDOT Standard Specification 203.23 (construction width $<$ 8 ft)	9
Figure 2.10 Modulus degradation curve	10
Figure 3.1 Location of SBRITE center in West Lafayette, IN	11
Figure 3.2 Equipment and methods used for subgrade modification: (a–b) site preparation; (c–d) water content control and mixing of natural soil on untreated strip; (e–f) cement-slurry treatment of subgrade of treated strip; (g) leveling; and (h–i) compaction of the subgrade of both strips with pad-foot drum and smooth drum roller	12
Figure 3.3 Aerial view and view from the east end of site of untreated (north) and cement-treated (south) strips after marking the testing grid on finished subgrade	12
Figure 3.4 (a) Methods used for the construction of aggregate layers and the placement of geotextile and equipment (note: stakes used for marking testing grid), (b) mixing, (c–d) placement, (e) leveling, and (f) compaction of aggregate	12
Figure 3.5 (a) Aerial view of finished test strips (note: nonwoven geotextile placed between subgrade and overlying subbase in eastern portion of strips). (b) Particle size distribution of IN #53 aggregate used to construct subbase. Dashed lines identify the IN #53 limits based on INDOT 904.03	13
Figure 3.6 Map of testing program on (a) untreated, (b) cement-treated strips, and (c) schematic of testing apparatus	14
Figure 3.7 (a) Schematic of the structure of the two testing strips, and (b–d) maps of aggregate layer thickness	15
Figure 3.8 Histograms of aggregate and subgrade LWD_L data for (a) untreated, and (b) cement-treated strip	17
Figure 3.9 Spatial distribution of LWD_L mean deflection data from tests on subgrade of (a–b) untreated strip, and (c) cement-treated strip. Note: different scale in leftmost plot	18
Figure 3.10 Spatial distribution of data from tests on aggregate layer of cement-treated and untreated strip: (a) LWD_L mean deflections, (b) degree of saturation, S , from nuclear density tests, (c) saturated hydraulic conductivity, k , from APT tests, and (d) median feature size, MFS	19
Figure 3.11 Spatial distribution of uncorrected and corrected data of saturated hydraulic conductivity, k , from APT tests: (a–b) untreated, and (c–d) cement-treated strip	20
Figure 3.12 Schematic of bootstrapping procedure followed to generate the data shown in Table 3.2	20
Figure 3.13 Result summary of linear correlation analyses	21
Figure 3.14 Relationship between in-situ S and $\log k$ of aggregate layer (k in ft/day). (a) All data for two strips; (b–e) data for specific MFS intervals (empty and full symbols denote data for untreated and cement-treated strip, respectively); and (f–g) aggregate MFS distributions for untreated and cement-treated strip	22
Figure 3.15 Effect of sample size on average characterization of strips	23
Figure 3.16 Effect of sample size on the correct assessment according to different criteria of (a–f) aggregate, and (g–l) subgrade of cement-treated strip	24
Figure 3.17 (a) Locations, and (b) results of single day repeat measurements	26
Figure 3.18 Locations where repeat measurements were performed between August and December 2020	27

Figure 3.19 Results of measurements performed between August and December 2020 at select locations on (a) untreated, and (b) cement-treated strip	27
Figure 3.20 Sampling trench on untreated strip: (a) before, and (b) after exhuming the geotextile samples. (c) Exhumed geotextile sample at one location on same strip, and (d) detail of perforation. Markers shown in part (a) identify locations for damage inventory	28
Figure 3.21 Installation of pressure cells: (a) excavation of housing for pressure cell in cement treated subgrade; (b) leveling of the paver sand following hand compaction with a tamper; (c) placement and leveling of the pressure cell; and (d) leveling of the overlying sand	28
Figure 3.22 (a) Placement of aggregate on strip (black arrows identify position of two pressure cells); (b) compaction of aggregate over one of the pressure cells; and (c) cart with power supply and data acquisition equipment	29
Figure 3.23 Examples of signal collected at one of the pressure cells during (a) a static pass, and (b–c) a vibratory pass	29
Figure 4.1 Site 1 location	30
Figure 4.2 Construction stages at Site 1: (a) placement, (b) spreading and leveling, and (c) compaction of aggregate	31
Figure 4.3 Testing at Site 1: (a) picture of working area, (b) mesh used to mark testing locations, and (c) testing grid and overview of testing program on compacted IN #53	31
Figure 4.4 APT orifice B results from tests on IN #53 aggregate at Site 1: (a) tests performed, (b) spatial variation, (c) histogram, and (d) descriptive statistics	32
Figure 4.5 (a) Spatial distribution, (b) histogram, and (c) descriptive statistics of LWD_L deflection data collected on IN #53 at Site 1	34
Figure 4.6 (a) Spatial distribution, (b) histogram, and (c) descriptive statistics of LWD_S deflection data collected on IN #53 at Site 1	35
Figure 4.7 MFS data for Site 1: (a) spatial distribution, (b) histogram, and (c) images corresponding to minimum, median, and maximum values (size of images $\sim 31\text{ cm} \times 20\text{ cm}$)	36
Figure 4.8 (a) APT, (b) LWD_L , and (c) LWD_S data from tests on IN #8 aggregate layer at Site 1	37
Figure 4.9 Correlation between deflections derived from LWD_L tests performed on IN #8 layer and on the underlying IN #53 layer at Site 1	37
Figure 4.10 Location of Site 2	38
Figure 4.11 Construction stages at Site 2: (a) placement, and (b) spreading and leveling of aggregate	38
Figure 4.12 (a) Picture of working area, and (b) overview of testing program at Site 2	39
Figure 4.13 APT orifice B results from tests on IN #53 at Site 2: (a) tests performed, (b) spatial variation, (c) histogram, and (d) descriptive statistics of measurements	40
Figure 4.14 Impact of orifice C calibration on values of k derived from APT measurements	41
Figure 4.15 (a) Spatial distribution, (b) histogram, and (c) descriptive statistics of LWD_L deflection data collected on IN #53 at Site 2	42
Figure 4.16 (a) Spatial distribution, (b) histogram, and (c) descriptive statistics of LWD_S deflection data collected on IN #53 at Site 2	43
Figure 4.17 MFS data for Site 2: (a) spatial distribution, (b) histogram, and (c) images corresponding to minimum, median, and maximum values (size of images $\sim 31\text{ cm} \times 20\text{ cm}$)	44
Figure 4.18 Location of Site 3	45
Figure 4.19 (a) Location of testing pads at Site 3 and testing program for (b) Pad 1, (c) Pad 2, (d) Pad 3, (e) Pad 4, and (f) Pad 5	45
Figure 4.20 Nuclear density results for IN #53 at Site 3	46
Figure 4.21 APT results for Site 3: spatial distribution and histograms for (a–b) Pad 1, (c–d) Pad 2, (e–f), Pad 3, (g–h), Pad 4, and (i–j) Pad 5	47
Figure 4.22 LWD_L results from tests on cement-treated subgrade at Site 3: spatial distribution and histograms for (a–b) Pad 1, (c–d) Pad 2, (e–f) Pad 3, (g–h) Pad 4, and (i–j) Pad 5	48
Figure 4.23 LWD_L results from tests on IN #53 at Site 3: spatial distribution and histograms for (a–b) Pad 1, (c–d) Pad 2, (e–f) Pad 3, (g–h) Pad 4, and (i–j) Pad 5	49
Figure 4.24 LWD_S results from tests on IN #53 at Site 3: spatial distribution and histograms for (a–b) Pad 1, (c–d) Pad 2, (e–f) Pad 3, (g–h) Pad 4, and (i–j) Pad 5	50
Figure 4.25 Relationship between (a) LWD_L deflections measured on subgrade and on IN #53 aggregate, and between (b) LWD_L and LWD_S deflections measured on IN #53 aggregate (data from Pads 1–5 at Site 3)	51
Figure 4.26 Nuclear density results for IN #53 at Site 3	51

Figure 4.27 MFS data for Site 3: spatial distribution and histograms for (a–b) Pad 1, (c–d) Pad 2, (e–f) Pad 3, (g–h) Pad 4, and (i–j) Pad 5	52
Figure 4.28 (a) View of cement-treated permeable base (CTPB) and open-graded asphalt (OGA) drainage layers at Site 3; and view of (b) OGA, (c–e) CTPB surface, and (f) thickness of CTPB layer	53
Figure 4.29 Summary of k data from APT program on open graded asphalt and cement-treated permeable base at Site 3	53
Figure 4.30 Examples of variation of k with repeat measurements at testing locations on (a–b) open graded asphalt, and (c–d) cement-treated permeable base at Site 3	54
Figure 4.31 Summary of data from Sites 1–3 and from SBRITE strips: (a) k , (b) MFS, (c) LWD_L deflections, (d) dry density of IN #53 aggregate, and (e) LWD_L deflections of underlying subgrade	55
Figure 4.32 Relationship between k and MFS (only data with $S < 35\%$ from Sites 1, 2 and the untreated strip at the SBRITE site)	56
Figure 5.1 Laboratory in-crate testing of (a) IN #53, and (b) IN #8	57
Figure 5.2 Comparison of laboratory APT data for IN #53 (Crates I, II, III, and V)	60
Figure 5.3 Hydraulic conductivity data from 11 falling head tests on IN #53 (for each test, the figure shows only data from measurements obtained by increasing the hydraulic gradient)	60
Figure 5.4 (a–g) Preparation of compacted sample in large permeameter; (h) detail of screens at ends of permeameter; and (i) compaction of last aggregate lift with vibratory hammer on wooden pad	61
Figure 5.5 (a) Setup for constant head tests in large permeameter, (b) testing protocol, and (c) example of data from a single stage	62
Figure 5.6 Data collected from large permeameter tests: (a) I (stages 1–5), (b) II (stages 1–5), (c) IV (stages 1–5), and (d) V (stages 1–2). Darker symbols identify data used to calculate value of k displayed	62
Figure 5.7 Data for test VI in which k increased over time. For this test only the measurements from the first stage are considered reliable	63
Figure 5.8 (a–d) Example of particle size distributions of aggregate retrieved from locations shown in (e) after completion of flow tests	64
Figure 5.9 APT testing of compacted aggregate inside large permeameter: (a) schematic of setup, (b) view of aggregate surface in Test I, and (c) view of aggregate surface in Test II	64
Figure 5.10 (a) Concrete pads in forms, and (b) side view of pad thickness	65
Figure 5.11 Examples of results of repeat APT measurements on pervious concrete pads (tests from October 2022—all with identical boundary conditions)	65
Figure 5.12 Examples of results of repeat APT measurements on pervious concrete pads (tests performed in October 2023)	66
Figure 5.13 Position of APT apparatus when testing (a) center of large pad, (b) corners of large pad, and (c) center of small pad (refer to Figure 2.2 for dimensions of apparatus)	66
Figure 5.14 Air permeameter testing of (a) small pad on rubber foam; (b) large pad with sprayed foam bottom support; and (c) large pad after treatment of base and sides with spray foam (note: marking on pad ensured consistent positioning of APT device)	67
Figure 5.15 APT measurements on large pad with different bottom and edge boundary conditions (tests from March 2022, see statistics in Table 5.8)	67
Figure 5.16 APT measurements on large pad with different bottom and edge boundary conditions (tests from October 2023, see statistics in Table 5.10)	68
Figure 5.17 (a) Results of falling head tests on cores from center of pervious concrete pads, and (b) view of cross-section of one of the cores	69
Figure 5.18 The k values from falling head tests on all cores obtained from pervious concrete pads (see core locations in Figure 5.19)	69
Figure 5.19 Comparison of falling head and APT k data for (a) both pads, (b) large pad only, and (c) testing locations on two pads	69

1. INTRODUCTION

1.1 Project Background and Problem Statement

The presence of excess moisture in pavement structures is one of the most detrimental factors affecting pavement durability. When subjected to dynamic loading, excessively wet pavement structures tend to develop high pore water pressures that lead to a reduction of the elastic moduli of both bound and unbound layers, ultimately causing rutting and fatigue cracking of asphalt pavements. Pumping of fines occurs in saturated concrete pavement structures under vehicular loading that results in joint faulting and ultimately failure. In addition, saturated pavement structures are highly susceptible to cycles of freezing and thawing that ultimately lead to the deterioration of the bound layers and the weakening of unbound layers.

Water enters pavement systems by seeping upward from high groundwater tables, flowing laterally from pavement edges and shoulder ditches, and infiltrating through surface cracks and joints. Managing water inflow requires designing pavement structures that prevent water from entering pavement systems and then quickly remove water that does happen to enter. Current water management practice in pavement design commonly involves a permeable base/subbase that functions as a drainage layer, and that ties into a subsurface drainage system (e.g., edge drain). Different design solutions for the drainage layer are employed by different transportation agencies using both stabilized and unbound aggregates. Regarding the latter, INDOT specifications continue to consider the option of using a coarse uniform aggregate such as Indiana #8. Work performed as part of a previous research project (Getchell et al., 2020) as well as preliminary field trials indicate that aggregates with particle size distribution falling within the band for Indiana #43 (or even #53) may be better candidate materials for the drainage layer. This is in line with national trends that, as a result of the documented performance issues (aggregate breakdown, early age cracking from penetration of concrete mortar (ACPA, 2007) and construction (instability of the construction platform) associated with the use of aggregates such as Indiana #8, have seen specifications transition from prescribing “permeable” (>550 ft/day) to “free draining” (permeability < 350 ft/day) drainage layers (ACPA, 2010).

While field trials indicate that aggregates such as Indiana #43 appear to function well as a drainage layers, recent experience shows that these aggregates may be difficult to compact without compromising permeability, due to particle crushing and the occurrence of segregation. As a result, contractors tend to under compact aggregate drainage layers, which reduces overall pavement strength/stiffness and, for asphalt pavements, compromises compaction of overlying asphalt layers. It becomes, therefore, imperative that INDOT define standard criteria for constructing aggregate drainage layers that provide adequate struc-

tural support while still supplying conduits for removal of excess water. Current requirements for pavement subbases including aggregate drainage layers are outlined in Section 302 of *INDOT's Standard Specifications* (INDOT, 2024). INDOT prescribes a standard process for aggregate drainage layer construction that involves aggregate spreading techniques, compaction roller requirements, minimum number of compaction roller passes, and trimming requirements. There are numerous disadvantages with this method-based approach for specifying drainage layer construction, the primary one being that contractor payment is not linked to product quality or long-term performance. Moreover, contractors may not be allowed to use the most economical or innovative procedures and equipment to produce the product sought.

Instead of method specifications, the AASHTO Highway Subcommittee on Construction (Doyle, 2003) recommends employing performance-based specifications that require accepting work based on engineering properties that predict performance. For aggregate drainage layers, the most critical engineering properties predictive of performance include saturated hydraulic conductivity and resilient modulus (AASHTO, 2015). Currently, INDOT has neither an established test method for determining the in-situ (i.e., as-constructed) hydraulic conductivity nor an established test method for assessing aggregate drainage layer stiffness/resilient modulus. This precludes the transition to performance-based specifications for aggregate drainage layer construction.

1.2 Project Scope and Research Objectives

This research study aimed to evaluate methods for measuring performance parameters of aggregate drainage layers in-situ and provide INDOT guidance for developing performance-based specifications for these layers.

Within this broad scope, the project had the following specific objectives.

- Identify state of the art testing methods for in-situ control of compaction and permeability of aggregate layers.
- Evaluate these methods in field relevant conditions.
- Assess their suitability/practicality (e.g., ease of use, rapidity of measurements) for a range of site conditions.
- Determine performance parameters of the selected methods.
- Provide recommendations for QA/QC procedures, and if appropriate, develop testing protocols for inclusion in the Indiana Test Methods.

1.3 Activities and Organization of Report

To address the previously outlined research objectives, the scope of work included the following activities, which are described in the subsequent chapters with additional information provided in the appendices.

1. *Review of Literature Pertinent to In-Situ Testing Methods*

As discussed in Chapter 2, the field experimental program ultimately focused on two methods: the light weight deflectometer (LWD) and the APT for measuring, respectively, the stiffness and the saturated hydraulic conductivity of aggregate layers. The cost and the complexity (time constraints, difficulty in repeating tests) of the ambitious field-testing program conducted as part of this project required detailed planning to ensure efficient use of field resources and collection of reliable data. Essential to this effort was a study of the selected testing methods, with emphasis on reviewing documentation of experiences from other researchers. A summary of this review is presented in Chapter 2 of this report.

2. *Experimentation on Two Test Strips*

As part of this project two test strips (20 ft × 60 ft) were constructed at the site of Purdue's Steel Bridge Research Inspection Training and Engineering (SBRITE) center utilizing equipment and procedures used in highway construction projects. The strips consisted of a layer of compacted Indiana #53 (herein referred to as IN #53) aggregate placed over either the compacted natural soil or the cement-treated subgrade.

Extensive testing with high spatial density using a range of techniques was conducted on the strips to obtain a statistically relevant amount of data. This effort was aimed at exploring issues of repeatability and investigating possible relationships between the measured parameters. Control of the construction schedule enabled detailed characterization of both the subgrade and the individual aggregate lifts, and continuous access to the site allowed repeat measurements under different environmental conditions. Testing of the two strips also permitted investigating the effects induced by variations in construction conditions.

Chapter 3 provides details on the strip construction process, the experimental program and the key insights derived from the analysis of the test results. Additional information is provided in Appendices A to C.

3. *Testing at INDOT Construction Sites*

Three construction sites were selected for field testing: the Cherry Lane extension project in West Lafayette, IN, the reconstruction of SR 46 in proximity to Bloomington, IN, and the widening of I-65 in Lebanon, IN. At all three sites testing focused primarily on the layer of compacted IN #53 aggregate constructed over the cement-treated subgrade, which, per INDOT specifications, was intended to function as a separator layer. Depending on the site, additional tests were performed on the underlying cement-treated subgrade and/or on the overlying drainage layer.

This stage of the experimental program was aimed at identifying practical advantages and/or issues associated with field deployment of the testing techniques and investigating specific issues related to their applicability and the interpretation of the data. As testing at two of the sites was completed early in the research project, the experience from these sites also served to inform and guide the design of the experimental program performed on the testing strips specifically constructed for this project (see above).

Details on the sites and analysis of the test results are presented in Chapter 4.

4. *Laboratory Testing Program*

The laboratory testing program was primarily designed to complement the field permeability tests. It comprised hydraulic conductivity measurements on laboratory prepared samples, including both constant and falling head tests performed in custom setups, as well as tests using the APT apparatus employed in the field. In addition to providing reference data, the testing program was designed to investigate key performance parameters of the APT device (repeatability, accuracy, impact of boundary conditions). With these goals in mind, tests were performed on both aggregate samples as well as on samples of pervious concrete, the latter chosen as a model material. Chapter 5 summarizes the results from this portion of the experimental program.

A summary of the work performed, conclusions drawn from the study and recommendations for future work are provided in Chapter 6 of this report.

2. BACKGROUND OF TESTING METHODS

2.1 Introduction

As discussed in the introduction to this report, the goal of this research project was to identify and assess test methods for in-situ control of the hydraulic conductivity and stiffness of aggregate drainage layers. The research specifically focused on two testing methods—the air permeameter test (APT) and the light weight deflectometer (LWD)—which were extensively employed at both the experimental SBRITE site (Chapter 3) and at three construction sites (Chapter 4). The scope of this chapter is to provide background on these two testing methods. Note that nuclear density tests were also performed in support of this research effort. As the nuclear density test is an established method, it is not reviewed here. Details on the specific equipment and procedures used are discussed in Chapters 3 and 4 when summarizing the testing programs performed at the various sites.

2.2 Air Permeameter Test

2.2.1 Overview

While the drainage properties of base/subbase layers play a critical role in the performance of pavements, and while the hydraulic conductivity is known to be characterized by significant spatial variability, no verification of the drainage properties is generally performed in the field. In practice, the hydraulic conductivity of such layers is more commonly derived from empirical relationships with particle size distribution and/or density. For example, the DRIP (Drainage Requirements in Pavement) software (Applied Research Associates, 2014), which is used for the design of drainage and separator layers, relies on the (Moulton, 1980, August; reprinted, July 1990) correlation (based

on D_{10} , porosity and percentage passing the #200 sieve) to estimate the hydraulic conductivity of unbound layers.

Various tests for measuring the in-situ hydraulic conductivity of aggregate layers have been previously proposed, relying on both air and water as permeant fluids (e.g., see White et al., 2007 and Clyne et al., 2001). For many of these methods the testing procedures can be quite complex and lengthy, and verification of test measurements not always straightforward. For example, the MnDot permeameter introduced by the Minnesota Department of Transportation (e.g., Clyne et al., 2001) not only requires digging a cylindrical well hole in the aggregate and measuring the water flow rate, but derivation of the saturated hydraulic conductivity involves selecting a theoretical model to obtain the steady flow rate and assumptions on the shape of the saturated bulb.

The APT was developed by White et al. (2007) and White et al. (2014) to enable rapid in-situ measurements of the hydraulic conductivity of granular layers of pavement systems, and in part overcome some of the challenges encountered with previous methods. The 2007 paper describes in detail the theory underlying the test and presents the first version of the APT device. A revised design of the APT device is presented in (White et al., 2014). The latter device was employed in this research. The following subsections summarize the theory behind the method (Section 2.2.2), describe the APT equipment and the testing and data reduction procedures (Section 2.2.3), and review factors affecting interpretation of the APT data (Section 2.2.4) and previous experiences with the test method documented in the literature (Section 2.2.5).

2.2.2 Theory

The APT apparatus creates an axisymmetric pressure differential across the tested layer and measures the resulting volumetric gas flow rate using calibrated

precision orifices (Figure 2.1). The saturated hydraulic conductivity (k_{sat}) of the tested medium is derived from these measurements using Equation 2.1–Equation 2.5. As a first step (Equation 2.1), the gas permeability of the medium is calculated from the absolute gas pressure on the soil surface ($P_{soil\ surf. [Pa]}$) and the volumetric flow rate ($Q [m^3/s]$). As discussed below, the first is measured, while the latter is calculated from measurements of the pressure across the calibrated orifice (Figure 2.1). Equation 2.1 is based on the modification of Darcy's law to account for the compressibility of the fluid flowing through the porous medium and the axisymmetric flow conditions generated by the APT apparatus. See White et al. (2007) for details on the derivation of Equation 2.1.

$$K_{gas}(m^2) = \left[\frac{2\mu_{gas} Q P_{soil\ surf. (abs)}}{r G_0 (P_{soil\ surf. (abs)}^2 - P_{atm}^2)} \right] \quad (\text{Eq. 2.1})$$

The additional parameters appearing in Equation 2.1—viscosity of the gas ($\mu_{gas} [Pa \cdot s]$), radius of the outlet ($r [m]$), and the dimensionless geometric factor G_0 —are known for a given permeant gas and geometry. G_0 reflects the effects that the sizes of both the seal and the sample relative to the outlet have on the pressure distribution within the porous medium. In particular, the value of G_0 is dependent on the depth to the impervious layer (the distance to the radial boundary appears to play a lesser role). The derivation of G_0 is based on previous work by (Goggin et al., 1988) and is discussed in detail by White et al. (2007).

Derivation of the saturated hydraulic conductivity, k_{sat} , from K_{gas} requires the relative permeability to gas (K_{rg}) of the medium (Equation 2.2). In the approach put forth by White et al. (2007, 2014), K_{rg} is derived using the (Brooks & Corey, 1964) relationship (Equation 2.3), and requires input of the Brooks-Corey pore size distribution index (λ), the residual water saturation (S_r) and the degree of saturation (S) of the tested material. The latter two parameters are used

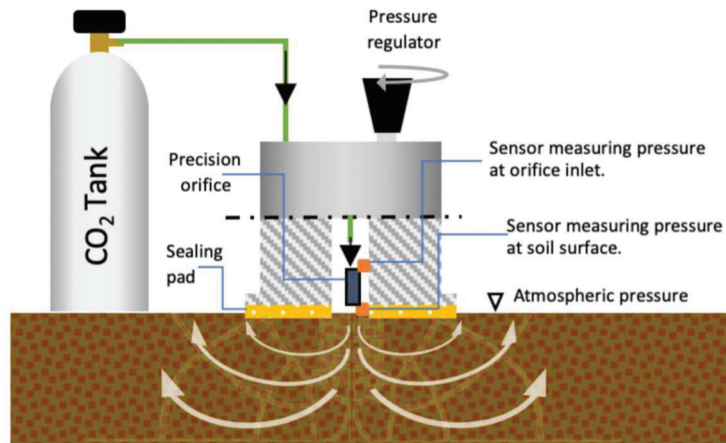


Figure 2.1 Conceptual schematic of APT apparatus.

to calculate the effective water saturation (S_e) of the material (Equation 2.4). While S is obtained from measurements in the field, λ and S_r are parameters that are derived from the soil-water characteristic curve (SWCC) of the material. In absence of the SWCC curve, values of these parameters can be derived from data available in the literature for similar materials or by employing existing empirical relationships with particle size distribution characteristics (e.g., Gupta et al., 2004). The complete formulation is summarized in Equation 2.5.

$$k_{sat}(m/s) = K_{gas} \frac{\rho_{water} g}{\mu_{water} K_{rg}} \quad (\text{Eq. 2.2})$$

$$K_{rg} = (1 - S_e)^2 \left(1 - S_e^{(2+\lambda)/\lambda} \right) \quad (\text{Eq. 2.3})$$

$$S_e = (S - S_r) / (1 - S_r) \quad (\text{Eq. 2.4})$$

$$K_{sat}(m/s) = \left[\frac{2\mu_{gas} Q P_{soil surf. (abs)}}{r G_0 (P_{soil surf. (abs)}^2 - P_{atm}^2)} \right] \cdot \frac{\rho_{water} g}{\mu_{water} (1 - S_e)^2 (1 - S_e^{(2+\lambda)/\lambda})} \quad (\text{Eq. 2.5})$$

Note that for unit consistency, ρ_{water} , g and μ_{water} appearing in Equation 2.2 and Equation 2.5 have

to be expressed in units of kg/m^3 , m/s^2 , and $\text{Pa}\cdot\text{s}$, respectively.

2.2.3 APT Equipment, Testing Procedures and Data Reduction

2.2.3.1 Equipment. Figure 2.2a shows the main components of the APT apparatus: the cylindrical housing that contains all the instrumentation (total mass ~ 18 kg), the compressed gas (CO_2 for all the work performed in this research) cylinder and associated tubing, valves and gauges and the wheel cart used for easy transport of the apparatus across a construction site. The top view of the device in Figure 2.2b shows the connection to the hose going to the compressed air cylinder, the pressure regulator through which the pressure applied to the orifice inlet is controlled, the valve used to switch between orifices and the display panel. A schematic showing inner and bottom views of the cylindrical housing is presented in Figure 2.2c, while the images in Figure 2.2d–e show details of the connections inside the cylinder housing and of the polyurethane base with the gas outlet and the pressure transducer ports.

The APT is equipped with three orifices (A, B, and C) of different size that are designed to be used for testing low permeability (A: $k < 100$ ft/day), medium permeability (B: $k = 100$ – $4,500$ ft/day) and high permeability (C: $k > 4,500$ ft/day) materials. Two

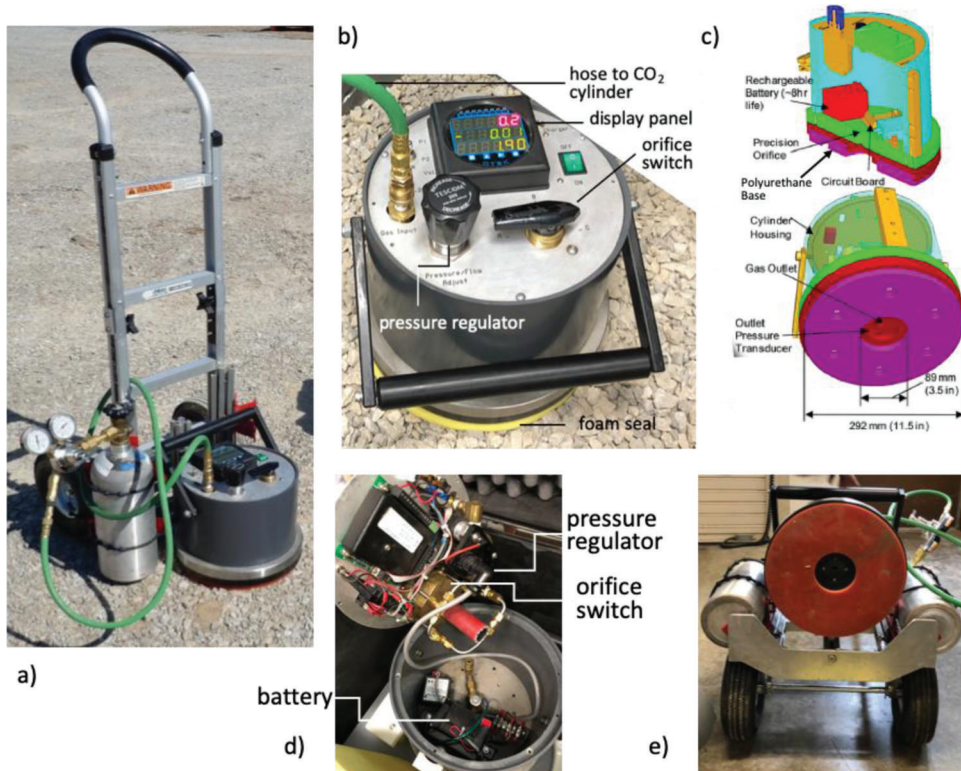


Figure 2.2 (a) APT apparatus mounted on cart, (b–c) details of connections inside cylinder housing components (from White et al., 2014); (b) APT mounted on cart; (c) details of connections inside cylinder housing; and (d) view of base plate.

sensors (Figure 2.1 and Figure 2.2c) measure the pressure at the input of the orifice and at its output. The first is used to calculate the volumetric flow rate through the orifice (Q in Equation 2.1 and Equation 2.5). The latter measurement reflects the pressure applied at the soil surface ($P_{soil\ surf.}$ in Equation 2.1 and Equation 2.5).

2.2.3.2 Testing procedures. Measurement of the saturated hydraulic conductivity with the APT involves the following procedure.

- First, the apparatus is positioned at the testing location. It is rested on a donut-shaped foam layer that functions as a seal (see Figure 2.2b).
- Once the device is turned on and the valve connected to the gas cylinder is opened, the pressure regulator is used to increase the pressure applied at the orifice inlet. This pressure is the top number visualized on the panel (P_1) and is displayed in psi (see Figure 2.2b and Figure 2.1).
- At the same time, the value of the gauge pressure applied at the soil surface increases. This pressure is the middle number visualized on the panel (P_2) and is displayed in units of inches of water (see Figure 2.2b and Figure 2.1). Using the regulator, P_2 is increased until it reaches a value of approximately 0.12 in. of water (~ 30 Pa). Currently, values of both P_1 and P_2 are recorded.
- The regulator is used to increase the pressure further and at least three additional measurements are performed, bracketing a value of P_2 of 0.25 in. of water (~ 62 Pa). This pressure range is selected to maintain values of the Reynolds Number low enough to ensure laminar flow conditions (White et al., 2007), to best represent the conditions occurring in pavement drainage layers in the field.
- The APT is lifted back on the cart and moved to a new testing location.

Note that while the bottom number on the display corresponds to the flow rate Q , this value is not recorded. It is instead calculated during data reduction from P_1 .

2.2.3.3 Data reduction. The data obtained from each testing location include four (or more) sets of measurements of P_1 and P_2 (gauge value of pressure applied at soil surface). A value of k_{sat} is derived from these data with the following procedure.

- The geometric factor (G_0) is first determined based on the estimated thickness of the aggregate layer (t) at the test location. The following equation provided by the APT manufacturer was used in this work (with t expressed in m):

$$G_0 = 4.6932 + 4.0196e^{(-0.0109 \cdot t)} \quad (\text{Eq. 2.6})$$

- For each reading, the flow rate is calculated from the pressure reading P_1 at the orifice inlet using an equation of the form shown below:

$$Q = \frac{aP_1}{b + P_1} + cP_1 \quad (\text{Eq. 2.7})$$

where a , b , and c are orifice and gas specific parameters derived from calibration of each orifice. While calibration factors for the orifices were provided by the APT manufacturer, an independent calibration was performed as part of this research. Figure 2.3 shows the setup used and the calibration curves derived for orifices B and C.

- For each reading, $\frac{P_{soil\ surf. (abs)}}{P_{soil\ surf. (abs)}^2 - P_{atm}^2}$ appearing in

Equation 2.5 is calculated from the P_2 reading, noting that P_{atm} is the atmospheric pressure and $P_{soil\ surf. (abs)}^2$ is simply equal to P_2 plus P_{atm} .

- As ρ_{water} , g , μ_{water} , μ_{gas} , r , G_0 , λ , and S_e are known parameters (S_e can be calculated from the in-situ degree of saturation (S) and the material's S_r) and constant for all readings, Equation 2.5 can be rewritten as:

$$Q = k_{sat} \frac{(P_{soil\ surf. (abs)}^2 - P_{atm}^2)}{A \cdot P_{soil\ surf. (abs)}} \quad (\text{Eq. 2.8})$$

Where,

$$A = \frac{\mu_{gas} \rho_{water} g}{r G_0 \mu_{water} (1 - S_e)^2 (1 - S_e^{(2 + \lambda)/\lambda})} \quad (\text{Eq. 2.9})$$

- k_{sat} can be then derived as the slope of the linear regression line through the Q and $\frac{(P_{soil\ surf. (abs)}^2 - P_{atm}^2)}{A \cdot P_{soil\ surf. (abs)}}$ data.

Figure 2.4 illustrates the testing procedure outlined above.

Note that the data reduction procedure described above deviates from that proposed by the developers of the APT. In that approach, a linear regression using the Q and $P_{soil\ surf.}$ data is performed to obtain the value of the flow rate in correspondence to a reference $P_{soil\ surf.}$ pressure of 0.25 in. of water. Equation 2.8 is then used to derive k_{sat} from this value.

2.2.4 Factors Affecting Test Interpretation

As highlighted in Section 2.2.2, several factors affect the value of k_{sat} determined from the APT measurements. Amongst these, the in-situ degree of saturation, the Brooks-Corey parameters (λ and S_r) and the dimensionless geometric factor (G_0) carry some uncertainty. It is therefore of interest to understand the sensitivity of k_{sat} to variations in these parameters. The primary findings from a study conducted by White et al. (2014) to explore the impact of these input parameters are summarized here.

- For a given radius of the outlet (1.75" \sim 4.45 cm), G_0 is primarily affected by the depth to the bottom impervious boundary and varies by less than 25% (from 5.79 to 4.71) as this depth increases from 3 to 12 in.
- The in-situ degree of saturation has a very significant impact on k_{sat} . This is illustrated in Figure 2.5a for the given values of S_r , G_0 , P_0 , Q , and λ , k_{sat} increases by one order of magnitude as S increases from 20% to 60%, and by approximately an additional order of magnitude if S reaches 80%. According to White and Vennapusa (2014)

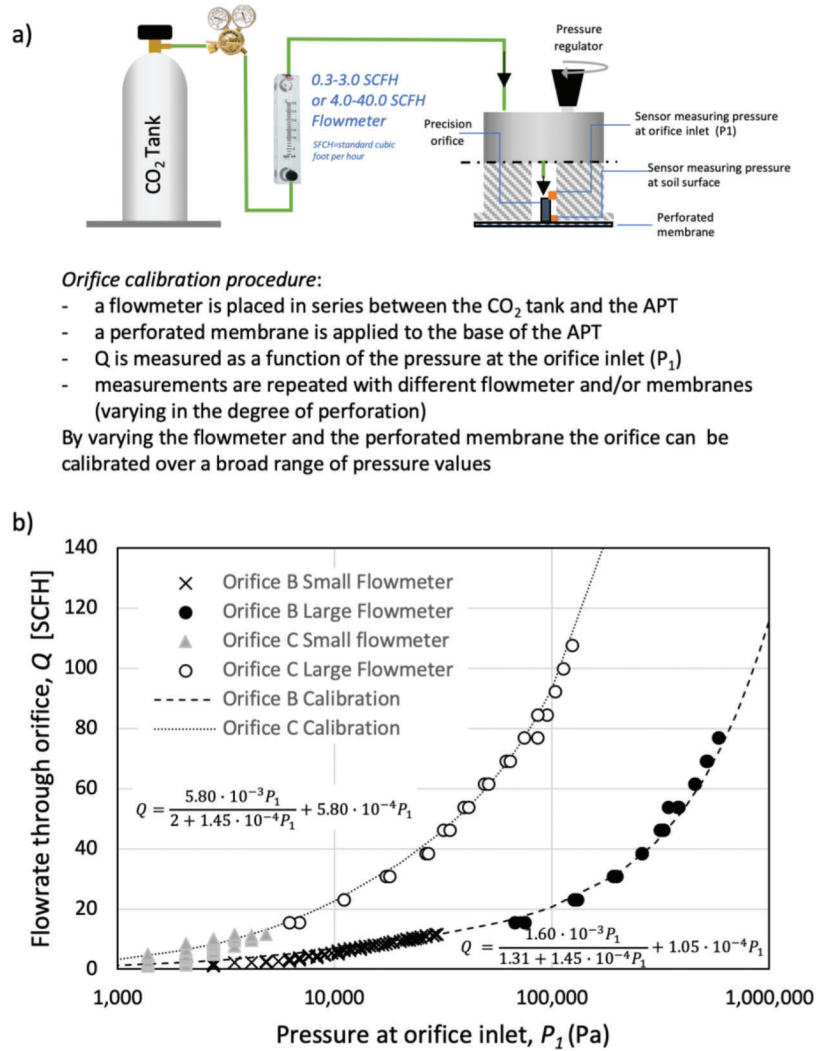


Figure 2.3 (a) Setup for calibration of orifices, and (b) calibration curves for orifices B and C.

the mean S for granular pavement base materials ranges between 16% and 62%.

- Both λ and S_r play a smaller role. The impact of λ is greater for high values of the degree of saturation (e.g., for $S = 80\%$ k_{sat} increases by a factor of 4 as λ goes from 1 to 5), but negligible for $S < 40$. For λ greater than ~ 5 , k_{sat} is largely independent of λ across all values of S (Figure 2.5a). Note that for the type of materials of interest to this research project, λ falls below 5, i.e., in the range in which not only do inaccuracies in the selection of its value play an important role, but also the impact of S is most significant.
- For a given value of S , k_{sat} increases as S_r decreases. As shown in Figure 2.5b a variation of S_r between 0% and 40% is reflected in a three-fold reduction in k_{sat} .

2.2.5 APT Validation and Previous Field Experiences

Laboratory validation of the APT device employed in this research project is discussed by the developers of the apparatus in White et al. (2014). In addition to

investigating the sensitivity of the test results to the input parameters (see Section 2.2.4), and verifying operational aspects of the device (e.g., performance of base seal), this work presents tests aimed at evaluating the measurement depth of the APT, quantifying the repeatability of the test, and assessing the device's accuracy. Regarding the first point, tests performed gradually increasing the thickness of the tested layer demonstrate a measurement influence depth of ~ 5 cm (2").

Assessment of the of the device's repeatability in this work focused specifically on the impact of P_2 (gauge pressure applied to soil surface) on the measured k_{sat} . Through repeat laboratory measurements on samples of different granular materials (with k_{sat} varying by over two orders of magnitude), White et al. (2014) showed that the data were highly repeatable ($CV < 1\%$) for $P_2 > 10$ mm and flow rate $Q > 100$ cm³/s. Where these minimum values could not be met (for materials with either too high or too low permeability), the CV increased up to 23%.

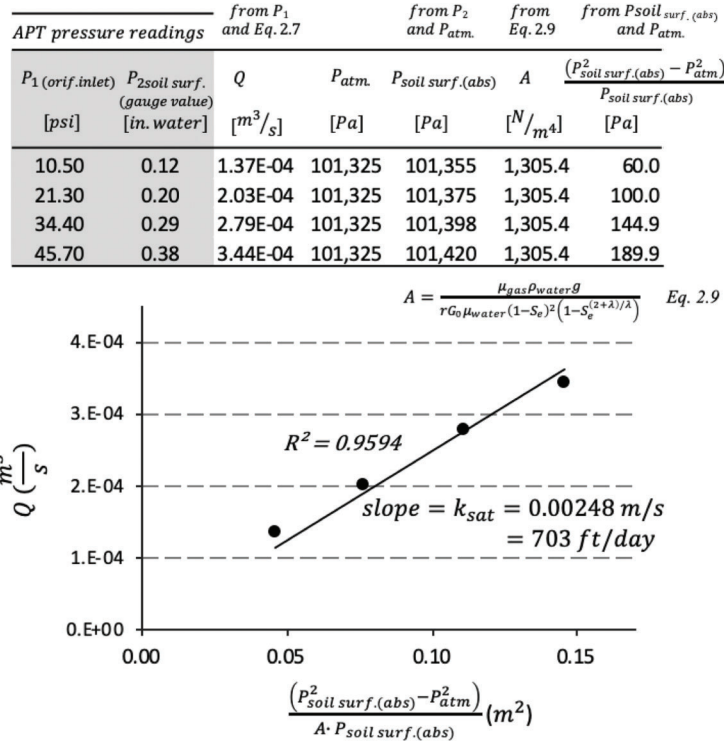


Figure 2.4 Illustration of the derivation of the saturated hydraulic conductivity from the APT pressure readings.

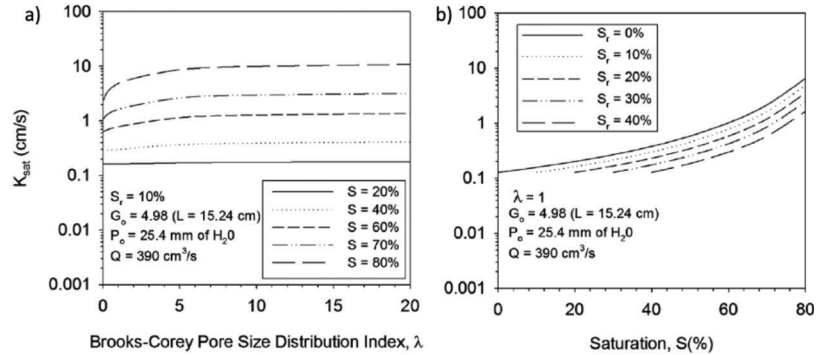


Figure 2.5 Results of parametric study showing influence of (a) Brooks-Corey parameter λ , and (b) degree of saturation, S , and residual degree of saturation, S_r , on calculation of saturated hydraulic conductivity (from White et al., 2014).

Finally, White et al. (2014), present k data for a range of geomaterials with A-1-a to A-1-b AASHTO classification and find that “the ratio of k_{sat} determined from the APT to laboratory hydraulic conductivity tests varied from about 0.2” to 5.0”. They attribute this discrepancy to difference in flow conditions (vertical flow and possible non-laminar conditions) and fines migration in the laboratory tests.

While the APT has been commercially available for several years, to date its implementation in the field has been limited. The following is a summary of the application and performance of the APT in studies documented in the literature.

- *Xiao et al. (2013)*: this work documents the use of the APTs for measuring k_{sat} on four test sections (15' \times 18') constructed using different crushed and uncrushed

aggregate materials ($D_{10} = 0.01$ – 1.36 mm, D_{60} – 6.2 – 10.2 mm; $P_{200} = 5\%$ – 12%). Average values of k_{sat} for the four test sections varied between $\sim 4,200$ and $8,500$ ft/day and were found to be strongly correlated with the % of fines of the four aggregates, and to a lesser degree with the aggregate shape properties. APT measurements were also used to quantify the different degree of spatial variability ($CV = 10\%$ – 66%) characteristic of each section.

- *Vennapusa and White (2015)*: in this work by the developers of the apparatus, the APT device was used to map variations in hydraulic conductivity of an open-graded subbase layer (material varying from GP to GP-GM to GW-GM) after injection from the surface, through drilled holes, of expandable polyurethane foam. Tests performed directly on the subbase after removal of the overlying PCC surface layer allowed identifying the highly concentrated zones in which the foam had

successfully propagated into the subbase, highlighting a two order of magnitude reduction in k_{sat} relative to the untreated areas.

- *Li et al. (2017)*: this work by the developers of the apparatus involved tests on unpaved roadway test sections and demonstrated the use of the APT in quantifying the increased hydraulic conductivity realized by placing a geocomposite under a compacted aggregate layer. In this same study, the authors showed that the value of k_{sat} determined for the geocomposite agreed with in-lab measurements performed using a large horizontal permeameter. APT measurements of k_{sat} of the aggregate layer (GP-GM/A-1-a) were on the order of 65 ft/day and exceeded the values determined in the lab by a factor of 20.
- *White et al. (2018)*: this work by the developers of the apparatus documents the use of the APT as part of the reconstruction of the Central Iowa Expo facility. APTs were performed with high density (0.6–1 m spacing) on the 6' crushed limestone modified subbase (MSB) layer (GP-GM/A-1-a) at three sections differing in the underlying support conditions (~100 tests per section). The APT data highlighted differences in the spatial variability of k_{sat} between the sections. The over three orders of magnitude variation in k_{sat} (~ 10^3 to 10^6 ft/day) measured across all sections was related, based on samples collected at ten locations across the site, to differences in aggregate gradation which were attributed to material segregation and degradation during compaction.

2.3 Light Weight Deflectometer (LWD)

2.3.1 Overview

Shown in Figure 2.6, the light weight deflectometer (LWD) is a stiffness-based in-situ test commonly used for construction quality control/assurance when placing compacted aggregates. LWD testing involves dropping a heavy weight from a set height along a guide rod onto a loading plate resting on the ground surface. The impulse generated by the drop weight drop striking the loading plate, which is cushioned by a spring buffer, induces a vertical deflection at the ground surface that is inversely proportional to the ground stiffness. Either an accelerometer or geophone housed inside of the loading plate measures ground response, and an external data acquisition device computes deflection by integrating with respect to time. Deflections output by the data acquisition device correspond to the maximum (initial local) values measured over their pulse durations, as illustrated in Figure 2.7.

2.3.2 INDOT LWD Requirements

INDOT conducts LWD tests in accordance with Indiana Test Method (ITM) 508 (INDOT, 2025). The test method requires that the drop weight weigh 10 kg and be supported by a guide rod weighing 5 kg. The loading plate is required to be 300 mm in diameter and weigh 15 kg (i.e., equal to sum of drop weight and guide rod masses). Set drop heights are unique to each individual LWD and are calibrated such that the peak

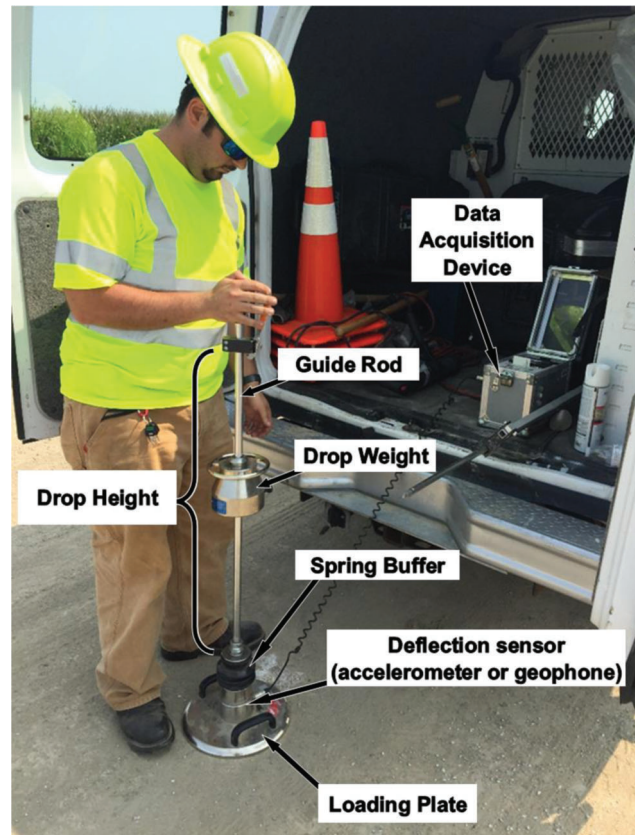


Figure 2.6 Typical light weight deflectometer testing setup.

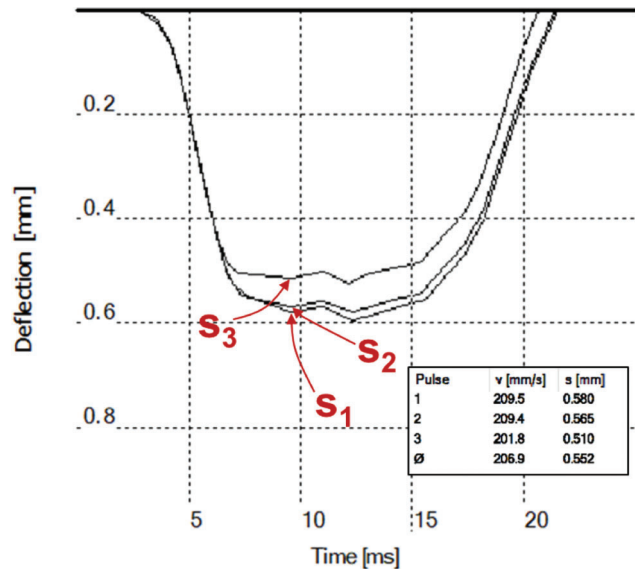


Figure 2.7 Example surface deflection response measure by LWD (note that output deflection values occur at the initial local maximum).

applied loadings are presumed equal to 7.07 kN. Maximum deflections are computed from an accelerometer housed inside the center of the loading plate.

INDOT Standard Specification 203.24 provides requirements for LWD testing of compacted aggregates

for construction acceptance. Construction inspectors will conduct a set of three LWD tests at a random station number for every 800 ton of compacted aggregate. LWD test spacing requirements are shown in Figure 2.8 (when construction areas are wider than 8 ft) and in Figure 2.9 (when construction areas are narrower than 8 ft). Acceptance criteria (i.e., maximum deflections) are typically established by constructing a test section onsite in accordance with ITM 514. However, standard specifications prescribe maximum allowable deflections for compacted No. 53 aggregate that is shown in Table 2.1. The mean deflection for the set of three tests shall not exceed the specified allowable mean deflection thresholds. Likewise, no individual test comprising the set shall exceed the specified single test maximum deflection thresholds.

2.3.3 Factors Affecting LWD Deflections

LWD deflection is inversely related to ground stiffness (i.e., soil elastic modulus). Indeed, soil elastic moduli can be backcalculated from LWD deflections using classical Boussinesq stress distribution theory. Since LWD deflection is effectively a measure of soil elastic modulus, factors influencing modulus also influence deflection.

2.3.3.1 Stress and strain level. Soil modulus is influenced by both the in-situ effective stress state, as

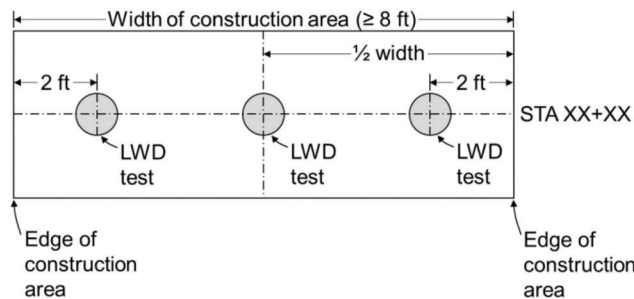


Figure 2.8 LWD testing locations for compacted aggregate construction acceptance in accordance with INDOT Standard Specification 203.23 (construction width \geq 8 ft).

well as by the shear level and resulting strain. The effect of the in-situ stress state on the initial elastic modulus is well established and described by a power function (building on the original work by (Hardin & Black, 1966). The degradation of soil modulus with strain has been long recognized starting from the early research

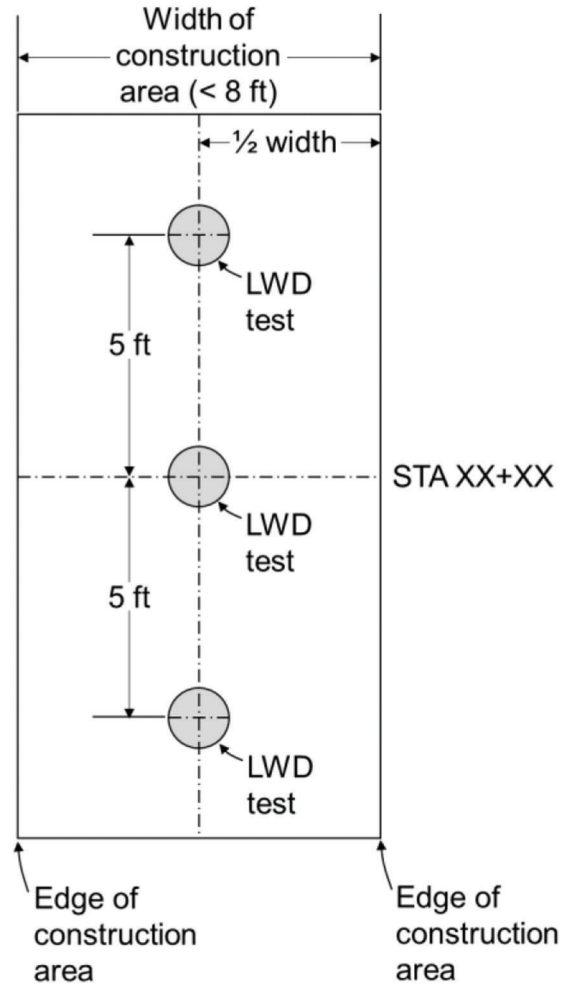


Figure 2.9 LWD testing locations for compacted aggregate construction acceptance in accordance with INDOT Standard Specification 203.23 (construction width < 8 ft).

TABLE 2.1
Maximum LWD deflection criteria for compacted No. 53 aggregate per INDOT Standard Specification 203.23

Material Type	In Areas Where Proof Rolling Can be Performed		In Areas Where Proof Rolling Cannot be Performed ¹	
	Allowable Mean Deflection ²	Maximum Deflection for a Single Test ³	Allowable Mean Deflection ²	Maximum Deflection for a Single Test ³
6-in.-thick layer of No. 53 Aggregate	≤ 0.51 mm	0.57	≤ 0.60 mm	0.65
12-in.-thick layer of No. 53 Aggregate	≤ 0.34 mm	0.40	≤ 0.47 mm	0.52
18-in.-thick layer of No. 53 Aggregate	≤ 0.31 mm	0.35	≤ 0.44 mm	0.49
Aggregate Over Lime Modified Soil	≤ 0.30 mm	0.35	—	—
Aggregate Over Cement Modified Soil	≤ 0.27 mm	0.31	—	—

¹Areas where proof rolling cannot be performed are those that are inaccessible to larger equipment (e.g., pavement patches).

²Mean deflection over set of three LWD tests shall not exceed the prescribed allowable mean deflection.

³No individual test of the set of three tests shall exceed the maximum deflection for a single test.

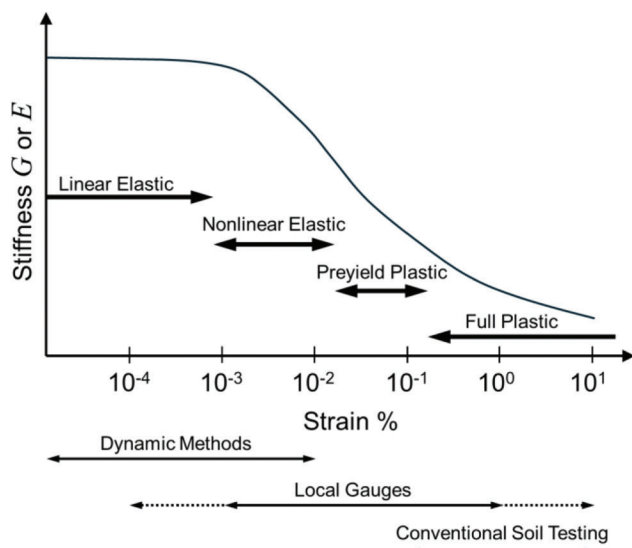


Figure 2.10 Modulus degradation curve (after Mitchell & Soga, 2005).

with the resonant column (e.g., Hardin & Drnevich, 1972a, 1972b). Figure 2.10 shows a typical S-shaped modulus degradation curve, which includes four zones that correspond to: linear elastic, nonlinear elastic, pre-yield plastic, and full plastic response (Mitchell & Soga, 2005). Under small strains (linear elastic zone), particles do not slide relative to each other, so deformations are mostly due to individual particle stiffnesses, their packing arrangement, and confining stresses. Under increasing strains (nonlinear elastic zone), soils exhibit nonlinear stress-strain behavior since the applied shear stress is sufficient to cause particles to slide relative to each other, though deformations due to particle movements remain largely recoverable. Beyond this zone, the response transitions to become fully plastic. See Oztoprak and Bolton (2013) for a discussion of the parameters affecting modulus degradation of granular materials.

LWD tests generally tend to induce stresses and strains on par with those encountered within the nonlinear elastic zone, although plastic straining can occur when testing relatively soft soils as reported by (Mooney & Miller, 2009). Within the nonlinear elastic zone, the elastic modulus tends to decrease with increasing stresses and strains, so LWD deflections would increase exponentially with increasing applied stress. However, higher applied stresses will increase confining pressures that in turn tend to increase elastic moduli, particularly for granular soils. Several models have been proposed over the years to consider these stress dependencies (e.g., Andrei, 1999; Witzczak, 2004) employing parameters such as bulk stress, deviator stress, and octahedral shear stress.

2.3.3.2 Moisture. Elastic moduli of soils will significantly decrease in response to increased moisture contents. As moisture content increases, so too will degree of saturation. Soils with low degrees of

saturation have higher apparent effective stresses due to the presence of matric suction (i.e., net negative pore pressures due to water capillarity). However, additional water entering pore air voids and increasing degree of saturation will lower matric suction and decrease apparent effective stress and, as a result, will weaken the mechanical properties (e.g., elastic modulus) of the soil. Several sources such as (Briaud, 2013; Fredlund et al., 2012; Ng & Menzies, 2007) discuss this phenomenon in greater detail. So, for LWD testing, deflections will increase with increasing soil moisture content.

2.3.3.3 Relative density/compaction. Soil elastic modulus tends to increase with increasing relative density and relative compaction. More densely packed soils have greater amounts of interparticle contacts offering stiffer resistance to deformation. Soils may be densified through compaction, which is the process by which a momentary applied load (rolling, tamping, or vibration) reduces in volume a mass of a soil through the expulsion of air. Hilf (1991) provides an in depth discussion of soil compaction processes and their effects on the mechanical properties of soils. So, with increasing compaction, LWD deflection will tend to decrease. However, deflection will approach a minimum value as soil relative density approaches 100%.

2.3.3.4 Particle size distribution. Some particle size distribution properties that generally affect soil elastic modulus include fines content, uniformity (well graded versus uniformly), and maximum particle size. Elastic modulus tends to decrease with increasing fines content, so LWD deflections are likely to be higher when conducted on soils with relatively higher fines contents. Likewise, more uniformly graded soils tend to have lower elastic moduli thereby yielding higher LWD deflections. Soils with larger maximum sized particles tend to have higher elastic moduli yielding lower LWD deflections when tested. Several other factors relating to particle size distribution affect elastic modulus; however, documentation of each and every one is beyond the scope of this report.

3. FIELD TESTING AT SBRITE SITE

3.1 Introduction

This chapter presents and analyzes the results of the field-testing program conducted on two test strips, constructed as part of this research project at the Steel Bridge Research Inspection Training and Engineering (SBRITE) center in Purdue University's Center for Aging Infrastructure (CAI) in West Lafayette, IN. As discussed in more detail below, the two strips differed in the characteristics of the subgrade and the construction procedure: the aggregate layer of one strip was built in two lifts using Indiana #53 (IN #53) aggregate over the cement stabilized subgrade, whereas in the other strip the same aggregate was placed and compacted in a single lift over the compacted natural soil.

The chapter is organized in five sections beyond this introductory one. The first two describe the methods used to construct the testing strips (Section 3.2) and summarize the testing program (Section 3.3) which included light weight deflectometer (LWD), air permeameter (APT) and nuclear density tests and imaging of the aggregate surface. Results of these tests are presented and analyzed in Section 3.4, which is comprised of seven subsections. The first three focus on the data collected on the finished surface of the two aggregate strips and on the underlying subgrade, and use a stochastic approach to examine the variability in the data across the two strips (Section 3.4.1), explore correlations between the measured parameters (Section 3.4.2) and analyze the impact of sample size on the assessment of whether a layer complies with specifications (Section 3.4.3). Section 3.4.4 presents data from additional measurements collected on the first lift of one of the aggregate layers. Additional data collected at the site to assess the repeatability of the APT are presented in Section 3.4.5. Finally, the last two sections report on observations conducted on geotextile samples exhumed after completion of the testing program (Section 3.4.6) and on measurements performed to quantify compactor vibratory effects during construction of the strips (Section 3.4.7). Note that the investigations discussed in these last two sections fall outside of the scope of the project.

3.2 Construction of Testing Strips

The field-testing program at the SBRITE site (Figure 3.1) was conducted on two 60 ft by 20 ft test strips constructed in August–September of 2020. At the site, soil conditions under the vegetated organic layer include a clayey sand (SC) with 48%–49% fines, and mean liquid limit and plastic limit of 27.9% and 14.6%, respectively. The water table lies approximately 18 ft below the ground surface (Patriots Engineering and Environmental Inc., 2014).

After removal of the topsoil and excavation of an additional 6" thick layer of the natural soil throughout the site (Figure 3.2a–b), different procedures were followed for construction of the two strips. On the northern strip, herein referred to as “untreated strip,” the natural soil was simply compacted with target values of water content and dry unit weight of 8.3% and 129.1 pcf (20.1 kN/m³). Soil compaction was performed by an independent contractor (Specialties Company LLC of Indianapolis, IN) with the procedure summarized in Figure 3.2. The top 12 in. of the natural soil were first mixed at the target water content using a Wirtgen WR 250i (Figure 3.2c–d); the soil was then leveled using a CAT M140 grader (Figure 3.2g) and finally compacted using first a CAT CS56 pad-foot drum roller and then a CAT CS56 smooth drum roller (Figure 3.2h–i).

Slurry cement stabilization with a cement application rate of 50.8 lb/yd² was performed by the same contractor to a depth of 14 in. (35.6 cm) on the footprint of the second southern strip (herein referred to as “cement-treated strip”) targeting 8% water content and 125.1 pcf (19.6 kN/m³) dry unit weight. Subgrade compaction and soil stabilization specifications were based on laboratory compaction and unconfined compression tests performed according to INDOT design procedures (INDOT, 2013). Figure 3.4e–f show the application of the cement slurry and the Wirtgen WR 250i Soil Stabilizer used to mix the slurry with the natural soil. The cement-treated soil was then graded and compacted using the same procedure and equipment described above for the untreated strip (Figure 3.2g–h).

After completion of the subgrade, a grid of perpendicular lines with a uniform spacing of 3 ft was established on both strips to identify testing locations (Figure 3.3). The grid lines parallel to the east-west (transversal) direction were labeled with numbers 1–7 (starting from north), while the grid lines parallel to the north-west (longitudinal) direction were labeled with

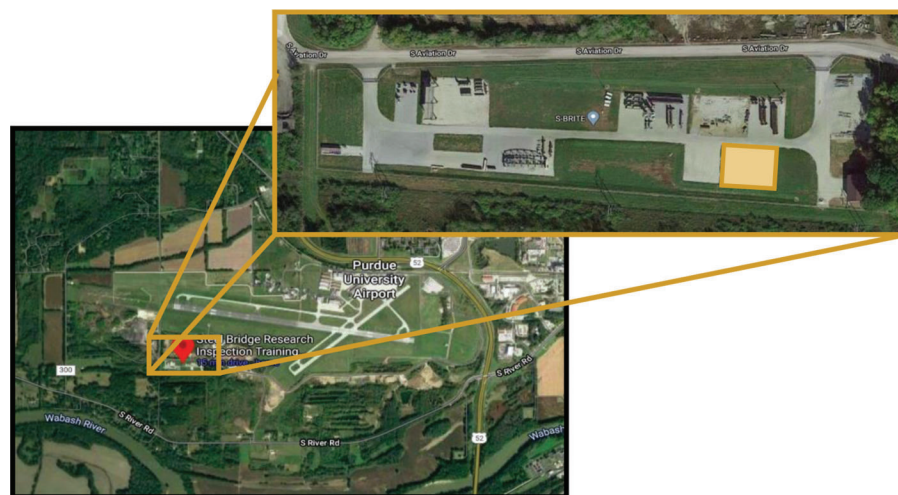


Figure 3.1 Location of SBRITE center in West Lafayette, IN.

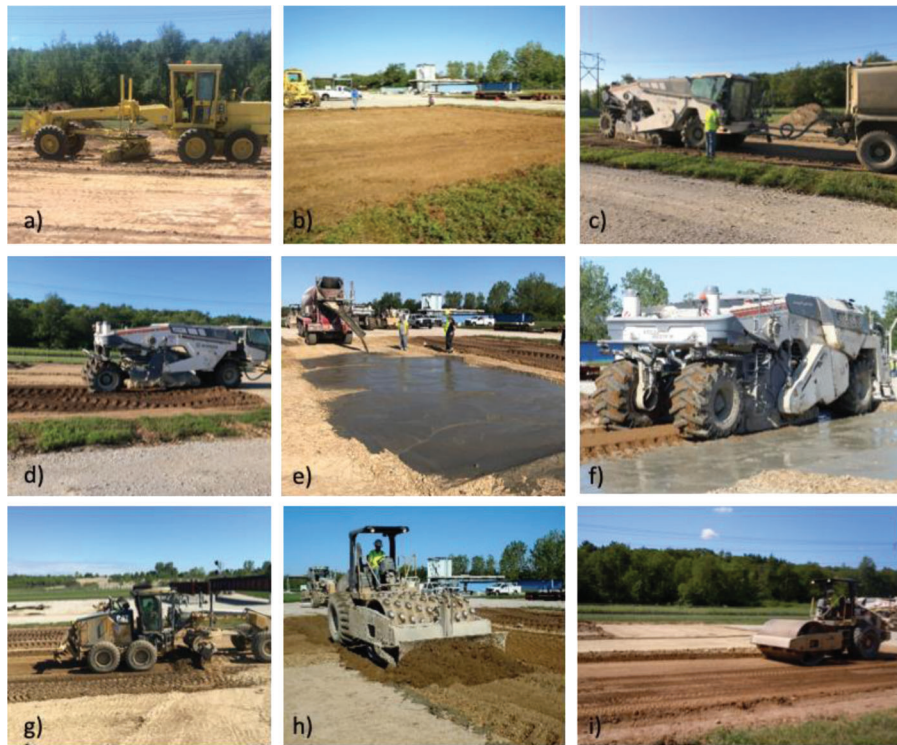


Figure 3.2 Equipment and methods used for subgrade modification: (a–b) site preparation; (c–d) water content control and mixing of natural soil on untreated strip; (e–f) cement-slurry treatment of subgrade of treated strip; (g) leveling; and (h–i) compaction of the subgrade of both strips with pad-foot drum and smooth drum roller.

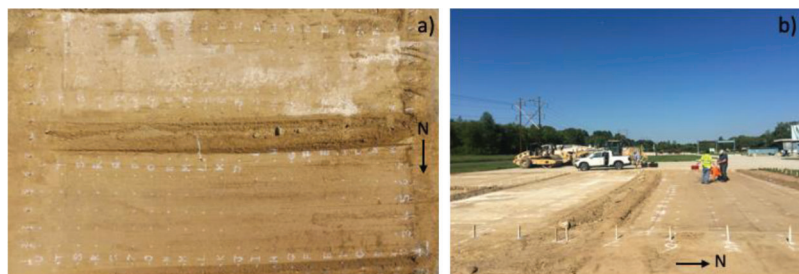


Figure 3.3 Aerial view and view from the east end of site of untreated (north) and cement-treated (south) strips after marking the testing grid on finished subgrade.

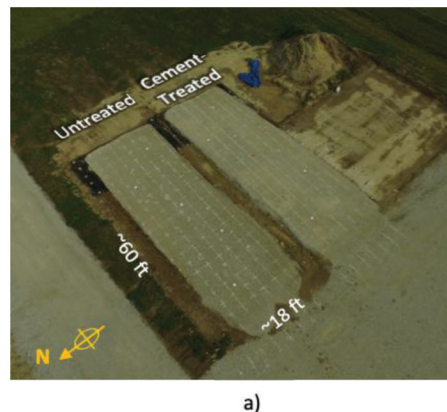


Figure 3.4 (a) Methods used for the construction of aggregate layers and the placement of geotextile and equipment (note: stakes used for marking testing grid), (b) mixing, (c–d) placement, (e) leveling, and (f) compaction of aggregate.

letters from A–T (starting from west). As the goal was to conduct additional measurements at these same locations after construction of the overlying aggregate layer, the grid was established connecting wooden stakes placed at 3-ft intervals along the perimeter of each strip with Nylon twine. Once the grid points were marked using traffic striping spray paint, the twine was removed, only to be repositioned when the testing grid was to be drawn again at the subsequent construction stage.

Prior to placement of the aggregate, a geotextile (GEOTEX® 601 6 oz nonwoven geotextile fabric manufactured by Propex, see product data sheet in Appendix A) was placed on the subgrade on the eastern most side of the strips (Figure 3.4a), overlapping rows P – T on the grid (Figure 3.5a).

Aggregate layers of both strips were built using crushed limestone sourced from US Aggregates Inc. (Delphi, IN). The average particle size distribution for this aggregate (with classification GW and A-1-a according to USCS and ASSHTO, respectively) is shown in Figure 3.5b along with the band that identifies the limits for the IN #53 designation. This gradation is regularly used by transportation agencies across the US for separation and drainage purposes (Getchell et al., 2020). On the untreated strip, the aggregate layer was constructed in a single lift (average thickness = 5.5 in. [14.0 cm]), while two lifts were used on the cement-treated strip (final mean thickness of 8.7 in. (22.1 cm)). In constructing all lifts, the aggregate was placed and graded using a CAT 930M wheel loader (Figure 3.4c–e) and then compacted using a CAT CS44B smooth drum roller (Figure 3.4f), following a sequence of 4 static, 4 vibratory ($f = 30$ Hz) and 4 additional static passes. To limit segregation of the material, care was placed in mixing the aggregate stockpile (Figure 3.4b). After completion of each lift, testing locations were again marked on the surface as described above. An aerial view of the completed strips captured by a drone after marking the testing grid on the finished aggregate surface is shown in Figure 3.5a.



3.3 Testing Program

3.3.1 Overview

A range of quality assessment techniques was employed to study the subgrade and aggregate layers of the two strips, including light weight deflectometer (LWD), air permeameter (APT) and, on the aggregate layers only, nuclear density (ND) tests. The testing program also included measurements of the thickness of the aggregate layer and imaging of the aggregate surface to quantify material heterogeneity. Except for the nuclear density tests, all tests were performed at locations on an orthogonal grid with uniform spacing of ~0.9 m (3 ft) in both directions (see Figure 3.5a for an aerial view of the strips captured from a drone). The grid was established after construction of each layer to ensure that tests were performed at the same locations on all layers. Figure 3.6 summarizes the tests performed at each grid location to characterize the subgrade and the finished aggregate layer. Additional tests included: LWD tests on the first lift of the aggregate layer on the cement-treated strip, and APT tests performed at select locations to assess the repeatability of the testing method.

3.3.2 Testing Methods

3.3.2.1 Elevation measurements. A Bosch GRL1000-20HVK Self-Leveling Rotary Laser was used to take elevation measurements referenced to a fixed control point after completion of the subgrade treatment and after compaction of each aggregate lift. Values of the thickness of the aggregate layer across the two strips were calculated from these measurements, yielding the maps shown in Figure 3.7.

3.3.2.2 Nuclear density tests. A total of 76 nuclear density tests (39 and 37 on the untreated and cement-treated strip, respectively) were performed on the

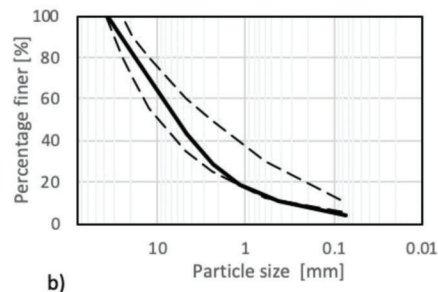


Figure 3.5 (a) Aerial view of finished test strips (note: nonwoven geotextile placed between subgrade and overlying subbase in eastern portion of strips). (b) Particle size distribution of IN #53 aggregate used to construct subbase. Dashed lines identify the IN #53 limits based on INDOT 904.03.

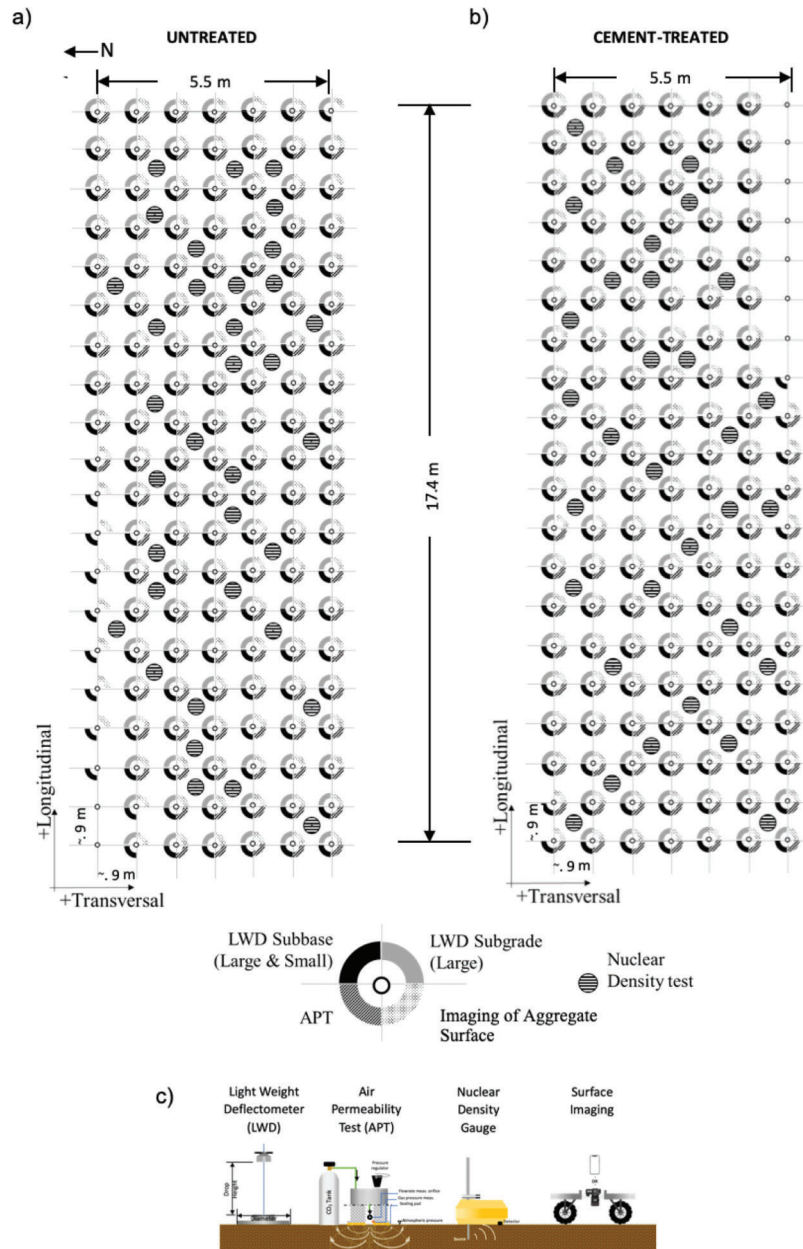


Figure 3.6 Map of testing program on (a) untreated, (b) cement-treated strips, and (c) schematic of testing apparatus.

aggregate layer using a Troxler 3430 device. Testing locations were offset from the testing grid so that driving the probes would not interfere with the other non-destructive tests. All measurements were performed positioning the source emitting controlled gamma rays and neutrons at a 15 cm (6 in.) depth within the aggregate layer and recording the signals at the surface detector over a 1-minute period. Values of dry density (ρ_d), water content (w) and degree of saturation (S) were derived from the test results following ASTM standard D6938-23.

3.3.2.3 Light weight deflectometer (LWD) tests. LWD tests were performed following ASTM E2583, using a Zorn ZFG 3.0 light weight deflectometer. LWD

tests were performed at all accessible points on the testing grid, using either a large (LWD_L : $D = 0.300$ m) plate (subgrade) or both large and small (LWD_S : $D = 0.150$ m) plate (aggregate layer), for a total of ~ 800 tests. The drop height was set to 0.720 m in the tests performed with the large plate and reduced to 0.17 m when using the small plate to apply a similar magnitude of stress on the loaded surface. The 0.17 m drop height used for the smaller plate was determined through a custom procedure that matched deflections at the center of a $\frac{3}{4}$ " thick plywood calibration disc produced using the two plates. In practice, a value of the modulus is commonly derived from LWD measurements using the theory for a rigid plate on a homogeneous, isotropic, linear-elastic half-space. Several studies

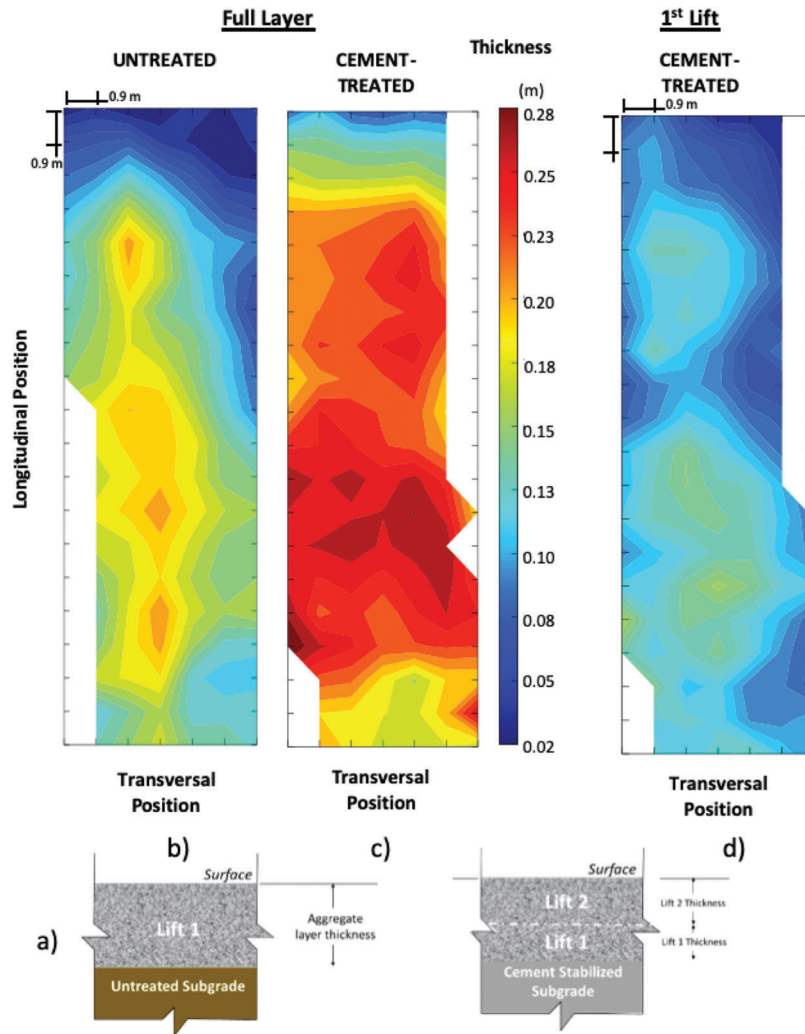


Figure 3.7 (a) Schematic of the structure of the two testing strips, and (b–d) maps of aggregate layer thickness.

(e.g., Mooney & Miller, 2009) indicate, that this approach may not yield realistic values of the modulus. As a result, only mean LWD deflections are reported here.

3.3.2.4 Air permeameter tests. Over 250 APTs were conducted on the finished aggregate at all accessible testing locations on the testing grid using the APT device developed by White et al. (2007, 2014) and discussed in Chapter 2. Location-specific values of S required for correcting the measured values for the in-situ degree of saturation were derived by linearly interpolating the data obtained from the nuclear density tests. Values of the residual saturation (S_r) and of the Brooks-Corey pore size distribution index (λ) were set to 10% and 1, respectively, based on data reported in the literature (Gupta et al., 2004) for similar geomaterials.

3.3.2.5 Aggregate surface imaging. Images of the surface of the compacted aggregate layers were taken in the field using the 5-megapixel camera of a Motorola

Moto G7 phone and processed to derive location specific values of the “Median Feature Size” (MFS). The MFS was used in this work to quantify visually observable variations in the aggregate surface, with higher MFS values reflecting a coarser appearance of the aggregate surface. The image analysis methodology developed to extract the MFS is discussed in detail by Garzon-Sabogal et al. (2024).

3.4 Results

3.4.1 Statistics of Field Data

Table 3.1 summarizes key statistics for the data collected on both strips, including mean (\bar{x}), standard deviation(s) and coefficients of variation ($CV = s/\bar{x}$). It is useful to first start examining the results for the parameters that are used in practice for quality acceptance/control. In the case of the subgrade, only LWD tests were performed at the SBRITE site. Several transportation agencies in the United States use LWD deflections and/or moduli derived from LWD data for

TABLE 3.1
Statistics of data from SBRITE site

Layer	Parameter	Strip	\bar{x}	s	CV	No. Measure	Min–Max	Range
Aggregate Layer	MFS [mm]	Untreated	5.97	0.82	0.14	137	4.14–7.83	3.69
		Cement-treated	4.36	0.67	0.15	132	3.41–6.56	3.15
	ρ_d [g/cm ³]	Untreated	2.09	0.08	0.04	46	1.87–2.21	0.34
		Cement-treated	2.20	0.06	0.03	37	1.94–2.29	0.35
	w [%]	Untreated	3.5	0.61	0.17	46	2.80–6.20	3.40
		Cement-treated	4.62	0.61	0.13	37	3.30–6.20	2.90
	S [%]	Untreated	0.48	0.13	0.28	46	0.28–0.45	0.17
		Cement-treated	0.56	0.11	0.20	37	0.36–0.76	0.40
	LWD_L [mm]	Untreated	0.48	0.29	0.60	138	0.12–1.61	1.49
		Cement-treated	0.26	0.08	0.28	133	0.16–0.57	0.41
	LWD_S [mm]	Untreated	0.40	0.16	0.41	138	0.16–0.89	0.73
		Cement-treated	0.20	0.07	0.34	133	0.12–0.57	0.45
	k_{APT} [m/s]	Untreated	1.27	8.04	0.63	73	2.81E-3–3.45E-2	3.17E-2
			E-2	E-3				
		Cement-treated	9.13	6.91	0.75	81	1.97 E-3–5.04E-2	4.85E-2
Subgrade	k_{APT} [ft/day]		E-3	E-3				
		Untreated	3,600	2,279	0.63	73	797–9,780	8,983
		Cement-treated	2,588	1,959	0.75	81	558–14,301	13,743
	LWD_L [mm]	Untreated	1.44	1.32	0.92	129	0.22–6.03	5.81
		Cement-treated	0.16	0.07	0.45	126	0.07–0.54	0.47

subgrade QA/QC (Hein et al., 2017). The use of deflections has the advantage of avoiding additional assumptions associated with calculation of the moduli. This is the approach taken by the Indiana Department of Transportation (INDOT, 2024) whose specifications identify allowable values for both the mean deflection and the maximum deflection measured at any testing station. For cement treated soils, these values are 0.27 mm and 0.31 mm, respectively. In the present study the mean LWD_L deflection measured on the cement treated subgrade (Table 3.1) is approximately 40% lower than the allowable mean deflection, and less than 5% of the 126 measurements made on the strip exceed 0.31 mm (not shown in table).

The LWD test is also used in practice for quality assessment of aggregate subbase and base layers, with varying criteria across different agencies. For aggregate layers constructed over cement-treated subgrade, INDOT specifications apply the same criterion as the one used for the underlying subgrade. Higher allowable values of the mean and minimum deflections are specified, instead, for aggregate layers over an untreated subgrade. These values vary depending on the thickness of the layer (6", 12", or 18" corresponding to 15, 30, and 45 cm) and on whether proof-rolling can be performed. For a 6" (15 cm) thick aggregate layer, the allowable mean deflection and maximum deflections are 0.51 mm and 0.57 mm when proof-rolling can be performed and increase to 0.60 mm and 0.65 mm when it cannot.

Focusing on the LWD_L data, Table 3.1 shows that the mean values for both strips fall below the specified limits. Further inspection of the full data shows that less than 20% of the LWD_L measurements for the

cement-treated strip and 17%–29% (depending on the maximum allowable value chosen) of those for the untreated strip data do not meet the specifications.

Dry density measurements are also used by several US state highway agencies for compaction control of bases and subbase aggregates. Based on a survey study by Titi et al. (2012), over 90% of these agencies require relative compaction of 95% or more. In Table 3.1, mean values of the dry density for untreated and cement-treated strip correspond to values of the relative compaction (calculated using $\rho_{dmax} = 2.25$ g/cm³ from vibratory tests on a material with similar gradation (Getchell et al., 2020), of 92% and 97%, respectively. Analysis of the full data reveals that of the measurements, 6% and 47% yield relative compaction values below 95%, for the cement-treated strip and the untreated strip, respectively.

To the authors knowledge, no state transportation agencies in the United States currently employ performance-based specifications for the saturated hydraulic conductivity (k) of aggregate layers. Nevertheless, as permeable subbases have been increasingly replaced in pavement design by free-draining subbases, recommendations have been put forward for the saturated hydraulic conductivity of such layers. The American Concrete Pavement Association (ACPA, 2007) and the Federal Highway Administration (FHWA, 2017) suggest that the laboratory permeability of free-draining subbase materials not exceed 350 ft/day ($\sim 1.2 \cdot 10^{-3}$ m/s). The FHWA document also recommends targeting in-situ values of k in the 500–800 ft/day ($\sim 1.7 \cdot 10^{-3}$ – $2.8 \cdot 10^{-3}$ m/s) range. These limits derive from construction (difficulty in compaction) and related performance (stability) issues documented in layers constructed using

coarser, more uniform aggregates that exhibit significantly higher values of k . All field measurements from the two strips exceed 500 ft/day, by as much as 30 times. All but five exceed the upper bound of 800 ft/day, and the mean values are found to be ~ 3 (untreated strip) and ~ 4.5 times (cement-treated strip) larger than this value.

The data in Table 3.1 offer insight into differences in the characteristics of the two strips. As one might expect, the results of the LWD_L tests performed directly on the subgrade show the most significant contrast between the two strips, with the mean deflection for the untreated subgrade (1.44 mm) almost an order of magnitude larger than that for the cement-treated subgrade (0.16 mm). Moreover, the LWD_L data for the untreated subgrade show significantly greater dispersion, as the coefficient of variation (0.92) is over twice that for the treated subgrade data (0.45). This indicates that because of cement-treatment, not only is the mechanical response of the subgrade improved on average, but it is also rendered more homogeneous.

Key differences are observed also in the data for the two aggregate layers. Specifically, comparison of the mean values reveals that, relative to the untreated strip, the aggregate layer of the cement-treated strip is characterized by higher water content (w), higher degree of saturation (S), higher dry density (ρ_d), a less coarse appearance (reflected in the lower MFS) and lower saturated hydraulic conductivity (k). Differences in the construction process (compaction of the aggregate in two versus one lift in the case of the cement-treated strip) as well as the presence of a stiffer underlying layer likely contributed to the more effective compaction of the aggregate on the cement-treated strip. Differences in water content, degree of saturation and MFS can likely be attributed to different sections of the stockpile from which the aggregate was obtained. For all the above measurements, the coefficients of variations are not significantly different between the two strips.

The LWD_L and LWD_S test results for the aggregate layers show the most significant difference between the two strips (Table 3.1), as the data for the untreated strip are characterized by mean values (0.48 and 0.40 mm for LWD_L and LWD_S , respectively) approximately two times greater than those for the cement-treated strip

(0.26 and 0.20 mm). The values of the coefficient of variation derived from the LWD_L and LWD_S data for the untreated strip also exceed those for the cement-treated strip (0.60 versus 0.28 for LWD_L and 0.41 versus 0.34 for LWD_S deflections). These trends align with those described above for the underlying subgrades.

Comparisons of the histograms of the LWD_L data collected on subgrade and aggregate layer of each strip are presented in Figure 3.8. Figure 3.8a shows that in the case of the untreated strip, the histogram of the LWD_L data for the aggregate layer is shifted to the left—towards smaller deflections—relative to that for the subgrade (mean value of 0.48 versus 1.44 for the untreated subgrade). The opposite trend is observed for the cement-treated strip as the histogram for the aggregate layer lies to the right of that for the subgrade (mean value of 0.26 versus 0.16 mm for the cement-treated subgrade) (Figure 3.8b). For both strips, the LWD_L data for the aggregate layer are less dispersed than those for the underlying subgrade, as reflected in the smaller CV values.

The CV values summarized in Table 3.1 highlight the varying dispersion that characterizes the parameters measured on the strips. Maps for the parameters with the highest CV values are presented in Figure 3.9 and Figure 3.10. All maps were constructed by linearly interpolating information between test locations. Areas in white are either locations where testing did not take place, or, in the case of S and k (Figure 3.10b–c), regions outside the domain within which nuclear density tests were performed (results from these tests are required to reduce the raw APT data). The first two maps (Figure 3.9), pertain to the LWD_L measurements on the two subgrades, and reinforce the points made above regarding the stiffer and more homogeneous nature of the cement-treated subgrade. Figure 3.10 shows maps of LWD_L , k , S , and MFS data for the two aggregate layers (the maps for LWD_S are omitted as these are very similar to those obtained with the larger plate). The color patterns in each map show that even within one strip, despite using the same aggregate and the same construction procedures, there is significant dispersion in the data. Causes for such spatial variability are numerous. The MFS maps in Figure 3.10d

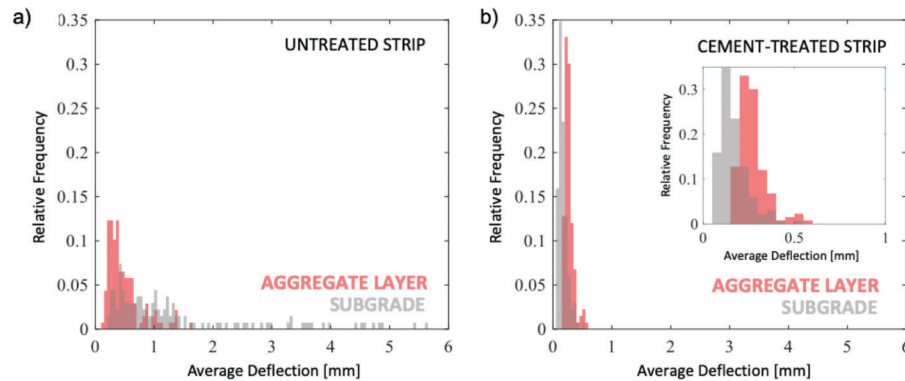


Figure 3.8 Histograms of aggregate and subgrade LWD_L data for (a) untreated, and (b) cement-treated strip.

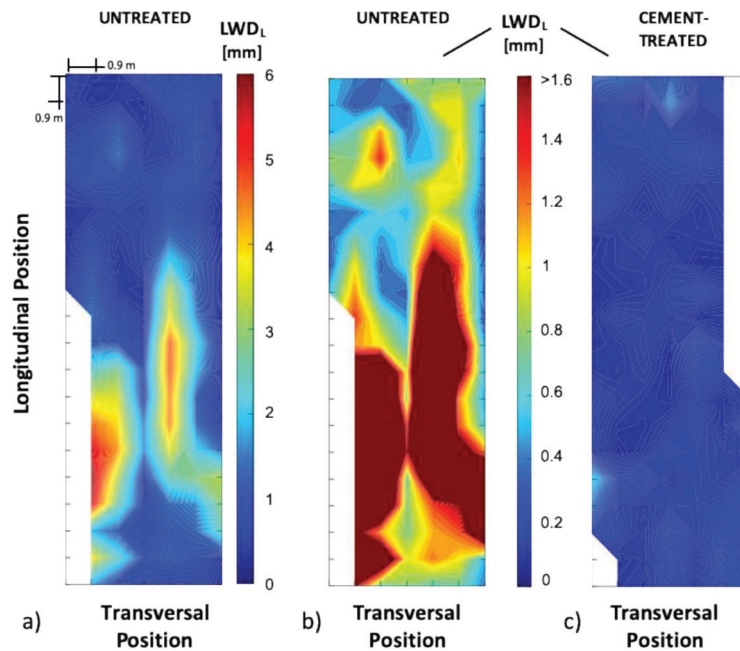


Figure 3.9 Spatial distribution of LWD_L mean deflection data from tests on subgrade of (a–b) untreated strip, and (c) cement-treated strip. Note: different scale in leftmost plot.

suggest that material heterogeneity produced by segregation during transport, stockpiling, placement, and/or compaction may be a contributing factor. In the case of k , given the relatively broad range over which S varies on both strips, additional variability in the k data may have been introduced by the correction required to account for the in-situ S .

The impact of the correction of S on the calculated values of k is clearly illustrated in Figure 3.11 which presents two maps for each strip: one of the uncorrected (raw) data (which would apply if the aggregate was dry) and one of the data processed after accounting for the in-situ degree of saturation (same as in Figure 3.10). Following correction, all values of k increase, by as little as a factor of 1.6, and by more than one order of magnitude at locations with S greater than ~ 0.65 . The most significant shift is observed in the values for the cement-treated strip, as the aggregate on this strip was characterized by higher values of S (Table 3.1). This emphasizes the importance of measuring the material's degree of saturation concurrently with APT measurements and the need to quantify its variability across a site.

Finally, it is worth noting that while both dry density and LWD deflections are used for quality control of aggregate layers, for both strips the LWD data show significantly greater dispersion than the ρ_d measurements (e.g., for LWD_L CV = 28% vs. 3% for the cement-treated strip and CV = 60% vs. 4% for the untreated strip). This suggests that additional factors other than the aggregate's state of compaction affect the results of the LWD tests. These issues are further examined in the following section through linear correlation analyses.

3.4.2 Correlations Between Measured Parameters

Pearson linear correlation analyses were performed to identify relationships between measured parameters taken two by two. Given the distinct characteristics of the two strips, data for the cement-treated and the untreated strip were considered separately. Additionally, two sets of analyses were performed for each dataset: the first included all data for each strip, the second only data from locations within the domains shown in Figure 3.10c, i.e., where all parameters were available (79 and 76 locations on the testing grid for the untreated and the cement-treated strip, respectively). As both yielded similar results, only those for the second set of data are presented and discussed here.

The outputs of each correlation analysis are the coefficient of correlation (r) and the p-value. The first measures the strength of the correlation, while the latter, which is the probability that the null hypothesis is true, measures its statistical significance. A $|r|$ value of 0.5 was used to separate weak-to-moderate from moderate-to-strong correlations. Note that this threshold is somewhat arbitrary, as the qualitative assessment of correlation coefficients varies from field to field (e.g., Akoglu, 2018). Correlations with p-values lower than 0.05 were considered significant (Chou, 1969).

To assess the uncertainty carried by the correlations analysis, independently of the above statistical significance (null-hypothesis) test, for each pair of variables, additional estimates of r were obtained using the bootstrap resampling method (Efron 1979a; 1979b). Bootstrapping is a tool that allows, in the present application, quantifying the uncertainty of the correlation coefficient using only the information contained in

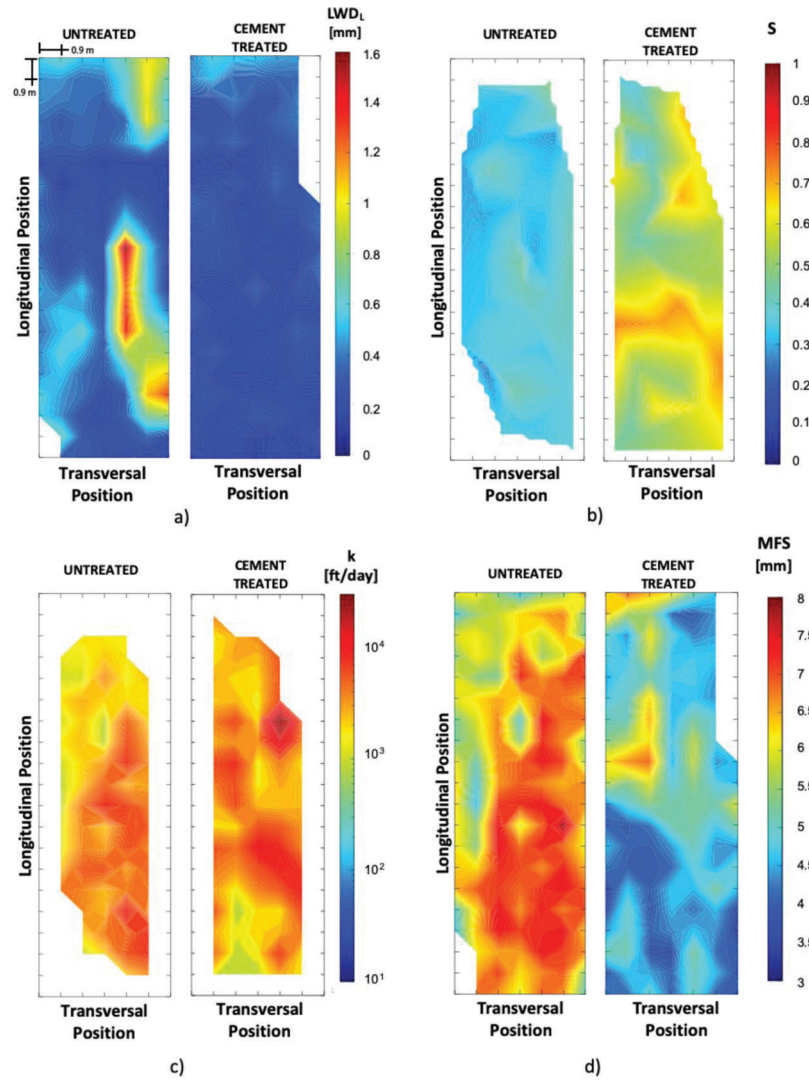


Figure 3.10 Spatial distribution of data from tests on aggregate layer of cement-treated and untreated strip: (a) LWD_L mean deflections, (b) degree of saturation, S , from nuclear density tests, (c) saturated hydraulic conductivity, k , from APT tests, and (d) median feature size, MFS .

the statistical sample without any assumptions on the population distribution (alternatively, Monte Carlo simulation would require some assumptions). This methodology has been used in several applications, such as in time series modeling (e.g., Léger, 1992), seismic hazard analysis (e.g., Lamarre, 1992) and geotechnical uncertainty analysis (e.g., Bourdeau & Amundaray, 2005). Figure 3.12 illustrates the bootstrapping procedure used in this work. For each pair of parameters (variables A and B), 200 correlation analyses are performed, each of which is based on m ordered pairs, where m is the number of locations within the data set where both variables are known. In each analysis, the m ordered pairs are randomly selected from the original data set allowing for repetition. For each dataset, the output of the analysis is a simulated histogram of the 200 numerically generated r values (Figure 3.12), from which the mean value and

coefficient of variation of the correlation coefficient, r , are calculated.

Figure 3.13 and Table 3.2 summarize the results of the correlation analyses (see also plots in Appendix B). The horizontal and vertical lines in the diagram in Figure 3.13 identify the variables included in each correlation analysis, while the semi-circles at each intersection depict the outcome of the analysis for each dataset. A blue semi-circle identifies the 12 correlations with r higher than 0.50 and $p < 0.05$ and the corresponding r values and p -values are summarized in Table 3.2. Orange is used to identify correlations for which at least one of the above conditions is not met. Table 3.2 also includes the mean values obtained from bootstrap resampling which are found to be consistent with the results of the linear regression analyses. The small values of the coefficients of variation of r obtained using bootstrapping reinforce confidence in the results.

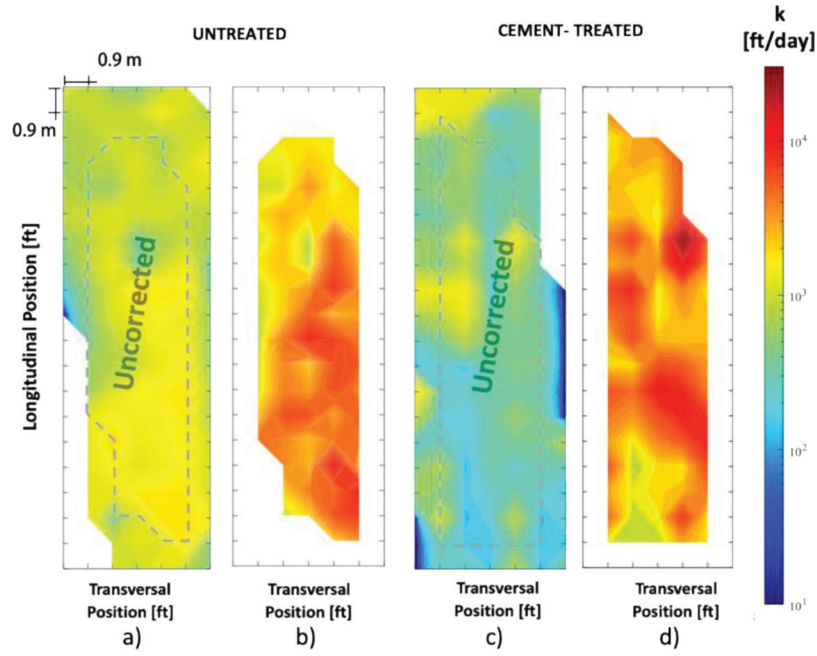


Figure 3.11 Spatial distribution of uncorrected and corrected data of saturated hydraulic conductivity, k , from APT tests: (a–b) untreated, and (c–d) cement-treated strip.

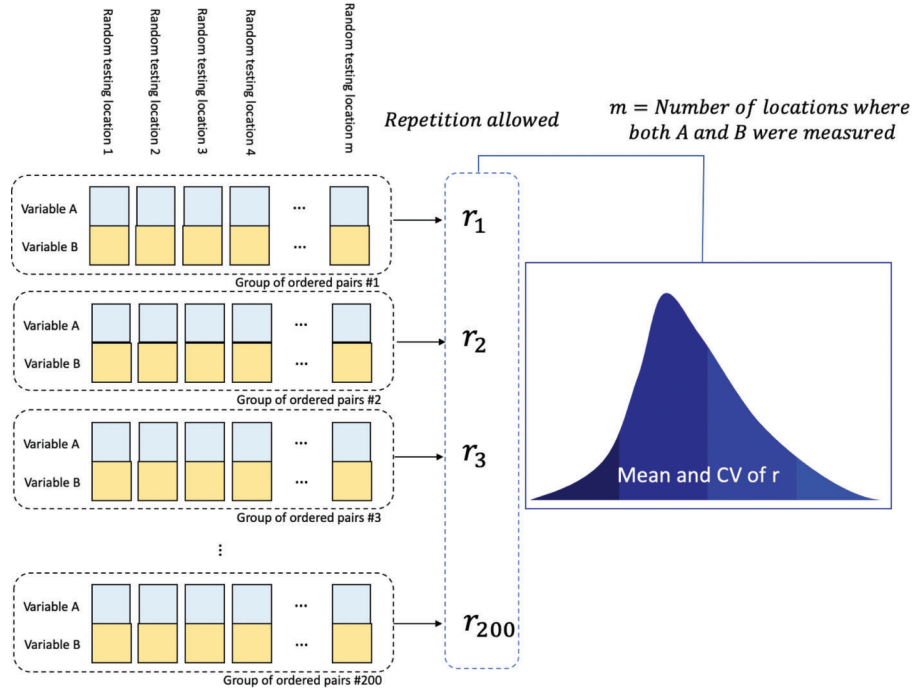


Figure 3.12 Schematic of bootstrapping procedure followed to generate the data shown in Table 3.2.

Note that the ranges shown in Figure 3.13 differ from those in Table 3.1, as the regression analyses use only the data from locations within the domains shown in Figure 3.10.

Strong correlations are observed for both strips between the degree of saturation of the aggregate and its water content ($r = 0.91$ and 0.74 , for the untreated and cement-treated strip, respectively), and between

degree of saturation and dry density ($r = 0.59$ and 0.84). This is to be expected as the results of the nuclear density tests (ρ_d and w) are used to calculate S . For the cement-treated strip, both w and S are found to be moderately positively correlated to the thickness of the aggregate layer, likely a reflection of the construction process. For the cement treated subgrade, ρ_d and w are also found to be correlated. This reflects the relationship

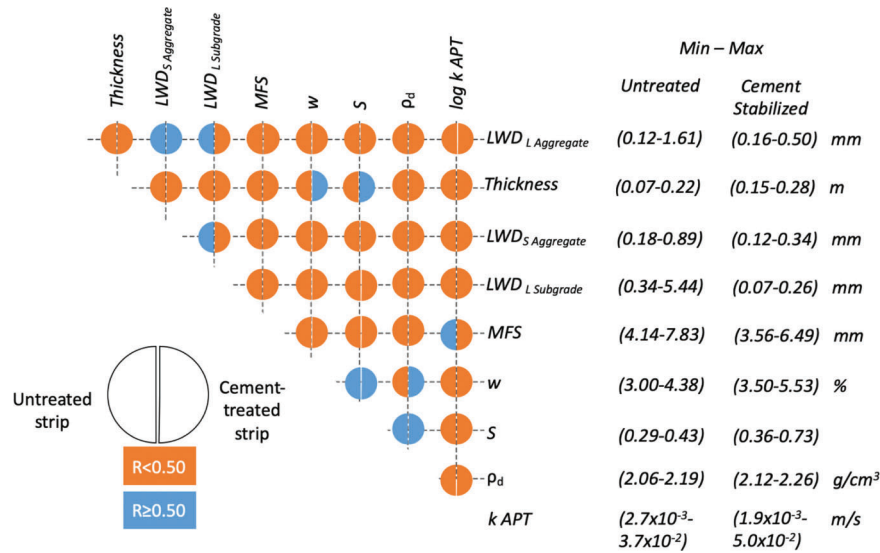


Figure 3.13 Result summary of linear correlation analyses.

TABLE 3.2
Results of correlation analyses and bootstrap resampling

Parameter	Correlated Parameter	Dataset	Linear Correlation		Bootstrap Resampling	
			r	p-value	Mean r	CV
LWD_L on Aggregate Layer	LWD_S on aggregate layer	Cement-treated strip	0.67	1e-11	0.65	0.17
	LWD_L on aggregate layer	Untreated strip	0.91	3e-30	0.91	0.03
	LWD_L on Subgrade	Untreated strip	0.69	4e-12	0.69	0.10
$k APT$	LWD_S on aggregate layer	Untreated strip	0.60	7e-9	0.62	0.14
	MFS	Untreated strip	0.85	4e-22	0.85	0.04
w	S	Cement-treated strip	0.91	2e-30	0.91	0.02
		Untreated strip	0.74	2e-14	0.75	0.06
		Cement-treated strip	0.84	6e-22	0.84	0.04
ρ_d	S	Untreated strip	0.59	3e-8	0.58	0.16
w		Cement-treated strip	0.54	4e-7	0.54	0.16
Thickness		Cement-treated strip	0.57	3e-8	0.56	0.15
	w	Cement-treated strip	0.58	3e-8	0.57	0.13

between these two properties in this range of water contents, as established by laboratory tests (Getchell et al., 2020).

For the untreated strip alone, both the LWD_L and LWD_S deflections measured on the aggregate surface show relatively strong correlation with the result of the LWD_L test performed on the underlying subgrade ($r = 0.69$ and 0.60) This indicates that the LWD measurements reflect the composite response of the aggregate and underlying soil, and that the deformability of the untreated subgrade plays a significant role on the overall deformation. No such correlation is observed in the case of the cement-treated strip ($r < 0.14$). This reflects the greater homogeneity in the subgrade conditions promoted by the treatment (Table 3.1) and the limited contribution to the measured deflection by the stiff subgrade layer.

For both subgrade conditions, LWD_L and LWD_S deflections measured on the aggregate layer are found to be strongly correlated. For the untreated strip this is expected as both measurements are controlled by the deformation on the underlying subgrade (see above). In the case of the of cement-treated strip this is because both tests provide a measure of the compressibility of similar soil volumes at the same location.

From the data for the untreated strip, a strong correlation ($r = 0.85$) emerges between MFS and $\log(k)$, suggesting that material heterogeneity is a major contributor to the over 10-fold variation in k measured across this strip. A weaker correlation ($r = 0.45$) between these same two quantities is found for the aggregate on the cement-treated strip. Given that the aggregate layer of the cement treated strip is characterized by much higher values of S (0.36–0.73,

Figure 3.10), it is hypothesized that this may be due to the additional uncertainty introduced by the correction for S , which plays a rapidly increasing role as S increases (White et al., 2014). Further discussion on the critical importance of this correction is provided below.

Figure 3.13 also highlights the absence of strong correlation, as measured by values of r lower than 0.50, between variables that might have been expected to be linked. For both strips only a weak negative correlation ($r = -0.36$ to -0.17) is found between LWD (both large and small plate) deflections measured on the aggregate surface and ρ_d values derived from the nuclear density tests. As discussed above, both measurements are used in practice to assess the quality of compaction of aggregate layers. The lack of a strong correlation between ρ_d and $LWD_{L,S}$ deflections may be expected for the untreated strip, given the above discussed impact of the underlying untreated subgrade on the LWD deflections measured at the aggregate surface. Relatively low values of r (-0.26 and -0.36 for ρ_d versus LWD_L and LWD_S , respectively) are, however, obtained also for the cement-treated strip. For this strip, the LWD measurements are thought not to be significantly affected by the response of the subgrade conditions and therefore should represent only the response of the aggregate layer.

Given the arbitrary nature of the 0.5 threshold value chosen for $|r|$, it is of interest to further examine a few pairs of variables for which the correlation coefficient falls just below this threshold. One such relationship is that between $\log(k)$ and S . For both the untreated and the cement-treated strip, there is a positive correlation between these two parameters with r equal to 0.48 (untreated strip) and 0.41 (cement-treated strip). A correlation between these two parameters should not be

expected, as the value of k derived from the APT is intended to represent the material's saturated hydraulic conductivity, and therefore should not be affected by the in-situ S . Reflecting the different ranges of the in-situ S , the data for the two aggregate layers have almost no overlap, and no correlation between these same parameters is observed when the data are analyzed as a whole (Figure 3.14a). This, however, does not consider differences between the two strips, in particular, the larger values of MFS (indicative of a coarser appearance of the surface) that characterize the aggregate layer of the untreated strip relative to that of the cement-treated strip (Figure 3.14f–g). As the MFS was seen above to have a strong correlation with $\log(k)$, additional linear correlation analyses were performed on smaller datasets comprising measurements at locations on the two strips where the MFS falls in small, specified ranges (MFS = 3.5–4 mm, 4–4.5 mm, 4.5–5 mm, etc.). The results of the analyses for the datasets that contain at least 20 data points are presented in Figure 3.14b–e. The r values between 0.68 and 0.85 demonstrate a strong correlation between $\log(k)$ and S , once the effects of material heterogeneity are accounted for. This translates into ~ 10 -fold increase in the value of k calculated for materials with the same MFS for S ranging between ~ 0.3 and 0.7 . This result raises questions about the validity of the correction for the in-situ degree of saturation, S , in the derivation of the saturated hydraulic conductivity, a critical step in the interpretation of the APT data.

3.4.3 Impact of Statistical Sample Size

As illustrated in Figure 3.6, characterization of the two strips relied on tests conducted with high spatial

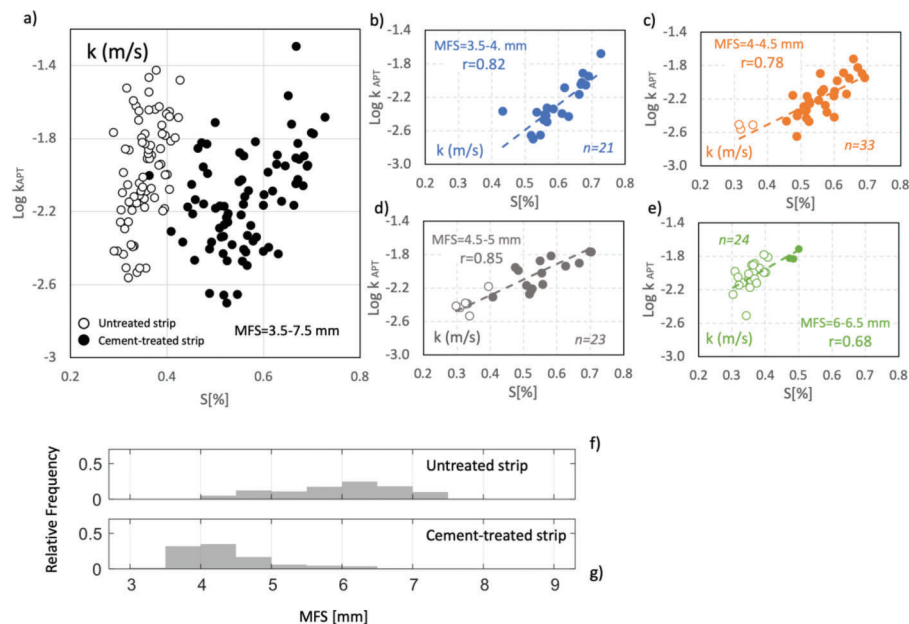


Figure 3.14 Relationship between in-situ S and $\log k$ of aggregate layer (k in ft/day). (a) All data for two strips; (b–e) data for specific MFS intervals (empty and full symbols denote data for untreated and cement-treated strip, respectively); and (f–g) aggregate MFS distributions for untreated and cement-treated strip.

density. The availability of such a large sample offers the opportunity to address two questions related to sample size. First, how representative is the estimate of the population obtained from a sample of size n compared to that obtained from the larger sample? Second, what is the probability of correctly assessing whether a layer complies with QA/QC specifications based on a sample of size n , and how does this depend on the specific acceptance criterion used?

Both questions are addressed here applying a stochastic approach and assuming that the large sample from the testing program conducted at the site provides the best representation of the population. Note that while the analysis presented here focuses exclusively on LWD_L data, a similar approach can be applied to the other data collected on the strips. Sample size is expressed both in absolute terms (number of measurements n used to characterize the 18 m \times 6 m area of each strip), as well as in normalized form, as the number of measurements per unit of area (meas./m²).

The approach employed to answer the first question can be summarized as follows. From all measurements collected on a given layer (aggregate or subgrade), a subset of size n is randomly selected and the mean of this sample, termed $LWD_{L,n}$, is calculated. This process is repeated 200 times per sample of size n , with n varying from 1 to the full size of the original LWD_L data set (~ 130 , see Table 3.1). For all sub-samples of size n , the mean ($\overline{LWD_{L,n}}$) and standard deviation ($\sigma_{LWD_{L,n}}$) of the 200 mean values ($LWD_{L,n}$) are calculated. Figure 3.15a–d present the results of this analysis where all 200 mean values are plotted for each

sample size n . The four plots pertain to the aggregate layer and subgrade of the cement-treated strip, and the aggregate layer and subgrade of the untreated strip, respectively. The colors in the figure represent the *standard score* of each $LWD_{L,n}$ value, calculated using Equation 3.1.

$$\text{Std. Score} = \frac{LWD_{L,n} - \overline{LWD_{L,n}}}{\sigma_{LWD_{L,n}}} \quad (\text{Eq. 3.1})$$

Points in orange, for instance, represent values of $LWD_{L,n}$ that for any given n are one standard deviation away from $\overline{LWD_{L,n}}$. While across the four plots, as expected, $\overline{LWD_{L,n}}$ is not affected by the sample size n , as n decreases the mean values of the samples show greater dispersion.

A different representation of these same data is provided in Figure 3.15e–h. Here, the vertical axis represents the fraction of $LWD_{L,n}$ values, that, for each n , differs from $\overline{LWD_{L,n}}$ by less than 5% (green markers), 10% (blue markers) or 20% (red markers). These fractions express the confidence level in the estimate of the population mean provided by a sample of size n . For example, for the aggregate layer on the cement-treated subgrade (Figure 3.15e), a minimum of ~ 45 measurements (~ 0.4 meas./m² or 2 meas./5 m²) is required to ensure with 90% confidence that the error in the estimate of the mean falls below 5%. With the same confidence level, the minimum sample size n decreases to ~ 15 (~ 0.1 meas./m² or 1 meas./10 m²) and ~ 5 (~ 0.025 meas./m² or 1 meas./40 m²), if a larger

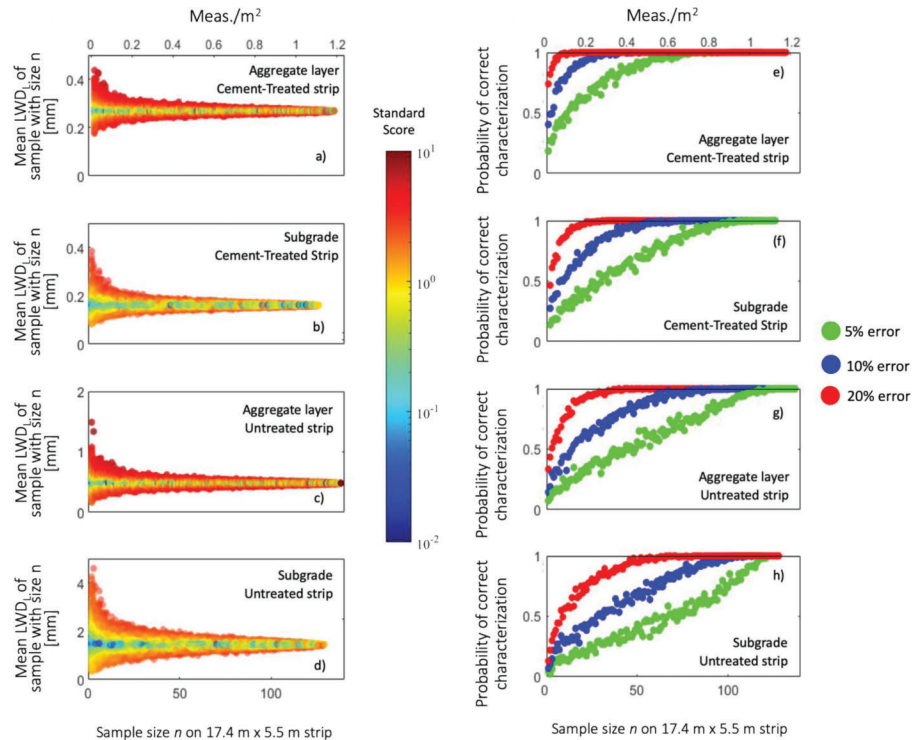


Figure 3.15 Effect of sample size on average characterization of strips.

margin of error, 10% and 20%, respectively, is deemed acceptable.

Note that these numbers are specific to this dataset, and as shown in Figure 3.15, increase for datasets with more variability, i.e., higher *CV* (see Table 3.1). For the aggregate on the untreated subgrade (Figure 3.15g), for example, they are approximately doubled. Overall, these results highlight that the estimate of the population mean based on smaller samples carries great uncertainty.

A similar approach can be employed to examine the effects of sample size *n* on the assessment made on whether a constructed layer complies with given specifications. This is illustrated here for both the subgrade and the aggregate layer of the cement-treated strip, using as a guideline the specification developed by INDOT (2024) for these types of layers. Again, samples comprising *n* measurements are selected randomly from the original data set. Two hundred such samples are created for each *n* value, with *n* varying from 1 to the full size of the *LWD_L* data set. For each sample, six different criteria are used to assess whether the layer is *Passing* or *Not Passing*. The first criterion requires that the mean of a sample of size *n* (*LWD_{L,n}*) does not exceed the 0.27 mm limit for the average pointwise

deflection used in the INDOT specifications. The remaining criteria are based on a certain percentage (95%, 90%, 75%, 50%, and 40%) of the measurements in each sub-sample staying below this same threshold.

Table 3.3 summarizes the result of applying these six criteria to the sample comprised of all *LWD_L* tests performed on the strip. Both the aggregate and the subgrade “pass,” based on the first criterion, as the mean values for both layers (see Table 3.1) are below 0.27 mm. When applying the other five criteria the assessments transition from “passing” to “not passing” as the acceptance criterion requires that at least 75% (aggregate layer) and 95% (cement-treated subgrade) of the measurements are less than 0.27 mm. The difference between the two layers reflects the different distributions of the two populations.

The results of the stochastic analysis are summarized in Figure 3.16. In each plot, the vertical axis represents the percentage of samples of size *n* that matches the qualification of the layer based on the full dataset (Table 3.3). Green and red colors identify such qualification (*Passing* or *Not Passing*, respectively). In other words, the height of the profile expresses the probability of correctly assessing the layer, while the color of the profile represents the assessment result.

TABLE 3.3
Assessment of layers of cement-treated strip based on six different acceptance criteria

	Mean of Measurements	Percent of Measurements <0.27 mm				
	<0.27 mm	95%	90%	75%	50%	40%
Aggregate Layer Cement-Treated Strip	Passing	Not Passing	Not Passing	Not Passing	Passing	Passing
Subgrade Cement-Treated Strip	Passing	Not Passing	Passing	Passing	Passing	Passing

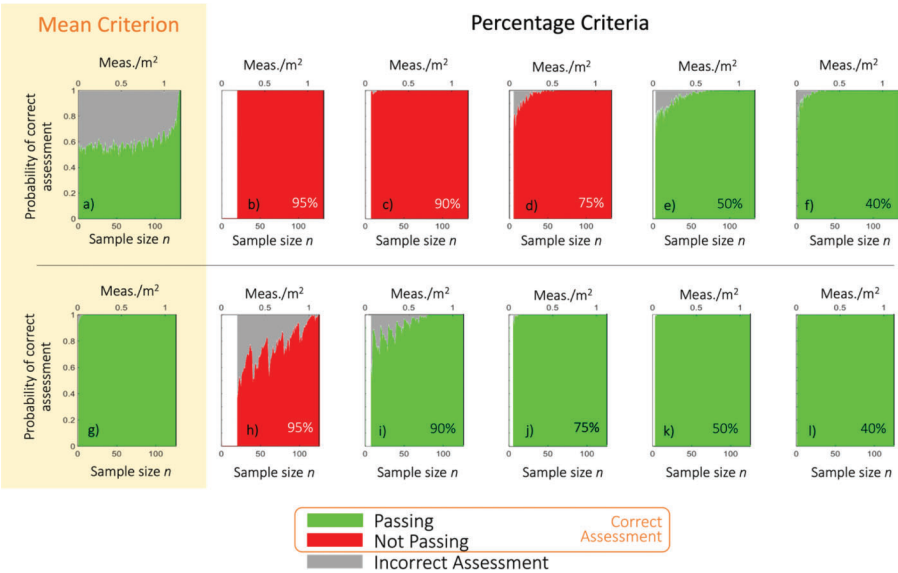


Figure 3.16 Effect of sample size on the correct assessment according to different criteria of (a–f) aggregate, and (g–l) subgrade of cement-treated strip.

The white areas reflect sample sizes for which a given criterion cannot be applied (e.g., the criterion requiring that at least 95% of the measurements are under a given threshold cannot be applied for $n < 20$). The small oscillations seen in the plots in Figure 3.16 are of numerical origin in the simulation algorithm.

The results show that when applying the first criterion based on the mean of the sample to the cement-treated subgrade (Figure 3.16g), the probability of correctly assessing this layer is very high ($>90\%$), and independent of the sample size. This is due to the uniform conditions promoted by the treatment. For the overlying aggregate (Figure 3.16a), unless the sample is very large ($\sim >1$ meas./m²), there is, instead, a less than 60% probability of correctly assessing the aggregate layer.

From a practical perspective, it is of interest to focus on the left-most portion of each of the graphs presented in Figure 3.16, as in the field QA/QC generally relies on a limited number of tests (e.g., INDOT specifications state that acceptance of chemically modified soils or aggregate should be based on three LWD tests obtained at a random station). Figure 3.16 shows that for such small sample sizes, there can be significant uncertainty in assessing the two layers, depending on the acceptance criterion used. Focusing on the “percentage criteria,” the figures illustrate that, for small sample sizes, the probability of incorrectly assessing the layers is as high as 20% (aggregate layer, Figure 3.16d–e and 50% (cement-treated subgrade, Figure 3.16h–i). Note that the highest uncertainty corresponds to the case for which the fraction of the measurements that is required to fall below the 0.27 mm threshold is close to the percentage of measurements in the full data set that meet this specification (60% and 94% for the aggregate and cement-treated subgrade, respectively).

The results displayed in Figure 3.16 and the above conclusions are specific to the datasets examined, as well as to the acceptance criteria considered. For different populations, the degree of uncertainty associated with any given criterion will change. These results do, however, demonstrate that small samples are not generally reliable for quality control. They also illustrate that criteria based on the mean of a sample can lead to “missing” information pertaining to local problematic areas, which are often the source of damage in pavement systems. These issues can compromise efforts invested in quality assessment. These observations highlight the importance of assessing uncertainty evidenced by the dispersion in the data as part of a quality assessment campaign. In practice this would require investing in rapid non-destructive tests

that can be performed in large number and at high spatial density, and formulating guidelines in probabilistic terms (e.g., by placing a parameter-dependent limit on the coefficient of variation). This issue will require further research.

3.4.4 Additional Tests on First Aggregate Lift of Cement-Treated Strip

As discussed above, the aggregate layer on the cement-treated strip was constructed in two lifts. Following compaction of the first lift, LWD_L and LWD_S tests were performed at locations on the testing grid. Key statistics for these measurements, are summarized in Table 3.4. They are generally consistent with those reported above for the full aggregate layer. While the testing program on the lift also included APT tests, they are not discussed here as they could not be corrected for the in-situ degree of saturation.

Correlation analyses were performed between these two parameters and the LWD_L and LWD_S data collected on the finished layer and the underlying subgrade. As above, correlations with $|r|$ value of 0.5 or greater are considered moderate-to-strong, and a maximum p-value of 0.05 is used to determine whether they are significant. As expected, and consistent with what was observed from the analysis of the data on the finished aggregate layer, LWD_L and LWD_S measurements at the same locations on the 1st lift are found to be strongly positively correlated ($r = 0.90$, Table 3.5). Relatively strong correlations ($r = 0.71$ – 0.73) are also identified between LWD_L and LWD_S deflections from tests on the 1st lift, and LWD_L and LWD_S data collected at the same location on the grid on the finished layer. This supports the notion that for the cement-treated strip LWD deflections are controlled by deformations in the aggregate layer.

TABLE 3.5
Results of second set of correlation analyses (correlations with $|r| > 0.5$ and $p < 0.05$)

Parameter	Correlated Parameter	r	p-value
LWD_L on 1st Lift	LWD_S on 1st lift	0.90	7.39e-24
LWD_L on Finished Aggregate Layer	LWD_L on 1st lift	0.73	5.25e-12
LWD_S on Finished Aggregate Layer	LWD_S on 1st lift	0.71	5.12e-11
LWD_L on Finished Aggregate Layer	LWD_S on 1st lift	0.71	4.94e-11
LWD_S on Finished Aggregate Layer	LWD_L on 1st lift	0.72	2.58e-11

TABLE 3.4
Statistics of data from tests on first aggregate lift SBRITE site

Property	\bar{x}	s	CV	No. Measurement	Min-Max	Range
LWD_L [mm]	0.27	0.12	0.45	127	0.12–0.80	0.68
LWD_S [mm]	0.19	0.09	0.49	67	0.07–0.63	0.56

As observed for the measurements on the finished layer, regression analyses between the LWD_L and LWD_S data collected on the 1st lift and deflections measured at the same locations on the underlying subgrade yielded r values below 0.5.

3.4.5 Investigation of APT Repeatability

Additional testing with the APT was done to assess the repeatability of the testing method. The results from two experiments are reported here. The first took place on a single day and involved repeat measurements in rapid succession at three locations with and without repositioning the APT apparatus. The second experiment involved single measurements at 29 locations (11 and 18 on the cement-treated and untreated strip, respectively) on 2–5 different dates between August and December 2020. Values of k derived from all these measurements were not corrected for the in-situ degree of saturation, as it could not be assumed that S remained constant. As a result, only the uncorrected data are reported here.

Figure 3.17a shows the locations selected for the first experiment: two (identified by symbols G5 and R5, based on their position on the grid) on the cement-treated strip and one (O3) on the untreated strip. Figure 3.17b summarizes the data collected at these three locations. A dashed outline is used to group a series of measurements that were performed without moving the

equipment. At the location on the untreated strip these repetitions were performed switching between orifice B and orifice C. On the cement-treated strip all measurements were performed, instead, using orifice B. Following these repeat measurements, the equipment, including the pad, was lifted and repositioned, making all efforts, facilitated by the presence of the painted grid, to target the exact testing location, and new measurements were collected.

Mean, range, and maximum and minimum values are summarized in Table 3.6. When conducting measurements without repositioning the equipment (columns 3–5 in Table 3.6) the measurements are repeatable within 25–50 ft/day. Note that the calculation for the O3 location includes data collected with two difference orifices. The range for this location is reduced to ~25 ft/day when data from a single orifice are considered. See Section 4.3 and Figure 4.14 for further discussion of the role played by the orifices and of the importance of verifying their correct calibration. Calibration procedures used in this work are summarized in Figure 2.3.

Significantly greater variation in the measured values of k (211–634 ft/day) is observed when lifting and repositioning the APT apparatus (including the pad) between measurements, as illustrated in columns 6–8 in Table 3.6. This may reflect local variability in k , as the apparatus may not be repositioned in the same spot, as well as variability in the testing procedure.

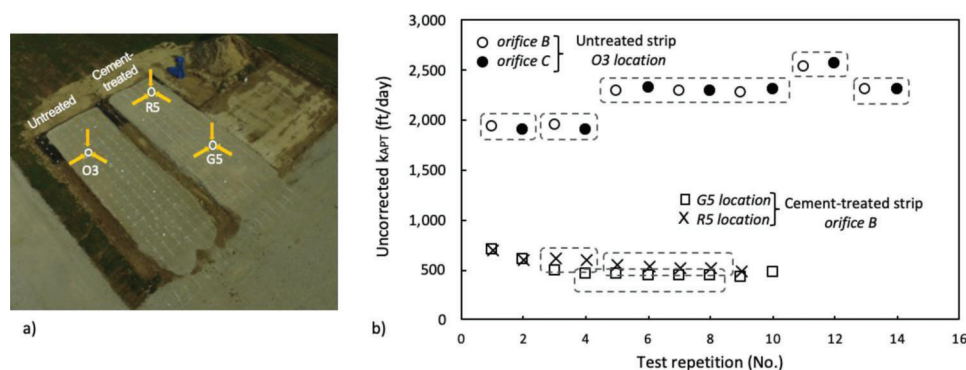


Figure 3.17 (a) Locations, and (b) results of single day repeat measurements.

TABLE 3.6
Summary statistics from single day repeat measurements

Strip	Location	Measurements Without Repositioning Equipment (Longest String)			Measurements Repositioning Equipment (Mean From Each String)		
		Mean (ft/day)	Range [Min–Max] (ft/day)	No. Measurement	Mean (ft/day)	Range [Min–Max] (ft/day)	No. Measurement
Untreated	O3	2,279	50 ¹ [2,254–2,304]	6	2,186	634 [1,906–2,540]	5
Cement-treated	G5	435	25 [425–450]	5	509	260 [419–679]	6
Cement-treated	R5	518	37 [503–540]	4	573	211 [472–683]	5

¹Based on measurements with both orifices B and C.

Figure 3.18 shows locations where the second set of tests were performed between August and December 2020. A summary of the uncorrected values of k obtained at each location are provided in Figure 3.19a and Figure 3.19b for the untreated and cement-treated strip, respectively. These data exhibit greater variability as measured by the values of the range: at 70% of the locations, the range in k exceeds 350 ft/day, and is as high as 1,103 ft/day. At a third of the locations the maximum value of k is over twice the minimum value. The greater variability of these values relative to the data reported in Table 3.6 can be attributed to

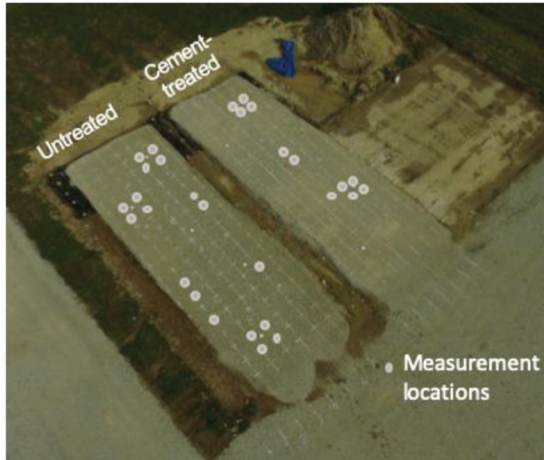


Figure 3.18 Locations where repeat measurements were performed between August and December 2020.

differences in the environmental conditions at the time of testing and, more importantly, to changes in the degree of saturation of the tested material during the 4-month period over which the measurements were performed. While the above discussed variability in the testing procedure, and the local variability in the material properties create some randomness, the data generally support this hypothesis. Focusing on the cement-treated strip, consider, for example, the data collected on November 7 (in gray) and November 24, 2020, (in gold). The first are consistently the highest values of k (uncorrected) measured at each location, while the latter tend to be at the low end. Data from the nearby Purdue Airport weather station indicate dry conditions with no rain for at least 8 days prior to November 7, and approximately 1 inch of rain between November 22 and November 24. The relative values of k (uncorrected) are consistent with a higher degree of saturation of the aggregate layer at the time of the second set of APT tests. These observations highlight the sensitivity of the APT data to the degree of saturation of the material tested and emphasize the importance of measuring this property concurrently with the APT testing program.

3.4.6 Investigation of Performance of Geotextile Separator Layer

As discussed above, a nonwoven needle-punched geotextile made of polypropylene staple filaments, with mass per area of 203 g/m², GEOTEX® 601 (see product

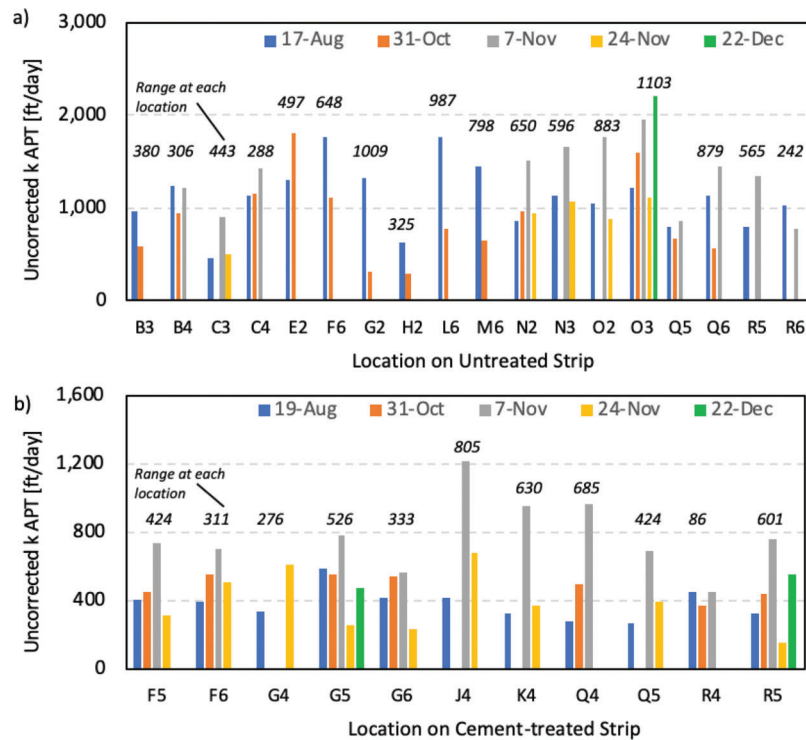


Figure 3.19 Results of measurements performed between August and December 2020 at select locations on (a) untreated, and (b) cement-treated strip.

data sheet in Appendix A) was laid on the eastern most side of the strips, covering approximately 1/4 of the subgrade (Figure 3.5a). This geotextile meets the Class 2 survivability requirements based on Holtz et al. (2008) (see also Getchell et al., 2020). It also qualifies as a Type 2A geotextile for “underdrains, subsurface drains, and filtration applications” per INDOT Standard Specification 918.02(b). INDOT Office of Materials Management does indeed list the Propex GEOTEX 601 in the list of approved geosynthetics for this type of application.

Following completion of the testing program described in this report, additional tests were performed on the strips in October 2020. These included falling weight deflectometer (FWD) tests at most locations on the grid and cyclic Automated Plate Loading tests (APLT) (Pajo et al., 2023) at nine locations on the testing grid. Two of these locations were on the portion of the strips underlain by the geotextile. APLT tests involved the application of 5,000 loading cycles. In November 2020, samples of the geotextile were exhumed at 12 locations (GX1-GX12) from trenches on both strips, including in correspondence to the locations of the cyclic plate load tests. Figure 3.20a–b shows the sampling trench on the untreated strip before and after the samples were obtained. In general, significant damage, in the form of bursts, perforations and abrasions, was observed on all samples from both strips, including those obtained outside the location of

the cyclic load tests. Figure 3.20c shows an example of the extensive damage observed on the samples, with detail of one of the perforations shown in Figure 3.20d. A complete documentation of the damage is provided by the images included in Appendix C.

Based on these observations, it can be concluded that the geotextile did not survive and could, therefore, not fulfill its intended functions as separator/filter. A higher-class product is required for this type of application.

3.4.7 Investigation of Compactor Vibratory Effects

Two semiconductor strain gage earth pressure cells (Geokon, 4800 Series, capacity 2.5 MPa) were installed on the subgrade of the cement-treated strip to quantify compactor vibratory effects. Figure 3.21 illustrates the installation of the cells along the south edge of the strip (approximately 16' and 38' ft from the east end). Figure 3.22a shows placement of the aggregate over the strip and highlights the location of the two pressure cells. Figure 3.22b shows the CAT CS44B smooth drum roller as it compacts the aggregate over one of the cells. A National Instruments (NI 6259) data acquisition card was used to acquire the earth pressure cell signals. It was mounted along with the pressure cell power supply, a laptop computer and a portable generator on a small cart (Figure 3.22c), which was positioned in immediate proximity to the strips.

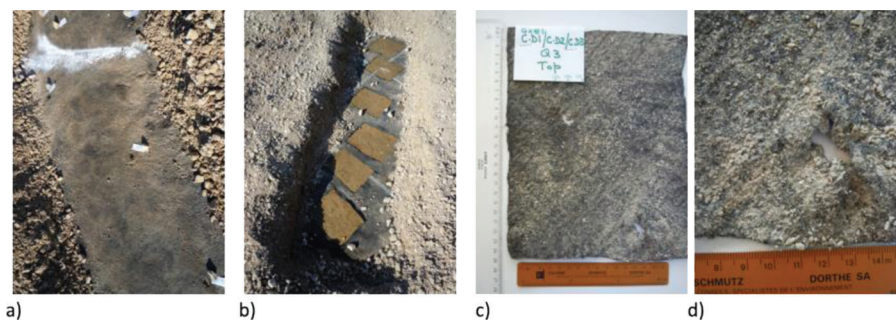


Figure 3.20 Sampling trench on untreated strip: (a) before, and (b) after exhuming the geotextile samples. (c) Exhumed geotextile sample at one location on same strip, and (d) detail of perforation. Markers shown in part (a) identify locations for damage inventory.

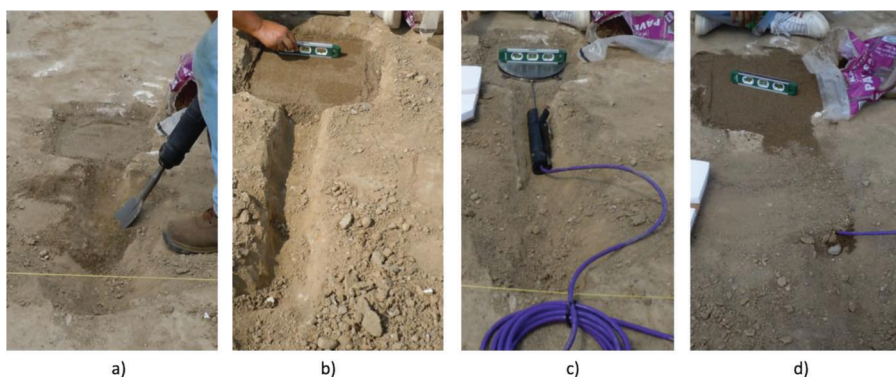


Figure 3.21 Installation of pressure cells: (a) excavation of housing for pressure cell in cement treated subgrade; (b) leveling of the paver sand following hand compaction with a tamper; (c) placement and leveling of the pressure cell; and (d) leveling of the overlying sand.

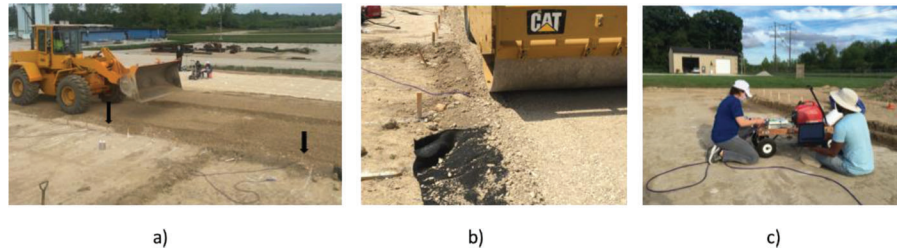


Figure 3.22 (a) Placement of aggregate on strip (black arrows identify position of two pressure cells); (b) compaction of aggregate over one of the pressure cells; and (c) cart with power supply and data acquisition equipment.

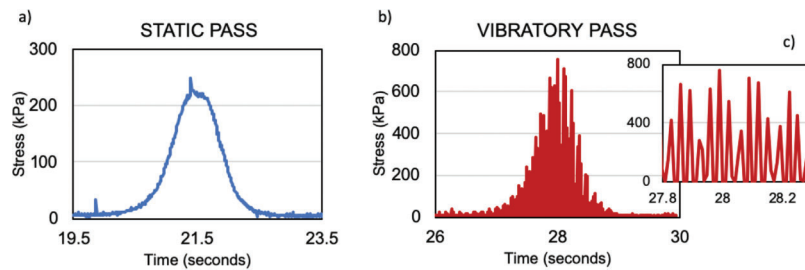


Figure 3.23 Examples of signal collected at one of the pressure cells during (a) a static pass, and (b–c) a vibratory pass.

Along the southern portion of the strip where the earth pressure cells were mounted aggregate compaction procedures differed from those described in Section 3.2. Specifically, the aggregate was compacted with four static passes (as the compactor moved forward and backward two times), followed by four vibratory passes, and by 4 additional static passes. Figure 3.23 shows examples of the variation of the signal measured by one of the cells as the CAT CS44B compactor approaches and moves past the cell in static (Figure 3.23a) and in vibratory (at maximum centrifugal force and $f = 30$ Hz) mode (Figure 3.23b–c). Similar data were collected during the other passes with the same mode. Average values of the maximum normal stress over the first four static passes and the four vibratory passes were 228 kPa and 700 kPa, respectively, corresponding to a force ratio (FR) of 3.1. This parameter is used to account for compactor vibratory effects through an equivalent static force. As discussed by (Getchell et al., 2020), consideration of vibratory effects on the applied loads is critical to the evaluation of the stability of granular layers, and to the appropriate design of compaction procedures in the field.

4. FIELD TESTING AT CONSTRUCTION SITES

4.1 Introduction

This chapter summarizes the results from field testing programs (light weight deflectometer [LWD], and air permeameter [APT] tests complemented by sand cone or nuclear density [ND] measurements and imaging of aggregate surface) conducted at three construction sites in Indiana—the Cherry Lane extension project in West Lafayette, the reconstruction of SR 46 in proximity to Bloomington, and the widening of I-65 in Lebanon. At all three sites testing focused primarily on the 6 in. (~15 cm)

layer of compacted IN #53 aggregate constructed over the cement-treated subgrade, which, per INDOT specifications, was intended to function as a separator layer. Depending on the site, additional tests were performed on the underlying cement-treated subgrade and/or on the overlying drainage layer.

The primary goal of testing at the three sites was to identify practical advantages and/or issues associated with field deployment of the LWD and the APT and with the use of these techniques for QA/QC of compacted aggregate layers. While there is some experience with the use of the LWD for compaction control in Indiana, this project was the first exploration of the use of the APT for measuring the permeability of aggregates in-situ. Additionally, as discussed in more detail in the following sections, tests at the three sites sought to investigate specific issues related to the applicability of the APT and the interpretation of the APT data that arose as the project progressed, and address questions related to the accuracy and repeatability of the test. Results and observations from the first two sites also served to inform and guide the design of the experimental program performed on the strips constructed at the SBRITE site (Chapter 3), with the data from all three sites also providing the opportunity for comparison to the results obtained testing the SBRITE strips. Table 4.1 provides a general overview of the testing program conducted at the three sites. Detailed results are presented in Section 4.2–Section 4.4.

4.2 Site 1: Cherry Lane, West Lafayette, IN

Site 1 is in West Lafayette, Indiana (Figure 4.1). The project, completed in late summer of 2019, involved the construction of the intersection between Cherry Lane and US 231, including the addition of turning lanes on

TABLE 4.1

Summary of field-testing program at Sites 1–3 (numbers represent tests performed which do not include repeat measurements at the same testing location)

Site	Layer	LWD_L	LWD_S	APT	ND	Sand Cone	Surface Images
Cherry Ln.	#8	44	44	19	–	–	–
West Lafayette	#53	44	44	40 +4 ¹	–	4 +3 ¹	43
SR 46 Bloomington	#53	76	76	75 +20 ²	–	4	72
I-65 Lebanon	Cement-treat. perm. base	120	–	–	–	–	–
	#53	101	107	96	45	–	107
	Cement-treat. perm. base	–	–	34	–	–	–
	Open-graded asphalt	–	–	10	–	–	–

¹Tests performed prior to compaction.

²Tests performed with orifice C.



Figure 4.1 Site 1 location.

US 231. The concrete pavement was constructed over a subbase formed by a 3" layer of INDOT #8 compacted over a 6" thick layer of INDOT #53, placed directly over the cement treated subgrade. Tests on both unbound aggregate layers, herein referred to as IN #8 and IN #53, were performed over a period of two days in July of 2019.

At Site 1, both unbound aggregate layers were placed and compacted in a single lift. Figure 4.2 shows pictures of the construction process: initial unloading of the aggregate in piles (Figure 4.2a), spreading and leveling of the aggregate with a CAT D5K Dozer (Figure 4.2b) and compaction with the CAT CS56B compactor (Figure 4.2c). Compaction of the IN #53 layer included three vibratory passes followed by one additional static pass, whereas the IN #8 layer was compacted only with static passes. No measurements of the thickness of the two aggregate layers were performed.

The northbound turning lane of US 231 (Figure 4.1) hosted the 30 ft by 9 ft testing section (Figure 4.3a). Tests were performed at 44 locations on a grid with 3 ft spacing in both directions. To draw the grid, a plastic mesh was positioned on the aggregate layer, and spray chalk was used to mark the testing locations (Figure 4.3b).

Figure 4.3c shows a schematic of the testing grid and summarizes the tests conducted at each location on the bottom #53 layer following compaction. They included: APT, LWD and sand cone tests, performed in that order. Sand cone tests were performed at only four locations. LWD tests were performed using the Zorn ZFG 3.0 light weight deflectometer (www.zorn-instruments.com) with both a small (LWD_S : $D = 0.150$ m) and a large (LWD_L : $D = 0.300$ m) plate. The drop height was kept constant and equal to 0.720 m in all tests, independent of the plate size. APT tests were all performed using the apparatus manufactured by Ingios Geotechnics. Details on the underlying theory, the device's design and operation, and data interpretation are provided in Chapter 2.

The following approach was followed to perform the APT tests. A first measurement was attempted using orifice B. As a reminder (see Chapter 2) this orifice is intended for soils with permeability falling below approximately $<4,000$ ft/day ($1.4 \cdot 10^{-2}$ m/s)). If this measurement was successful, no additional APT tests were performed, and the APT apparatus was moved to the subsequent measuring location. If, however, the pressure generated with this setup was insufficient to



Figure 4.2 Construction stages at Site 1: (a) placement, (b) spreading and leveling, and (c) compaction of aggregate.

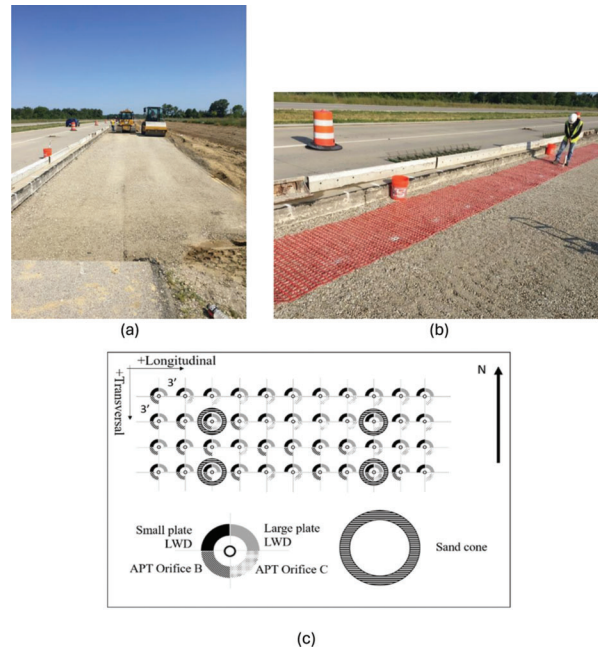


Figure 4.3 Testing at Site 1: (a) picture of working area, (b) mesh used to mark testing locations, and (c) testing grid and overview of testing program on compacted IN #53.

perform a measurement—an indication that the permeability exceeded the range measurable with that orifice—the test was repeated using orifice C. At a limited number of locations, APT measurements were performed with both orifices B and C.

While Figure 4.3c refers to the testing program on the IN #53 layer after compaction, additional LWD (large plate only) and APT tests were conducted prior to compaction at the same four locations where sand cone tests were performed. Use of the mesh shown in Figure 4.3b ensured exact correspondence of the testing locations both prior and post compaction. At three of these locations, additional sand cone tests were also performed prior to compaction. The results of all sand cone tests are summarized in Table 4.2. The data highlight the increase in dry density following compaction, from a mean of 1.76 g/cm^3 (109.8 pcf) to 1.96 g/cm^3 (122.3 pcf). Note that the corresponding relative compaction values shown in the table are based on a reference γ_{dmax} (140 pcf) derived from data for similar materials (Getchell et al., 2020), and, as a result, should be considered approximate. Values of the water content and the degree of saturation derived from the sand cone

tests show that the compacted aggregate was close to dry ($w < 1\%$, $S < 6\%$).

A more limited testing program was performed on the top IN #8 layer after compaction. Also, in this case prior to conducting the tests, the plastic mesh was used to create a grid and ensure overlap with the testing locations on the underlying layer.

Figure 4.4 provides a summary of the k data derived from the APT tests performed on the compacted IN #53 aggregate. As discussed earlier in this report, calculation of k from the APT results requires as input the material's degree of saturation. Given the very low values of the degree of saturation ($S < 6\%$) derived from the sand cone tests, no correction for saturation was applied to the Site 1 data. Per recommendation of the APT manufacturer the standard atmospheric pressure (101.325 kPa) was used as input in the expression used to derive k .

Figure 4.4a shows which orifices were utilized when testing each location. The type of orifice is a qualitative indicator of the material's permeability, as locations which required orifice C necessarily reflect higher values of k . Locations where measurements were not

TABLE 4.2
Results of sand cone tests at Site 1

	Transverse Position (ft)	Longitudinal Position (ft)	ρ_d (g/cm ³)	γ_d (kN/m ³)	γ_d (pcf)	w (%)	S (%)	RC (%) ¹
Before Compaction	3	6	1.65	16.2	103.0	0.8	3.2	73
	9	6	1.84	18.1	114.8	1.0	5.6	82
	9	24	1.79	17.6	111.7	0.9	4.6	80
Mean	–	–	1.76	17.3	109.8	0.9	4.5	78.1
After Compaction	3	6	2.05	20.1	127.9	0.4	3.0	91
	9	6	1.84	18.1	114.8	0.7	3.8	82
	3	24	1.91	18.7	119.2	0.5	3.3	85
	9	24	2.03	19.9	126.7	0.2	1.4	90
Mean	–	–	1.96	19.2	122.3	0.4	2.9	87.1

¹Based on γ_{dmax} = 140 pcf from (Getchell et al., 2020).

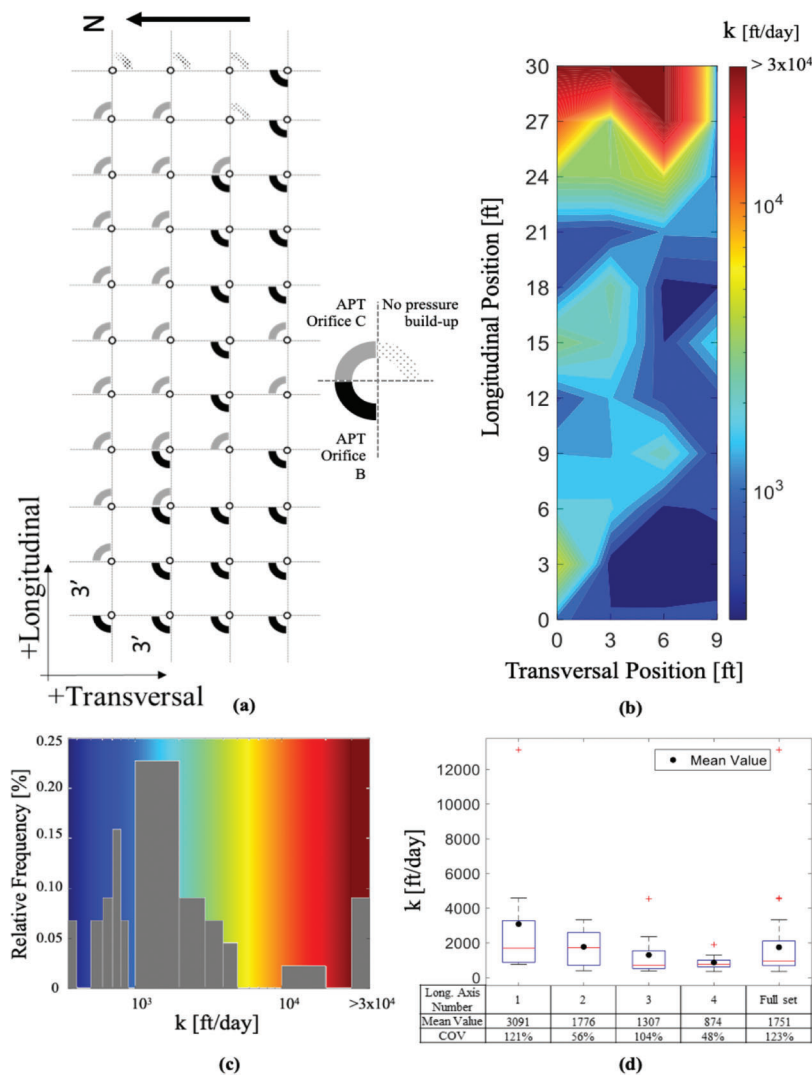


Figure 4.4 APT orifice B results from tests on IN #53 aggregate at Site 1: (a) tests performed, (b) spatial variation, (c) histogram, and (d) descriptive statistics.

possible, due to insufficient pressure build-up with both orifices, are also highlighted in the figure. At these locations, the permeability is expected to exceed the range measurable with the APT ($k > 20,000$ ft/day ($7.1 \cdot 10^{-2}$ m/s)). Figure 4.4b shows a map with contours of k for the compacted IN #53 layer. For purposes of creating the plot, a value of k equal to 30,000 ft/day was used as input for locations where there was insufficient pressure build up with orifice C.

Overall, as illustrated in the histogram shown in Figure 4.4c, the measured k data fall within a broad range, from a minimum of ~ 350 ft/day to a maximum of over 13,000 ft/day, with mean equal to 1,751 ft/day and CV = 123%. All values exceed the 350 ft/day threshold recommended for free draining subbases, falling instead within the range typical of permeable subbases (ACPA, 2007). Box plots for data collected along each of the four longitudinal axes, as well as for the full data set are presented in Figure 4.4d, highlighting how the higher values of k were clustered along the left side of the lane, in correspondence to what was originally the right shoulder of the northbound lane of US 231. Note that the mean and CV values are based only on measured data, i.e., they do not include the values assumed at locations where there was no pressure build up with either orifice. This implies that both mean, and CV are underestimates of the actual values.

At stated above, at four locations APTs were conducted after grading of the IN #53 aggregate, but prior to compaction. Three of these measurements required using orifice C. The results of these tests are summarized in Table 4.3. Comparison to the values of k derived from the APTs performed at the same locations after compaction show, as might be expected, a reduction in k (by a factor of 1.4–2.3). At the same time, at the fourth location a small increase in k was measured after compaction. Moreover, all k data obtained before compaction fall within the range established by the tests on the compacted aggregate. Overall, this suggests that additional factors other than density may affect k .

Plots similar to those used to present the k data are used in Figure 4.5 and Figure 4.6 to summarize the LWD results for the tests performed on the compacted IN #53 aggregate using the large and the small plate,

respectively. In each figure, panel (a) shows the spatial distribution of the LWD deflections, while the corresponding histogram is presented in panel (b). Finally, descriptive statistics of the data along each longitudinal axis are summarized in panel (c).

Both Figure 4.5 and Figure 4.6 show that higher deflections were measured at locations closest to the left shoulder of the turning lane, similar to what is observed for the k data derived from the APT (Figure 4.4). Focusing on the results of tests performed with the larger plate, all but one of the measurements points fall above the 0.27 mm threshold value used in INDOT specifications, with 50% of the measured deflections falling above 0.63 mm.

Despite the larger stress applied with the smaller plate, deflections of similar magnitude were measured using the small plate. Also, in this case the vast majority (93%) of the measurements exceed 0.27 mm. Moreover, both sets of data show similar trends across the testing strip (Figure 4.5b and Figure 4.6b), including similar values of the mean and the coefficient of variation for the full data set as well as for each of the longitudinal axes (Figure 4.5c and Figure 4.6c).

A limited number of LWD measurements (small plate only) were performed on the uncompacted IN #53 aggregate. The measured deflections are found to be higher (by 8% to 66%) than those measured at the same locations after compaction (Table 4.3).

Clear differences in the appearance of the IN #53 compacted aggregate surface across the testing strip were observed at Site 1. These differences were documented via pictures, as described in the previous chapter for the SBRITE site. Values of the MFS derived at each testing location by processing the images using the image analysis routine specifically developed for this purpose (Garzon-Sabogal et al., 2024) are shown in Figure 4.7a. These same data are presented in the form of a histogram in Figure 4.7b. For reference, Figure 4.7c shows images corresponding to locations where the minimum, median and maximum values of the MFS were recorded at the site. The histogram indicates a bimodal distribution of the MFS data around values of ~ 4.25 – 4.5 mm and 6 – 6.25 mm. From Figure 4.7a, the higher values of MFS, which

TABLE 4.3
Comparison of #53 APT and LWD data before and after compaction

	Transverse Position (ft)	Longitudinal Position (ft)	ρ_d (g/cm ³)	k (ft/day) ¹	LWD _S (mm)	RC (%)
Before Compaction	3	6	1.65	4,326 (B)	0.722	73
After Compaction	3	6	2.05	1,891 (B)	0.433	91
Before Compaction	9	6	1.84	1,264 (C)	0.394	82
After Compaction	9	6	1.84	729 (B)	0.365	82
Before Compaction	3	24	N/A	4,782 (C)	0.694	N/A
After Compaction	3	24	1.91	3,340 (B)	0.596	85
Before Compaction	9	24	1.79	766 (C)	1.906	80
After Compaction	9	24	2.03	1,070 (B)	1.304	90

¹(B) and (C) denote the orifice used for measurement.

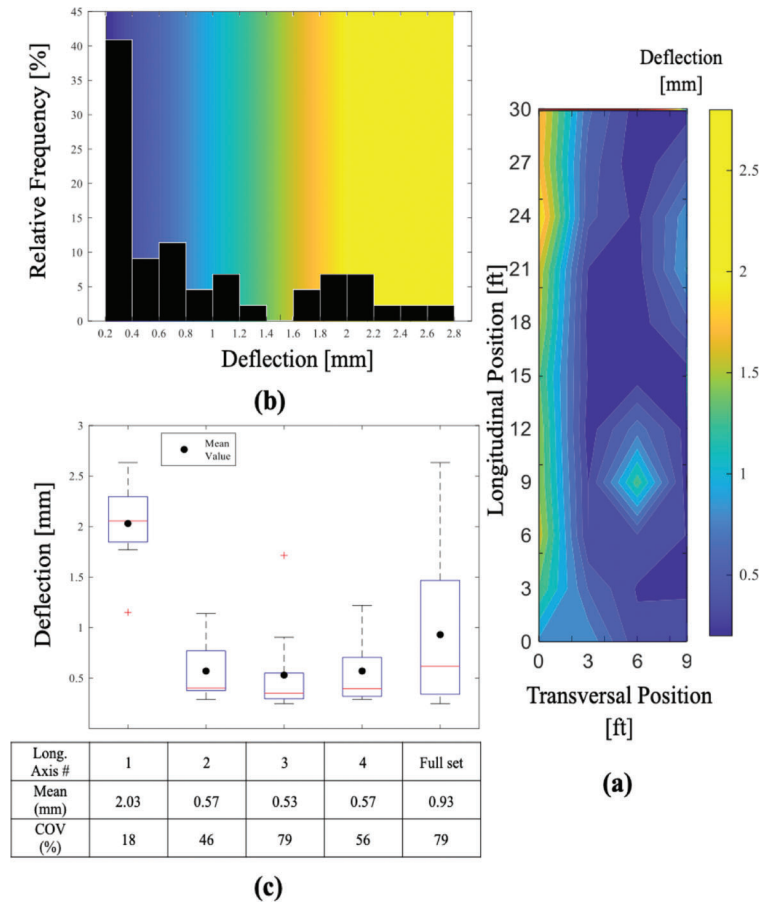


Figure 4.5 (a) Spatial distribution, (b) histogram, and (c) descriptive statistics of LWD_L deflection data collected on IN #53 at Site 1.

reflect the coarser aggregate, are found to correspond to testing locations along the left shoulder of the lane, consistent with the higher k values derived from the APT at these same locations. Moreover, the two overall highest values of MFS (8.2 and 7.2 mm) correspond to two of the locations where there was no pressure build up with either orifice, where k is assumed to exceed 20,000 ft/day. The relationship between k and MFS is discussed further in the following sections.

As summarized in Table 4.1 and Figure 4.3, 19 APT tests were performed using orifice C on the layer of compacted IN #8. k values derived for 11 of these tests (Figure 4.8a) fall between $\sim 2,700$ and 13,500 ft/day, with mean value of $\sim 8,400$ ft/day and CV = 44%. No measurements could be obtained for the remaining eight tests due to insufficient pressure build up, reflecting values of permeability more than 20,000 ft/day. These results demonstrate that the APT device, in its current configuration, cannot be used to consistently measure the hydraulic conductivity of aggregates as coarse as IN #8. As a result, subsequent testing at Sites 2 and 3, as well as at the SBRITE site focused exclusively on the subbase layer constructed using IN #53 aggregate.

LWD tests with both the small (150-mm diameter) and large (300-mm diameter) plate were also performed

on the IN #8 layer. The results of these tests are summarized in Figure 4.8b–c. The measured deflections fall in a broad range (e.g., 0.25 to 2.03 mm for the small plate), with the small plate LWD yielding deflections on average 25% higher than those measured with the larger plate. As seen for the tests performed on the underlying layer of IN #53, higher deflections were measured at locations along the first longitudinal axis.

As shown in Figure 4.9, a strong correlation, reflected in a coefficient of correlation greater than 0.94, is found to exist between the deflections measured using the large plate (LWD_L) on the IN #8 and the IN #53 layers. A similar correlation is found between the LWD_S deflections. This indicates that LWD measurements performed on the IN #8 layer are, in this case, largely controlled by the deformation of the underlying IN #53 layer, precluding inferences on the state of compaction of IN #8 from the LWD data.

4.3 Site 2: SR 46, Bloomington, IN

The second field testing program took place in the north-east limits of Bloomington, Indiana (Figure 4.10) on September 24, 2019. The project involved the reconstruction of the pavement of SR 46 around the

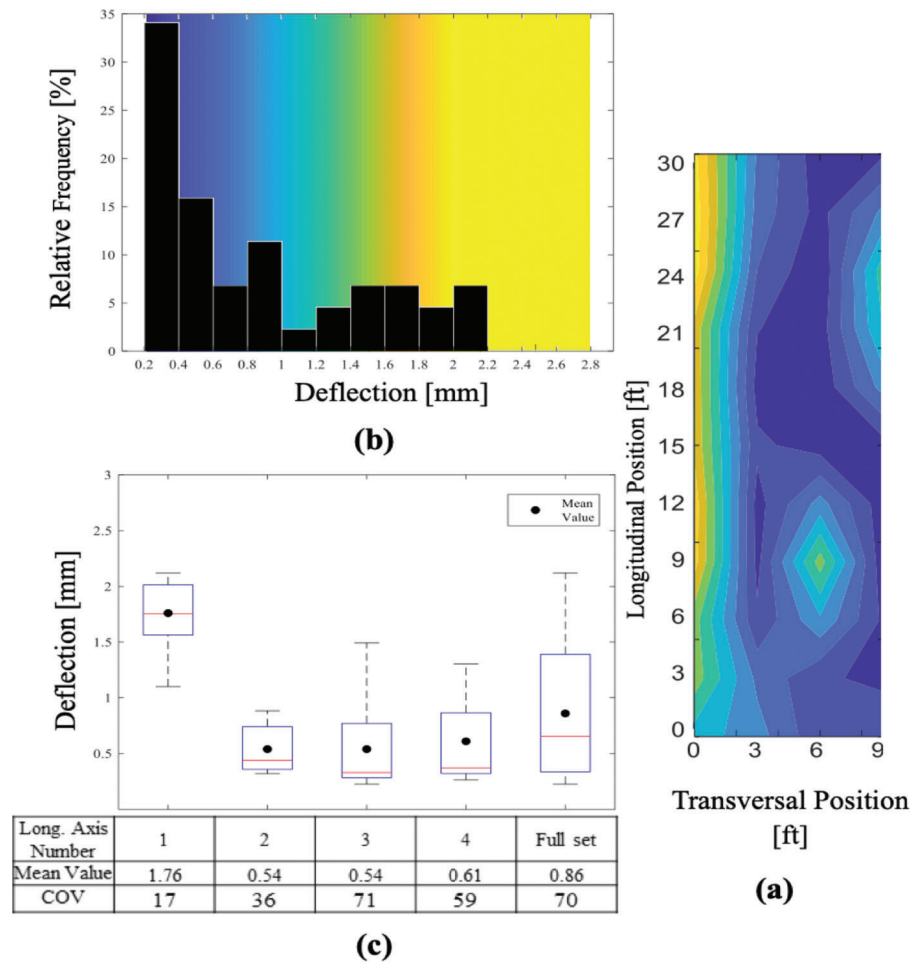


Figure 4.6 (a) Spatial distribution, (b) histogram, and (c) descriptive statistics of LWD_S deflection data collected on IN #53 at Site 1.

intersection with I-69. The pavement structure constructed at this site includes a 6-in. layer of IN #53 compacted over a geotextile covering the cement-treated subgrade. A 3-in. layer of IN #8 placed over this layer supports the concrete slab.

Testing at this site focused exclusively on the layer of IN #53. The aggregate was transported to the site in Kenworth T880 dump trucks with a capacity of up to 11.5 m³ (Figure 4.11). In constructing each lift, the aggregate was spread without the use of a spreader box and leveled using a CAT 140M2 motor grader (Figure 4.11b), targeting a thickness of about 1.5 in., very close to the maximum particle size of the aggregate. Finally, a vibrating compactor roller (Ingersoll-Rand SD-100D) was used to compact the lift. This process was repeated until the design thickness was achieved after compaction of the last lift.

Testing on the IN #53 layer took place over a 54 ft by 9 ft section, located over the east bound portion of SR 46 before the bridge crossing I-69. Similar to Site 1, prior to testing, the mesh shown in Figure 4.12a was positioned on the aggregate surface, and chalk paint was used to mark testing locations on a grid with 3 ft spacing in both directions. Figure 4.12b summarizes the

measurements conducted at each location. Only four sand cone tests were performed, all after compaction of the IN #53 aggregate.

LWD tests were performed at all locations using the same Zorn ZFG 3.0 light weight deflectometer employed at Site 1 with both a small (LWD_S : $D = 0.150$ m) and a large (LWD_L : $D = 0.300$ m) plate. As at Site 1, the drop height was kept constant and equal to 0.720 m in all tests, independent of the plate size.

APT tests were performed with the same apparatus used at Site 1 (see Chapter 2 for details on the design of the apparatus, its operation and data interpretation). Measurements could be performed at all but one testing location using orifice B. At approximately 60% of the testing locations, they were then repeated using orifice C (Figure 4.13a). These additional tests were performed to verify orifice calibrations and investigate any impact of the orifice size on the measurements.

The results of the four sand cone tests are summarized in Table 4.4. As for Site 1, no tests were performed to determine the maximum dry density of the specific IN #53 aggregate used at Site 2. Also in this case, relative compaction values are based on a reference γ_{dmax} for similar materials from (Getchell et al., 2020)

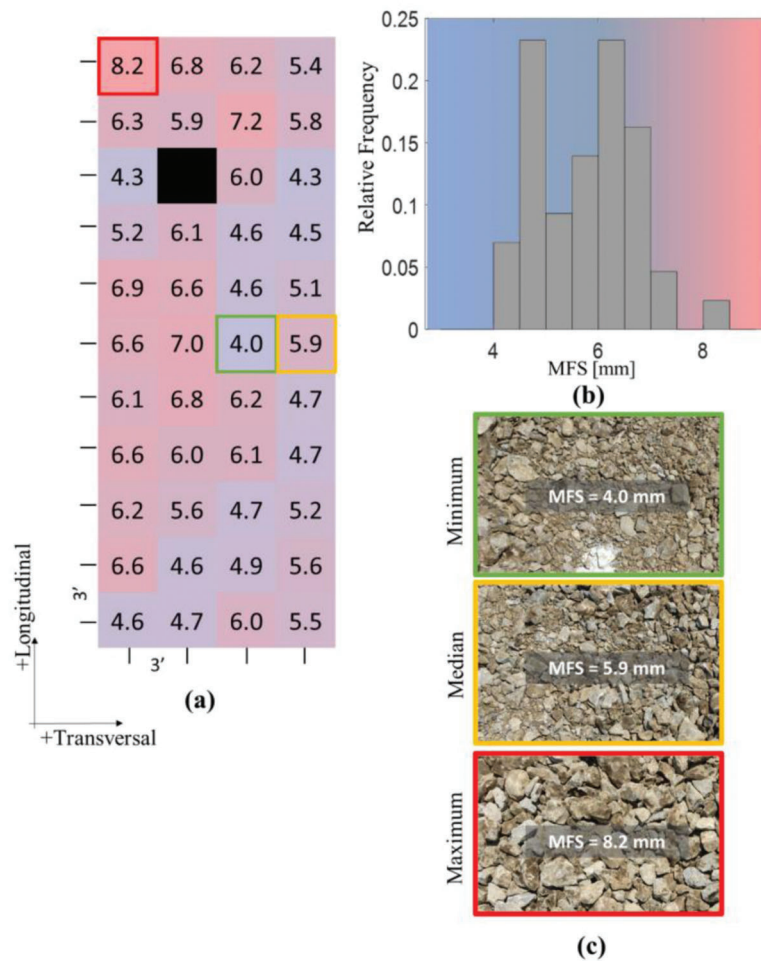


Figure 4.7 MFS data for Site 1: (a) spatial distribution, (b) histogram, and (c) images corresponding to minimum, median, and maximum values (size of images ~31 cm × 20 cm).

and thus should be considered approximate. The sand cone results reveal a well compacted layer, with relative compaction in the 91%–96% range.

Figure 4.13a shows the spatial distribution of the k data obtained from the APT tests on the layer of compacted IN #53. With one exception, all the data come from measurements performed using orifice B. Only in one case (transversal position = 3 ft, longitudinal position = 48 ft) it was necessary to use the larger orifice. As the values of the degree of saturation derived from the sand cone tests were relatively low (13%–23%), the data shown in the figure do not reflect any correction for S . This issue is further discussed below. Additionally, as for Site 1, per recommendation of the APT manufacturer the standard atmospheric pressure (101.325 kPa) was used as input in the expression used to derive k .

As reflected in the descriptive statistics summarized in Figure 4.13d, higher values of k were measured along the axis closer to the right shoulder. Across the testing section, values of k all exceeded 300 ft/day, with values lower than 1,000 ft/day measured at over 80% of the testing locations.

As indicated in Figure 4.12, at 44 out of the 76 testing location, APT measurements were made using both orifices. Figure 4.14 compares k values derived from these two measurements. Two sets of data from the tests performed with orifice C are included in the figure: the first was obtained using the calibration factor for orifice C provided by the APT manufacturer; the second using the results of the in-lab calibration performed by the research team. Values of k in the first set of data exceed those derived from the measurements using orifice B by a factor of ~2.7. Similar observations were made based on a more limited number of tests at Site 1. The second set of data, instead, provides results consistent with those obtained with orifice B. This demonstrates that with appropriate calibration, the results are independent of the orifice. This also stresses the importance of verifying factory orifice calibration factors.

The k values presented in both Figure 4.13 and Figure 4.14 were calculated assuming dry conditions ($S = 0$). Table 4.5 shows the impact of accounting for the measured degree of saturation in the reduction of the APT data. The effect is illustrated for the four

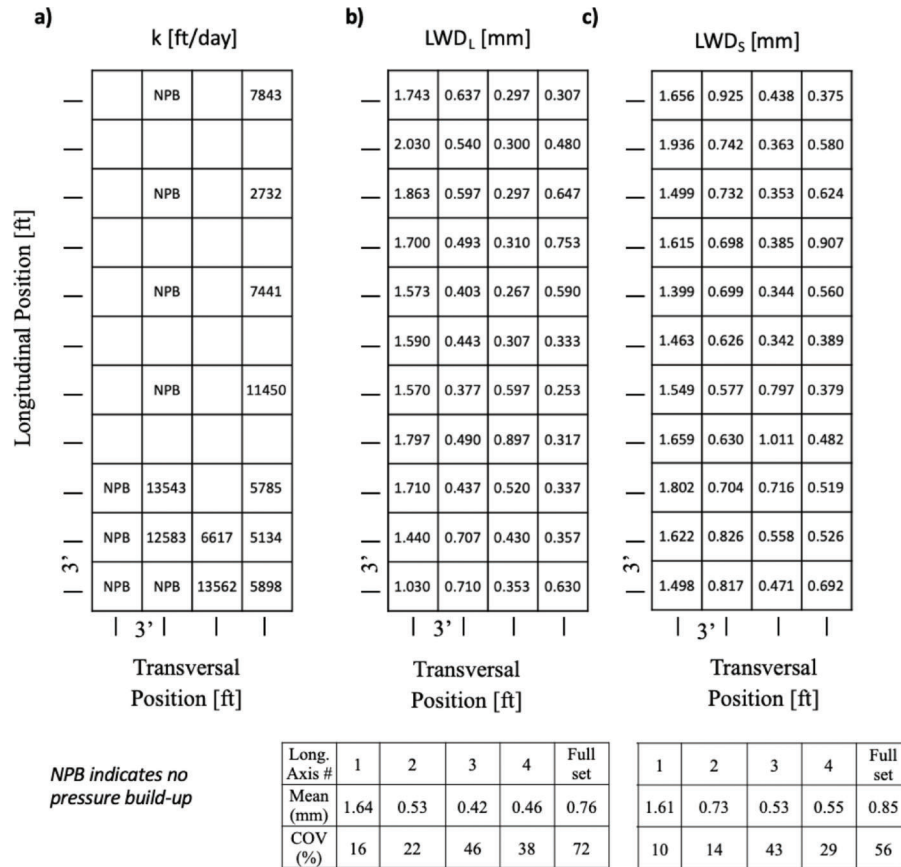


Figure 4.8 (a) APT, (b) LWD_L , and (c) LWD_S data from tests on IN #8 aggregate layer at Site 1.

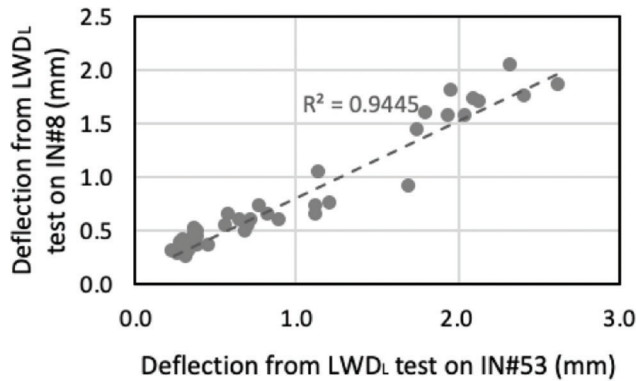


Figure 4.9 Correlation between deflections derived from LWD_L tests performed on IN #8 layer and on the underlying IN #53 layer at Site 1.

testing locations closer to where the sand cone tests were performed. As discussed in Chapters 2 and 3, based on White et al. (2007), the correction for the degree of saturation requires estimates of the residual saturation (S_r) and the Brooks-Corey pore size distribution index (λ) for the tested aggregate. In implementing the correction for the degree of saturation two sets of values were used for these parameters. The first ($S_r = 0$ and $\lambda = 3$) is based on recommendations provided by the APT manufacturer; the second ($S_r = 10\%$ and $\lambda = 1$) was selected by the research team

based on values reported in the literature for similar geomaterials (Gupta et al., 2004). As illustrated in the table, the impact of the correction increases with the degree of saturation and is also a marked function of the assumed values of S_r and λ . For the location with the highest degree of saturation (21%), the increase in k due to the correction is as high as 70%.

Results for the LWD tests conducted using the large and small plate are shown in Figure 4.15 and Figure 4.16, respectively. In general, tests using the smaller plate yielded slightly higher deflections (e.g., see shift to higher values in histograms and higher values of mean). In both cases, as reflected in the statistical descriptors shown in panels (c) of Figure 4.15 and Figure 4.16, the largest deflections were measured along the third vertical axis.

As in the case of Site 1, heterogeneity in the appearance of the aggregate surface was observed at Site 2. It was documented through pictures that were analyzed using the image analysis routine developed by Garzon-Sabogal et al. (2024). Values of the MFS derived from the analysis of the images collected at Site 2 are summarized in Figure 4.17, along with the corresponding histogram and reference pictures corresponding to the largest, smallest and median values of the MFS. While most of the MFS values fall between 4 and 4.5 mm, mean and CV are like the values determined for Site 1. As shown in Figure 4.17a, the surface was



Figure 4.10 Location of Site 2.



Figure 4.11 Construction stages at Site 2: (a) placement, and (b) spreading and leveling of aggregate.

observed to be generally coarser surface towards the right shoulder of the lane. The highest value of MFS (8.5 mm) is found to correspond to the location where the highest value of k was recorded ($\sim 3,365$ ft/day).

4.4 Site 3: I-65, Lebanon, IN

The third testing site, Site 3, is in Lebanon, Indiana (Figure 4.18). At this location, travel lanes were being added within the I-65 median between SR 32 and SR 47. As described for the other two sites, the project at Site 3 involved construction of a layer of IN #53 over the cement-treated subgrade to function as a separator layer. The layer was compacted by vibratory rolling (5 passes, followed by wetting of the surface and 2–3 additional passes) using a CAT CS-563E. Two different options were used for the overlying drainage layer over two segments of the projects: a cement treated permeable base and open graded asphalt. This was the first INDOT project on which these solutions for drainage layer were used.

Testing at Site 3 occurred in two phases. In the first, in July of 2021, tests were performed on the cement treated subgrade (July 20, 2021) and on the #53 aggregate (July 27, 2021) within a 500 ft section on the at the southern end of the added southbound lanes.

On October 5, 2021, the research team returned to the same site to perform tests on the cement treated base and the open graded asphalt drainage layers. The primary objective of these tests was to ascertain the applicability of the APT for measuring the permeability of these bound layers.

4.4.1 Tests on Cement-Treated Subgrade and Compacted IN #53 Subbase

Testing on the cement-treated subgrade and the compacted IN #53 subbase layer was concentrated in five rectangular areas (~ 9 ft by 12 ft) separated by approximately 100 ft, designated as Pads 1–5 (Figure 4.19a). On each pad, a testing grid with 3 ft spacing in both directions was established. The objective in

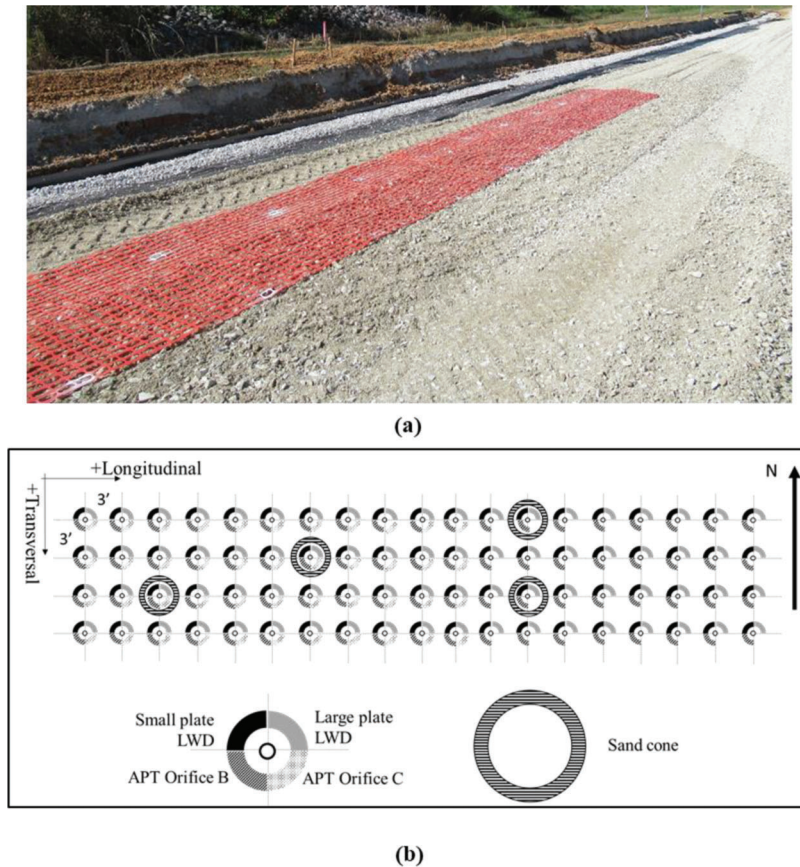


Figure 4.12 (a) Picture of working area, and (b) overview of testing program at Site 2.

conducting tests at multiple smaller pads rather than on a single strip as done at the previous sites was to cover a larger extension of the project and gain insight into the variability in the measured properties at two different scales.

As summarized in Table 4.1 and in Figure 4.19b–f, the testing program included LWD (large plate) on the subgrade, and nuclear density tests, DCPT, APT, LWD (small and large plate) on the IN #53 layer. Site 3 was the only construction site at which (a) LWD data were collected also on the cement-treated subgrade; and (b) nuclear density tests were performed on the compacted IN #53 aggregate to be able to accurately account for the in-situ degree of saturation when correcting the k data. These additions to the testing program were based on experience gained at the SBRITE site (Chapter 3). In designing the testing program, the plan was to conduct LWD tests at the same locations on both the subgrade and the overlying aggregate layers. Due to issues with accessing some areas of the construction site during the second visit, this was ultimately not possible for Pads 3–5 as shown in Figure 4.19d–f. DCPT tests were also performed at Site 3 as a means to obtain a measure of the thickness of the compacted aggregate layer. They were not successful in detecting the location of the interface between aggregate and cement-treated subgrade and are not further discussed.

As illustrated in Figure 4.19, nine nuclear density tests were performed on each pad. At each location, measurements were performed extending the probe of the Troxler 3430 Nuclear Density Gauge to both 4 and 6 in. Density values determined from the measurements performed with the probe at a 4" depth was found to be consistently larger than those with the probe pushed to a depth of 6". It was concluded that the latter data were affected by the lower density of the underlying subgrade. As a result, only the 4" measurements were used and are discussed herein.

Table 4.6 summarizes the mean values of dry density, dry unit weight, water content, degree of saturation and relative compaction for each of the five pads and for the entire site. Box plots of the dry density data are presented in Figure 4.20. Mean values of the relative compaction (as for the other sites calculated based on a $\gamma_{dmax} = 140$ pcf from Getchell et al. (2020) range between 77% (Pad 3) and 83% (Pad 1), lower than those determined at the other two sites. Mean values of the degree of saturation determined from the ND tests go from 24% (Pad 3) to 34% (Pad 5).

Figure 4.21 shows the spatial distribution of k over Pads 1 through 5, and the corresponding histograms. Table 4.7 summarizes mean, CV, and range for each of the pads, and for the entire site. Values of k presented in

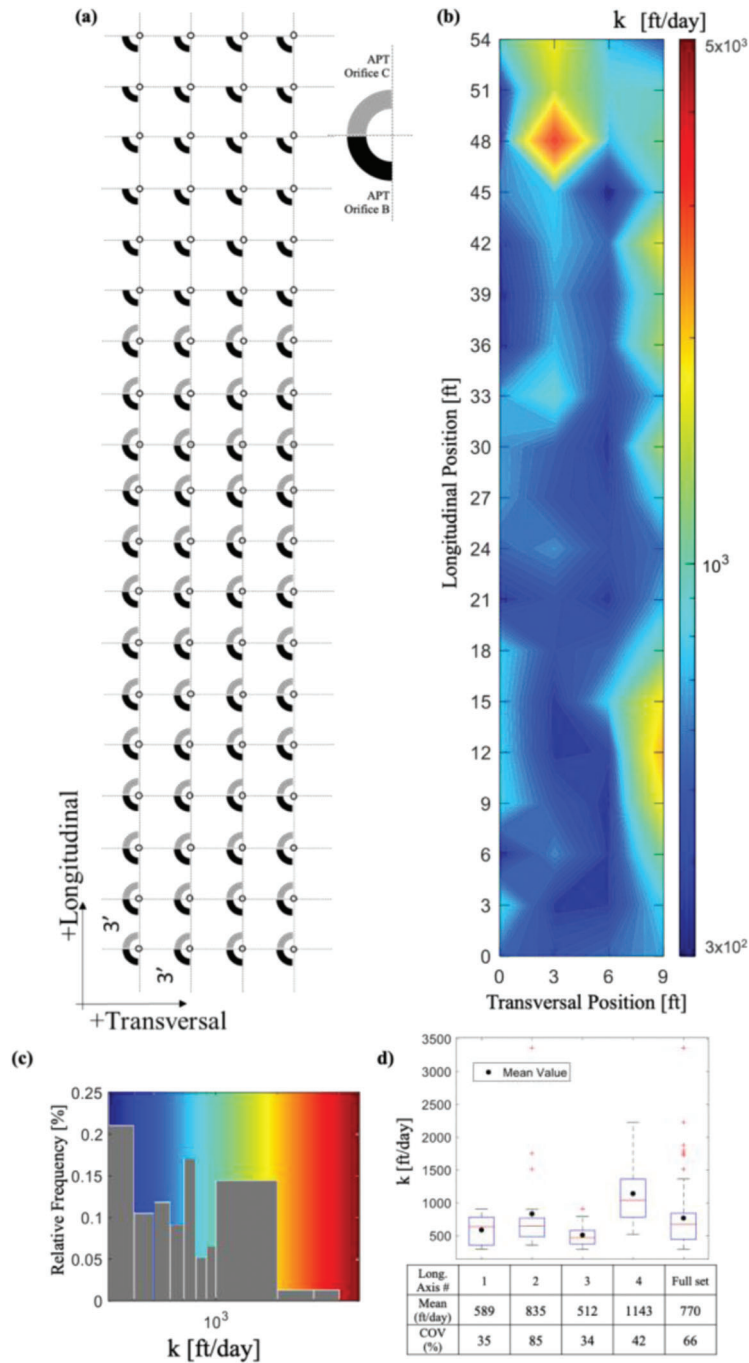


Figure 4.13 APT orifice B results from tests on IN #53 at Site 2: (a) tests performed, (b) spatial variation, (c) histogram, and (d) descriptive statistics of measurements.

TABLE 4.4
Results of sand cone tests at Site 2

Transverse Position (ft)	Longitudinal Position (ft)	ρ_d (g/cm ³)	γ_d (pcf)	γ_d (kN/m ³)	w (%)	S (%)	RC (%) ¹
3	18	2.12	132.1	20.8	1.4	12.8	94
6	6	2.12	132.2	20.8	2.3	21.0	94
0	36	2.06	128.3	20.2	1.6	13.1	91
6	36	2.15	134.2	21.1	1.6	14.9	96
Mean =		2.11	131.7	20.7	1.7	15.5	93.8

TABLE 4.5
Effect of degree of saturation on value of k derived from APT measurements at select locations at Site 2

Transverse Position (ft)	Longitudinal Position (ft)	k (ft/day) $w/S = 0$	S (%)	k (ft/day) $S_r = 0.1, \lambda = 1$	k (ft/day) $S_r = 0, \lambda = 3$
3	18	475	12.8	503 (+6%)	642 (+35%)
6	6	375	21.0	485 (+29%)	644 (+72%)
0	36	342	13.1	364 (+6%)	464 (+36%)
6	36	530	14.9	599 (+13%)	774 (+46%)

% relative to k w/S = 0

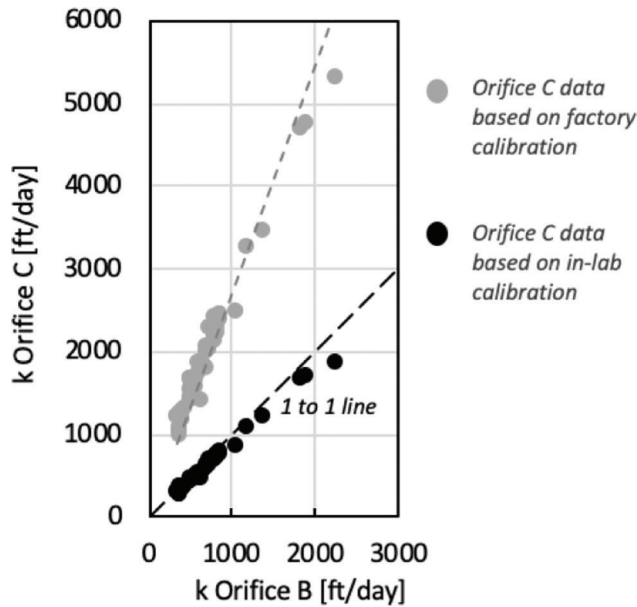


Figure 4.14 Impact of orifice C calibration on values of k derived from APT measurements.

Figure 4.21 were derived from APT measurements performed using the same apparatus used at the other sites (see Chapter 2 for details on equipment testing procedures and data reduction). The values of k reported in Figure 4.21 and Table 4.7 account for the aggregate's degree of saturation. Specifically, for each pad, the nine measurements obtained from the nuclear density tests were interpolated to obtain position specific values of S . Based on data available in the literature for similar materials, the residual degree of saturation (S_r) and the Brooks-Corey pore size distribution index (λ) were assumed to be equal to 10% and 1, respectively. Per recommendation of the APT manufacturer, the standard atmospheric pressure (101.325 kPa) was used as input in the expression used to derive k .

The vast majority of the measurements (90 out of 96) were performed using orifice B. Four of the measurements (1 on Pad 2 and 3 on Pad 3) required using orifice C, and two orifice A (both on Pad 5). Overall, the k

data collected across the site vary across almost two orders of magnitude (46 ft/day [Pad 1] to 3,082 ft/day [Pad 3]), with CV equal to 98%. Approximately 60% of the data fall below 500 ft/day. Significant variability in the k data is observed also in the single pads, with CV values ranging from 43% (Pad 5, at which only 12 APTs could be performed) to 95% (Pad 2). In several of the pads, the tests identify localized areas with k values significantly greater than the measurements obtained in immediate proximity (e.g., see green-to-red k values above 2,000 ft/day in Pads 2 and 3).

Plots and histograms of the deflections from the LWD tests performed using the Zorn ZFG 3.0 light weight deflectometer (www.zorn-instruments.com) on the cement treated subgrade (large plate [D = 0.30 m] only) and on the compacted IN #53 aggregate (large [D = 0.30 m] and small [D = 0.15 m] plate) are presented in Figure 4.22–Figure 4.24. Note that as done at the SBRITE site (Chapter 3), for the small plate only the drop height was reduced from 0.72 m to 0.17 m for consistency in the applied stress.

In general, the LWD_L data for the cement-treated subgrade (Figure 4.22) are relatively consistent across the five pads (overall CV = 28%) with mean values ranging between 0.25 mm (Pad 3) and 0.32 mm (Pad 1). Approximately 47% and 30% of all measurements fall above the 0.27 mm and 0.31 mm threshold values used in INDOT specifications.

The deflections from the LWD_L tests on the IN #53 aggregate (Figure 4.23) are, in general, significantly higher than those measured on the subgrade (89% and 77% of all measurements are greater than 0.27 mm and 0.31 mm, respectively). This is consistent with the low values of the maximum dry unit weight (107.3–116.1 pcf, corresponding to relative compaction less than 84%) derived from the nuclear density tests (Table 4.6 and Figure 4.26). Additionally, greater variability is observed from pad to pad, as illustrated by the mean values of the deflection data, which vary from 0.27 mm (Pad 1) to 0.73 (Pad 4). In each pad, the high density of the LWD_L testing program identifies localized areas with significantly higher deflections, where pavement damage and distress may be anticipated. This degree of local variability cannot be captured by traditional

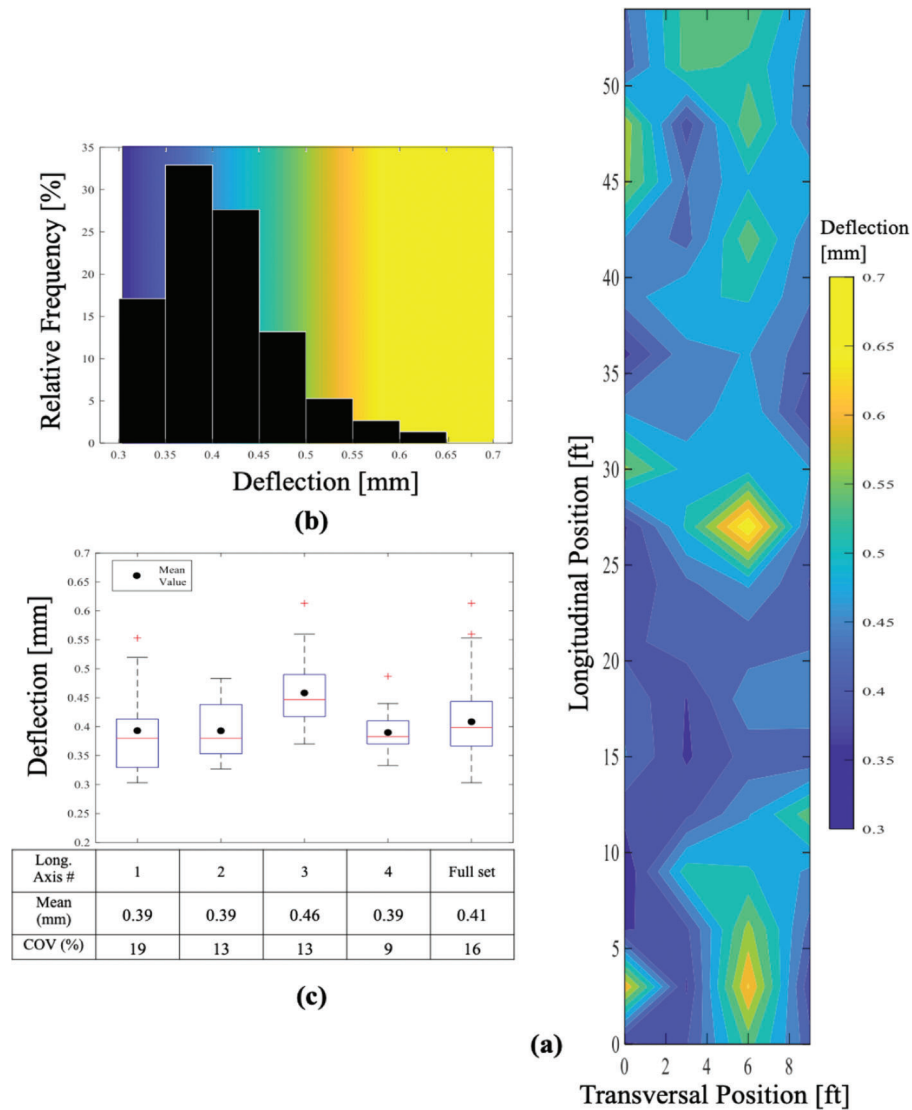


Figure 4.15 (a) Spatial distribution, (b) histogram, and (c) descriptive statistics of LWD_L deflection data collected on IN #53 at Site 2.

QA/QC approaches, which generally involve testing at locations offset by a few hundred meters (e.g., INDOT, 2020).

As shown in Figure 4.25a, no correlation is found to exist between the LWD_L deflection data measured on the compacted IN #53 aggregate and those measured on the underlying subgrade. This contrasts with what was observed at Site 1, where a strong correlation was found between the deflections measured on the aggregate layers (IN #8 overlying IN #53) tested (Figure 4.9). It is, however, consistent with the results for the cement-treated strip at the SBRITE site.

LWD_S tests were also performed on the IN #53 aggregate (Figure 4.24) at Site 3. Similar observations—generally large deflections and variability between pads—to those outlined above for the LWD_L tests apply in this case. As expected, the data for the two tests are found to be strongly correlated Figure 4.25b. On average, relative to the LWD_L deflections, those

measured with smaller plate are 15% smaller, consistent with the smaller depth of influence (as discussed above LWD_S tests at Site 3 were performed with reduced drop height to apply a stress like that applied with the large plate). Finally, Figure 4.27 summarizes the MFS data. Across all pads, values of the MFS are quite consistent (mean = 3.9 mm, CV = 14%). MFS mean values for the individual pads are in the 3.7 to 4.3 mm range). Values of the CV are relatively small (5%–19% for the individual pads) reflecting limited heterogeneity within each pad.

4.4.2 Tests on Cement-Treated Permeable Base and Open-Graded Asphalt

As discussed earlier, the second stage of testing at Site 3 comprised a program of APTs on two different bound drainage layers: a cement-treated permeable base (CTPB) and an open-graded asphalt (OGA) layer.

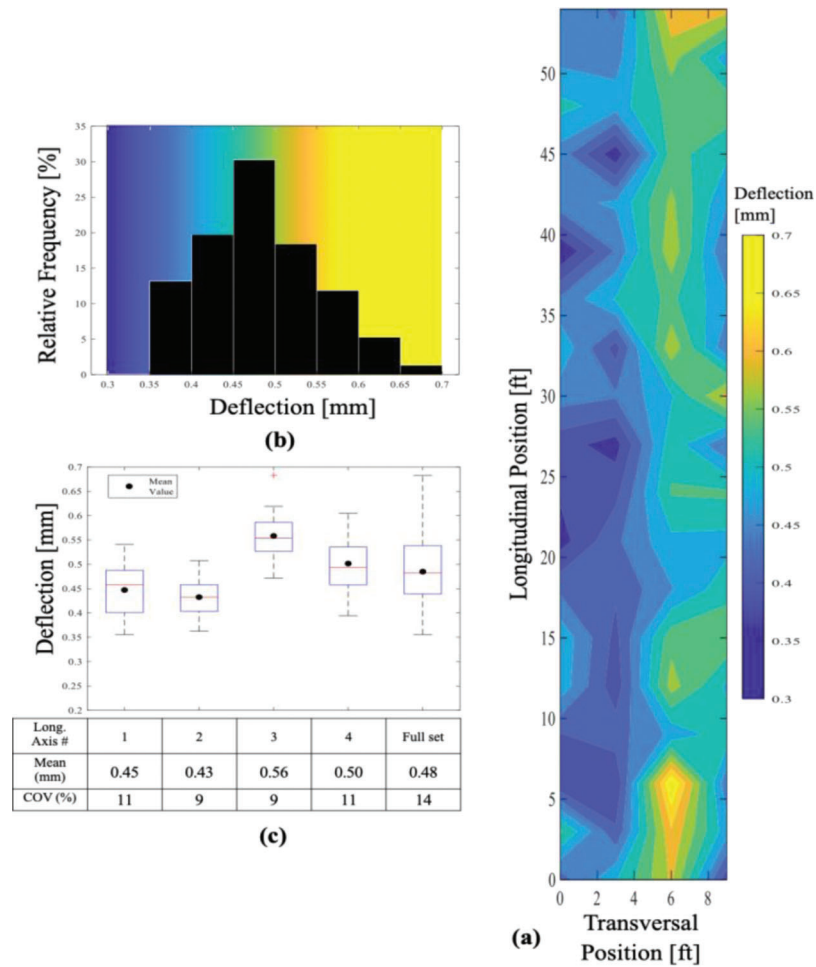


Figure 4.16 (a) Spatial distribution, (b) histogram, and (c) descriptive statistics of LWD_S deflection data collected on IN #53 at Site 2.

Figure 4.28a shows the proximity of the two drainage layers at the site. Tests were performed at 10 locations on the cement-treated permeable base, over an approximately 500-ft stretch, and at two locations offset by 40 ft on the contiguous OGA section. Figure 4.28b–f shows views of the surface of the two layers. The white striations visible on the CTPB surface are due to a curing sealant applied after construction of the layer.

At all locations, measurements were first performed at a reference point termed the “center.” At most locations additional tests were then performed at four additional points positioned 3 ft from the center point along two diameters orthogonal to each other (see Figure 4.29). The objective of these tests was to quantify variability in k at two different scales (“local” foot-level scale and larger 100-ft scale). At all locations repeat measurements were performed at the center point, both keeping the device stationary and lifting and repositioning it. Overall, approximately 100 and 30 measurements of k were obtained on the open graded asphalt and the cement-treated permeable base, respectively.

Figure 4.29 shows k data collected at all testing locations on both drainage layers. These data correspond to single measurements at each measuring point (i.e., no repeat measurements are included). Values of the mean, the CV and the range for each location and for the two complete datasets are summarized in Table 4.8. In the case of the cement-treated base, k varies significantly at each location (range = 69 to 1,757 ft/day and CV = 38%–87%) and across all measurements (range = 1,942 ft/day CV = 64%), indicating similar variability at the two scales examined. Similar observations apply to the open-graded asphalt layer. In general, for both layers, the values of k are of the same order of those measured on the compacted IN #53 aggregate. Most of the measurements (75% of those on the CTPB and 100% of those on the OGA) exceed 350 ft/day.

At both locations on the OGA layer and at six locations on the CTPB repeat measurements were performed at the center point, both keeping the device stationary, and lifting and repositioning it, carefully targeting the same testing point. The goal of these measurements was to quantify the repeatability in the k

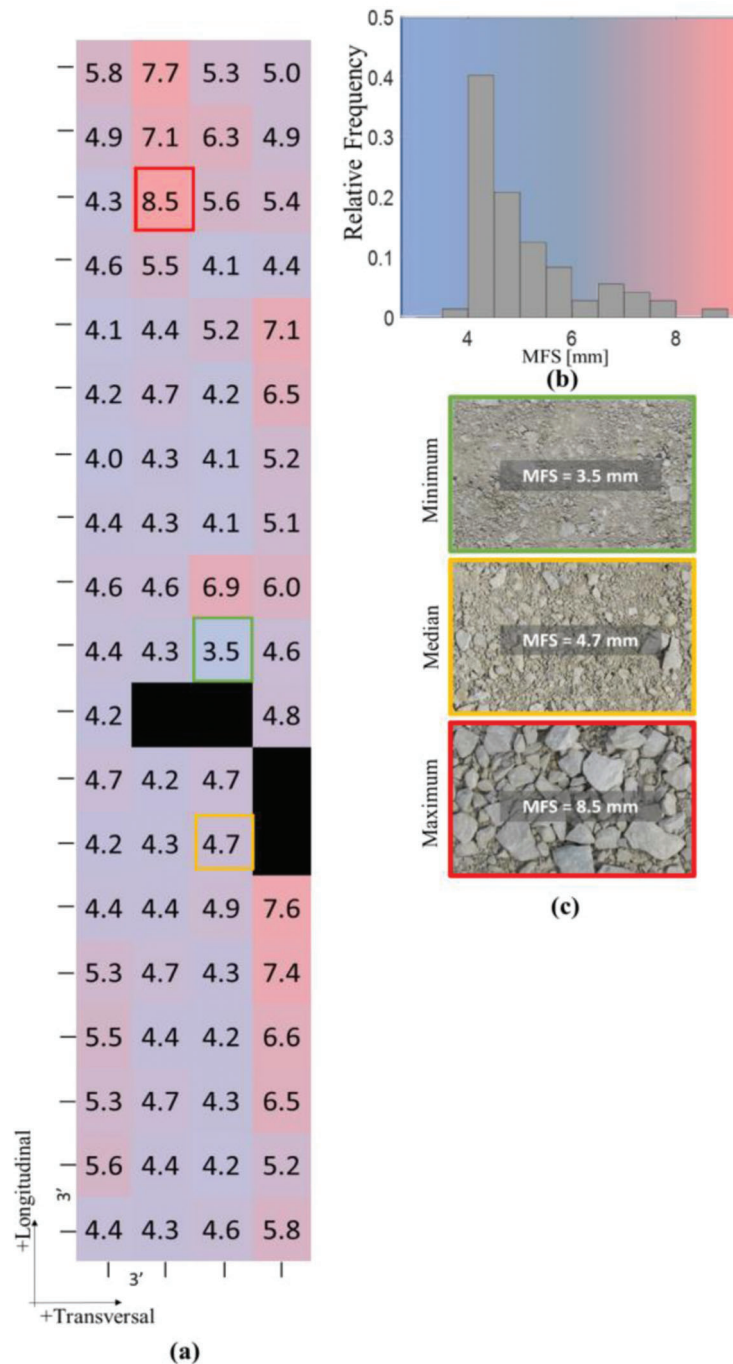


Figure 4.17 MFS data for Site 2: (a) spatial distribution, (b) histogram, and (c) images corresponding to minimum, median, and maximum values (size of images ~31 cm × 20 cm).

data produced by the APT method. Similar to the field experiments performed at the SBRITE site (see Section 3.4.5) and laboratory tests presented in Chapter 5, the first set of measurements, which were performed in rapid succession without modifying the testing conditions is intended to measure the inherent repeatability of the measurement. The second set of measurements reflects the impact of slight differences in the manner

the pad and the APT device are positioned. Representative example plots of repeat data collected at four locations are presented in Figure 4.30. Key statistical indicators derived from repeat measurements at all testing locations are summarized in Table 4.9.

Values of the CV derived from repeat measurements performed without moving the device vary across all testing locations between 1.2% and 3.0%. For all testing

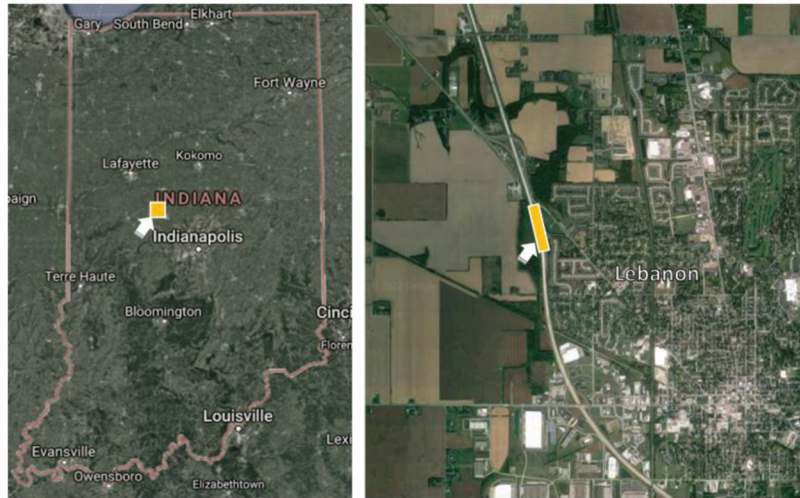


Figure 4.18 Location of Site 3.

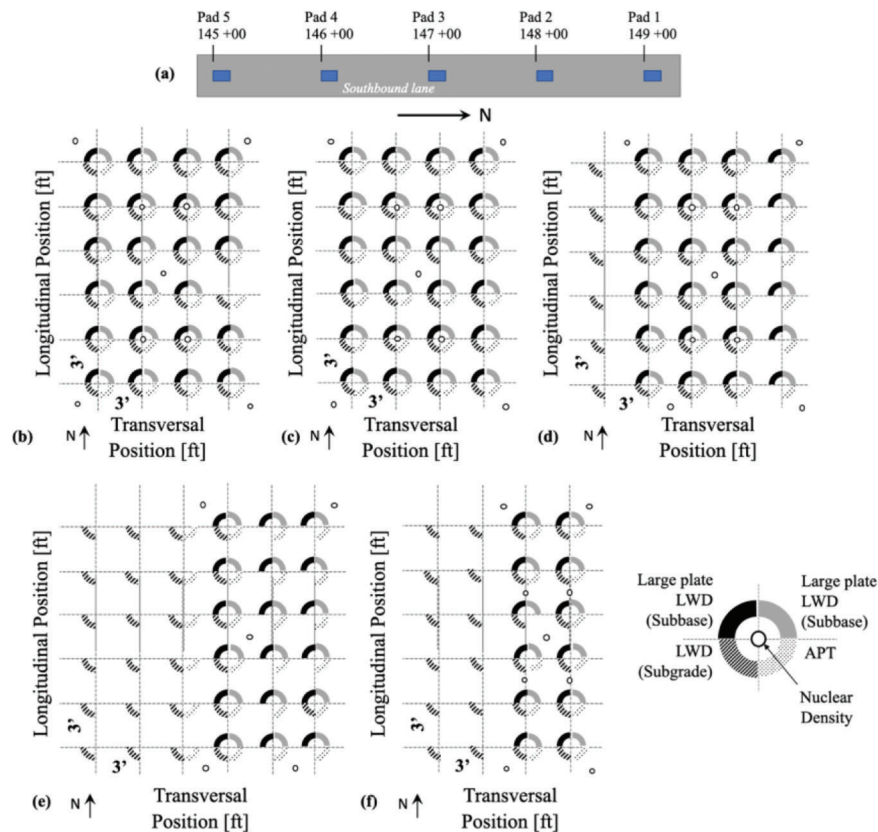


Figure 4.19 (a) Location of testing pads at Site 3 and testing program for (b) Pad 1, (c) Pad 2, (d) Pad 3, (e) Pad 4, and (f) Pad 5.

locations the values of CV increase for the second set of measurements but remain below $\sim 10\%$. As illustrated in Figure 4.30 and Table 4.9, differences between measurements performed targeting the same location on materials with the appearance as uniform as that of the two bound layers tested at Site 3 can exceed 200 ft/day. This highlights the challenges with implementing excessively stringent QA/QC criteria.

4.5 Observations on Compound Field Data and Comparisons Between Sites

A summary of the data from Sites 1–3 is presented in Table 4.10 and in the box plots in Figure 4.31. For reference, data from the two strips tested at the SBRITE site are also included. Panels (a–d) in the figure pertain to the properties of the compacted IN

TABLE 4.6

Result summary of nuclear density tests performed on Pads 1–5 at Site 3 (numbers represent mean values derived from nine tests performed on each pad)

Pad No.	ρ_d (g/cm ³)	γ_d (kN/m ³)	γ_d (pcf)	w (%)	S (%)	RC (%) ¹
1	1.86	18.2	116.1	5.5	31.3	83
2	1.84	18.1	114.8	4.7	26.0	82
3	1.72	16.9	107.3	5.4	23.9	77
4	1.81	17.8	112.9	5.0	25.7	81
5	1.74	17.1	108.6	7.1	33.7	78
All	1.79	17.6	111.7	5.5	28.1	80

¹Based on $\gamma_{dmax} = 140$ pcf from (Getchell et al., 2020).

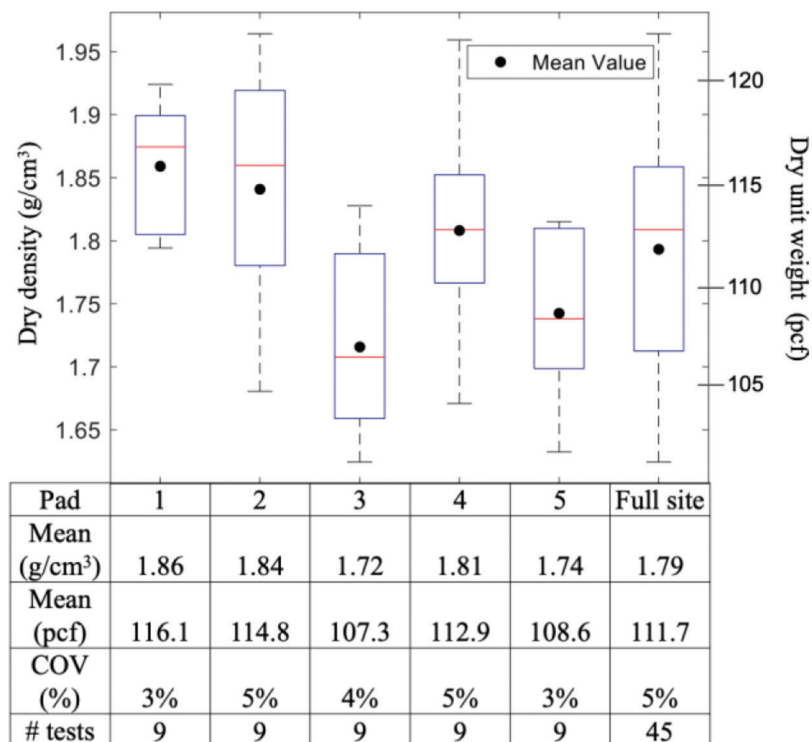


Figure 4.20 Nuclear density results for IN #53 at Site 3.

#53 aggregate layer, while panel (e) summarizes the available LWD_L data collected on the subgrade (Site 3 and SBRITE strips only). The graphs illustrate the broad range over which the properties of the compacted aggregate vary across all sites. Note that the k data reported in Figure 4.31a for the SBRITE strips and for Site 3, which represent the ends of the k range, are corrected to account for the in-situ degree of saturation, while the results for Sites 1–2 are not corrected as no data were available on the local variation of the degree of saturation. Additionally, the graphs do not reflect the high values ($>20,000$ ft/day) that apply to testing locations where there was no pressure buildup, as no specific value of k could be assigned to these locations. Independent of the site, of the aggregate properties examined, k values show the greatest dispersion, with CV ranging between 63% and 123%. At the other end,

the dry density shows the smallest variability (CV = 2%–5%), followed by MFS (CV = 14%–20%) and LWD_L (CV = 16%–79%).

Across Sites 1–3 the trend in the k data (Figure 4.31a) is the same as that of the MFS (Figure 4.31b) results. Site 1, where the higher values of k were measured, is also the site characterized by the higher values of MFS. Similarly, at Site 3, both k and MFS fall at the low end of the values measured across the three construction sites. This is true despite the much lower dry density achieved at Site 3 (Figure 4.31d), implying that particle size, as measured by the MFS, affects k to a greater degree than particle packing, as measured by the dry density. The data for the strips at the SBRITE site generally support this trend (the much higher density of the aggregate compacted on the cement-treated strip may affect the measurements on that strip).

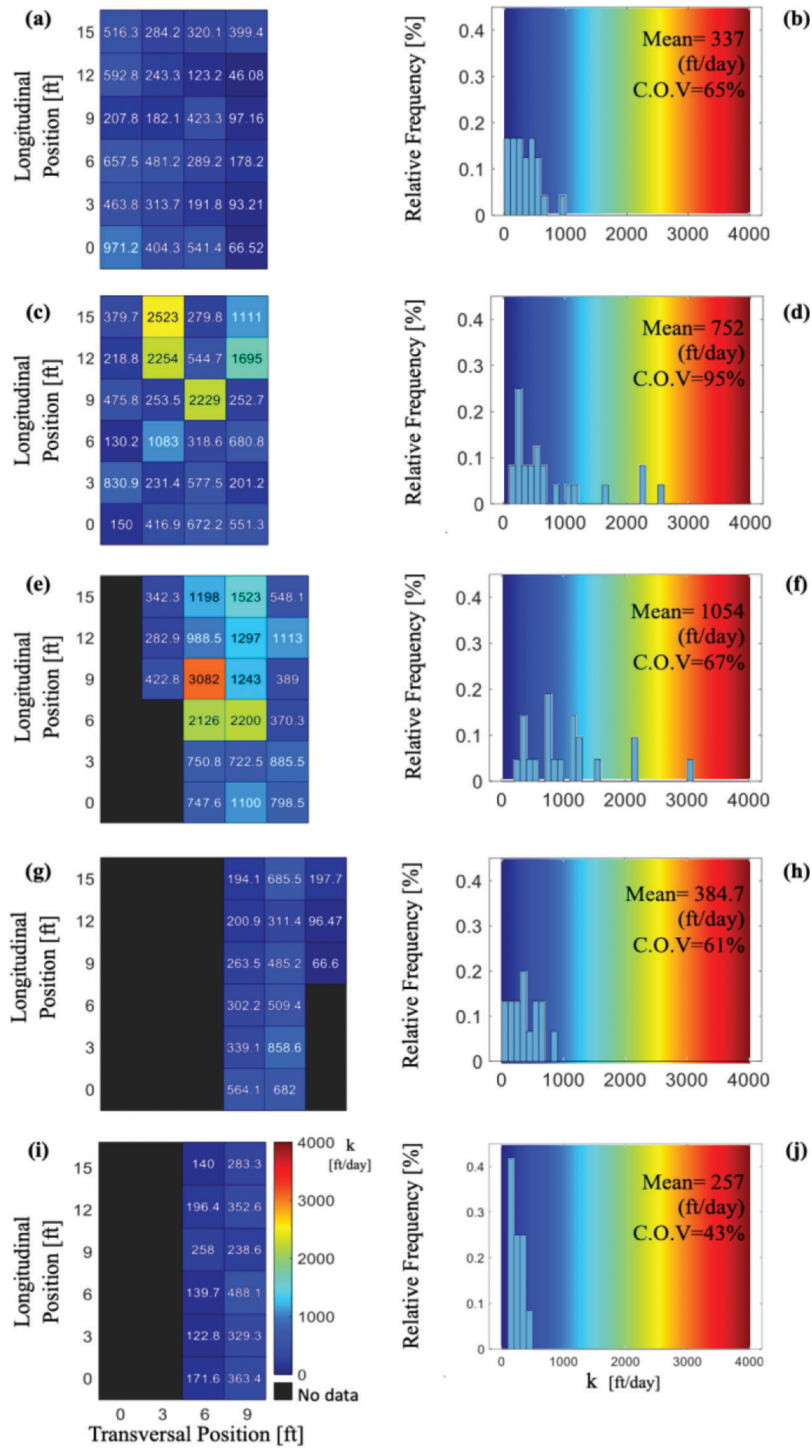


Figure 4.21 APT results for Site 3: spatial distribution and histograms for (a–b) Pad 1, (c–d) Pad 2, (e–f), Pad 3, (g–h), Pad 4, and (i–j) Pad 5.

As discussed in the previous chapter, variations in the MFS also explain the local variability in k across individual sites. This is illustrated in Figure 4.32, in which values of k of Sites 1 and 2 are plotted versus MFS alongside the data from the untreated strip at SBRITE already presented in Chapter 4. For the latter dataset, a strong correlation (as measured by a

correlation coefficient $r = 0.85$ and $p\text{-value} = 5 \times 10^{-5}$) was found to exist between MFS and $\log(k)$. Despite some scatter, a similar trend is observed in the data for Sites 1 and 2, supporting the notion that the MFS parameter is an indicator of local heterogeneities driving variability in hydraulic conductivity at the local scale.

TABLE 4.7
Key statistical indicators derived from APT measurements of the k of IN #53 at Site 3

Pad No.	Mean (ft/day)	CV (%)	Min–Max (ft/day)	Range (ft/day)	n
Pad 1	337.0	65.5	46–971	925	24
Pad 2	752.5	94.7	130–2,523	2,393	24
Pad 3	1,053.8	67.0	183–3,082	2,899	21
Pad 4	383.8	61.5	67–859	792	15
Pad 5	1,168.3	43.4	123–488	365	12
All	595.0	98.1	46–3,082	3,036	96

Examination of the dry density and LWD_L deflection data, both of which are used for QA/QC control of compacted aggregates offers interesting insights. To start, as observed for the SBRITE strips, no strong correlation between the dry density and LWD_L deflection was found for Site 3. Moreover, while the LWD_L deflections measured in the tests on the IN #53 aggregate are of the same order or smaller than those measured at the other sites, values of the dry density are significantly and consistently smaller.

Table 4.10 also shows that at all sites the dry density data are characterized by lesser variability (CV =

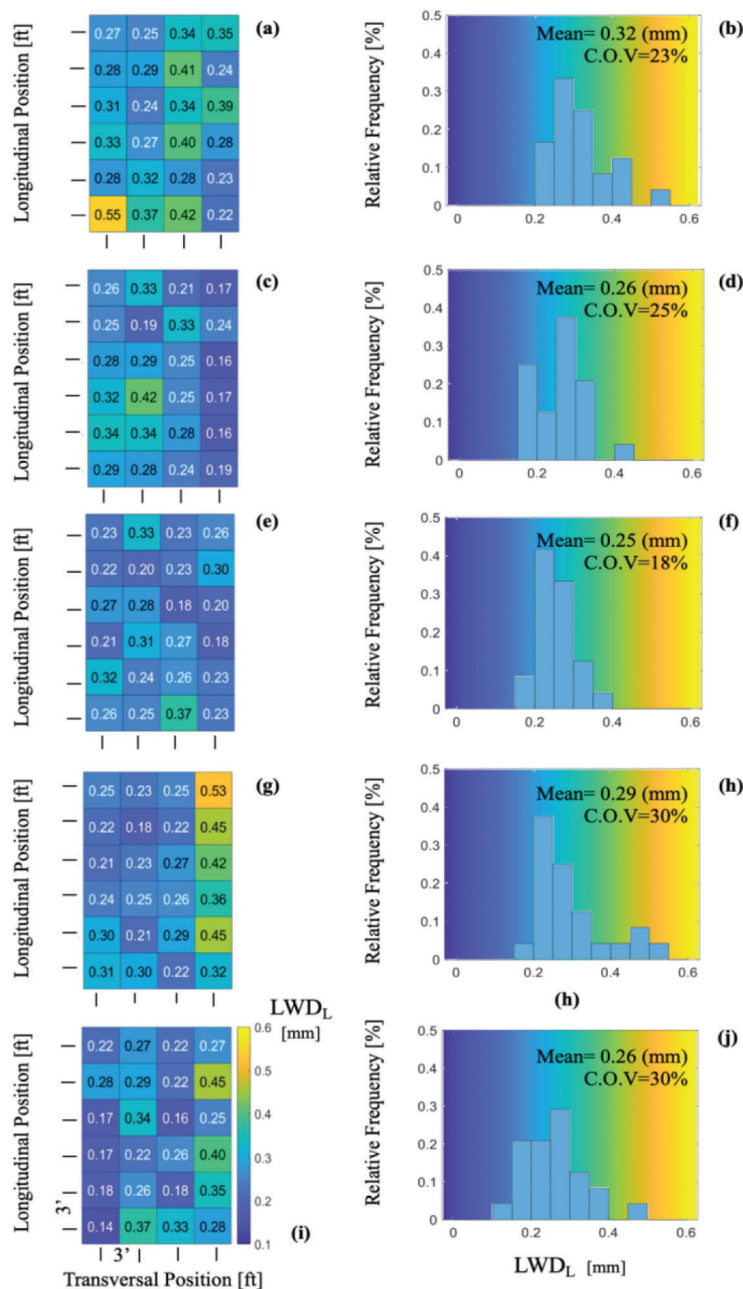


Figure 4.22 LWD_L results from tests on cement-treated subgrade at Site 3: spatial distribution and histograms for (a–b) Pad 1, (c–d) Pad 2, (e–f) Pad 3, (g–h) Pad 4, and (i–j) Pad 5.

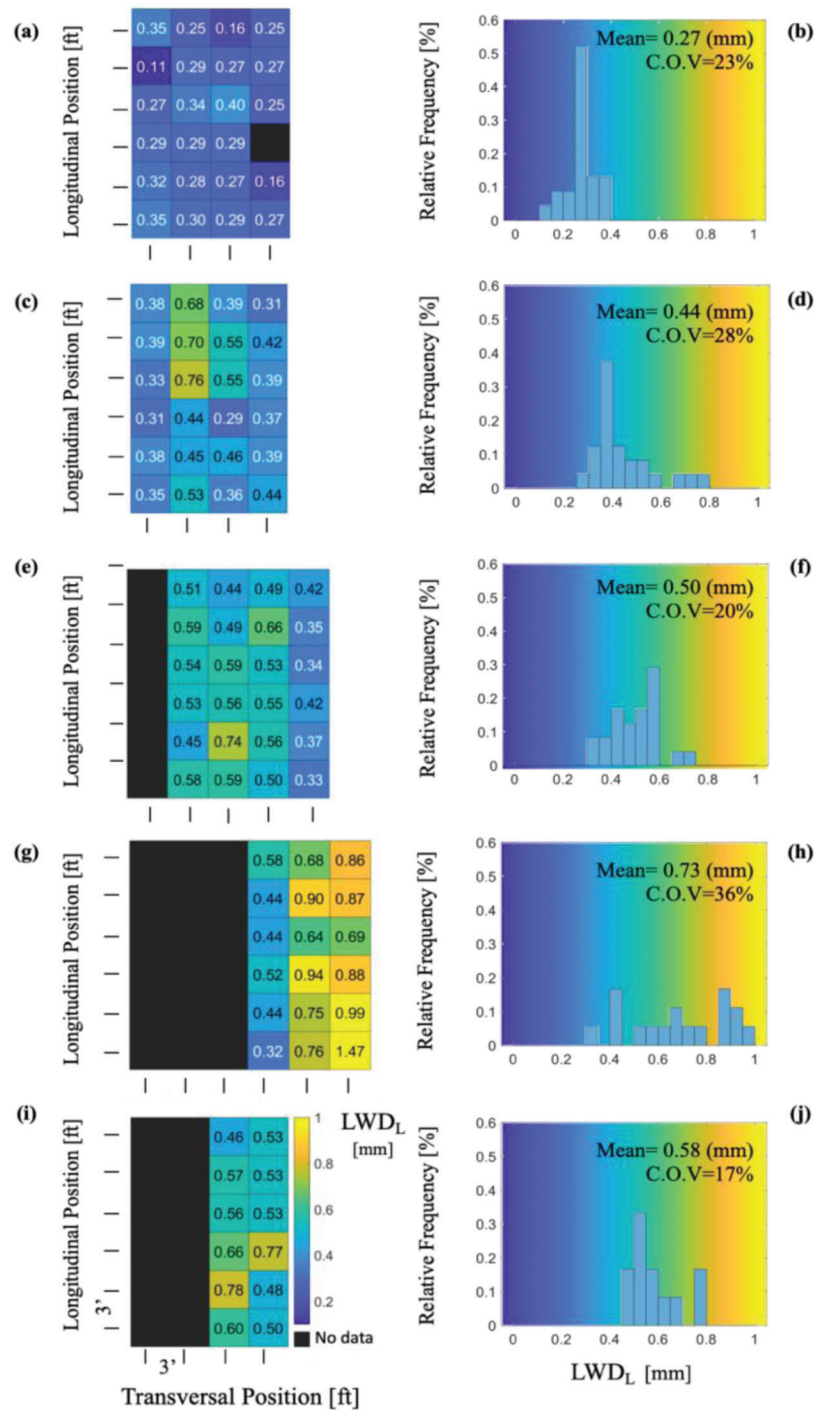


Figure 4.23 LWD_L results from tests on IN #53 at Site 3: spatial distribution and histograms for (a–b) Pad 1, (c–d) Pad 2, (e–f) Pad 3, (g–h) Pad 4, and (i–j) Pad 5.

2%–5%) compared to the LWD_L deflections (CV 16%–79%, Table 4.10). This suggests that factors other than the state of compaction affect the LWD_L results,

raising questions regarding the use of LWD tests for verification of the state of compaction of aggregate layers.

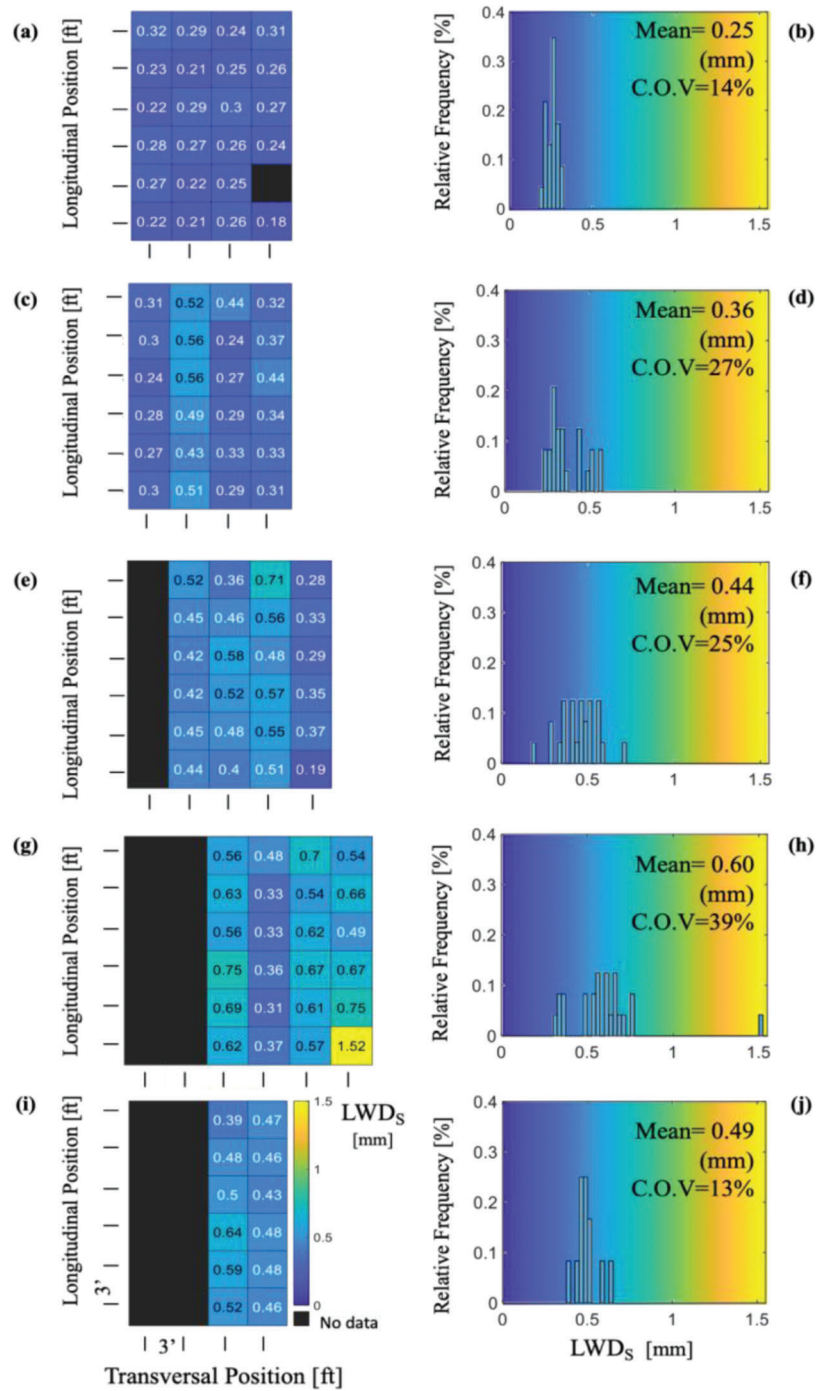


Figure 4.24 LWD_S results from tests on IN #53 at Site 3: spatial distribution and histograms for (a–b) Pad 1, (c–d) Pad 2, (e–f) Pad 3, (g–h) Pad 4, and (i–j) Pad 5.

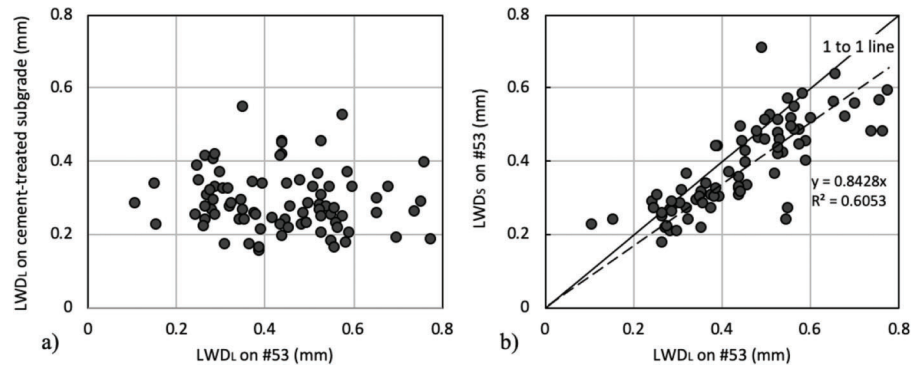


Figure 4.25 Relationship between (a) LWD_L deflections measured on subgrade and on IN #53 aggregate, and between (b) LWD_L and LWD_S deflections measured on IN #53 aggregate (data from Pads 1–5 at Site 3).

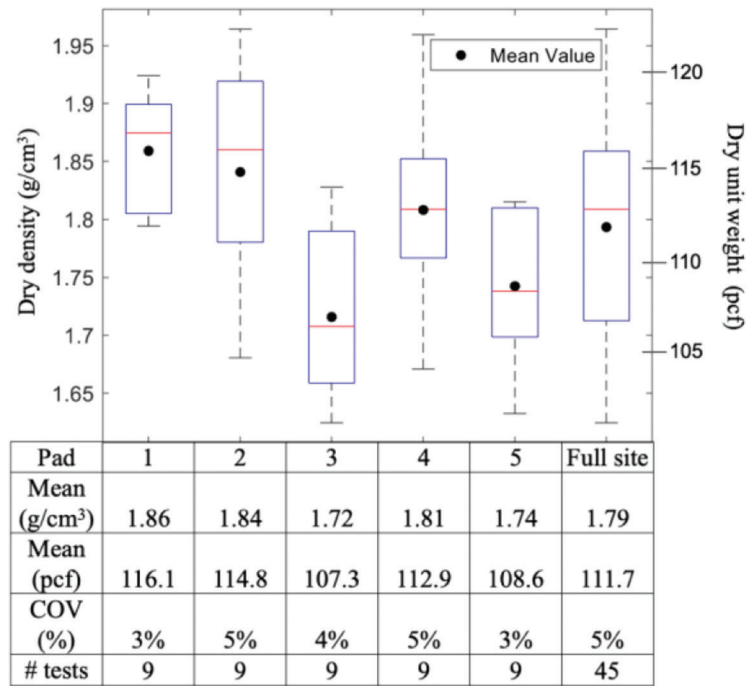


Figure 4.26 Nuclear density results for IN #53 at Site 3.

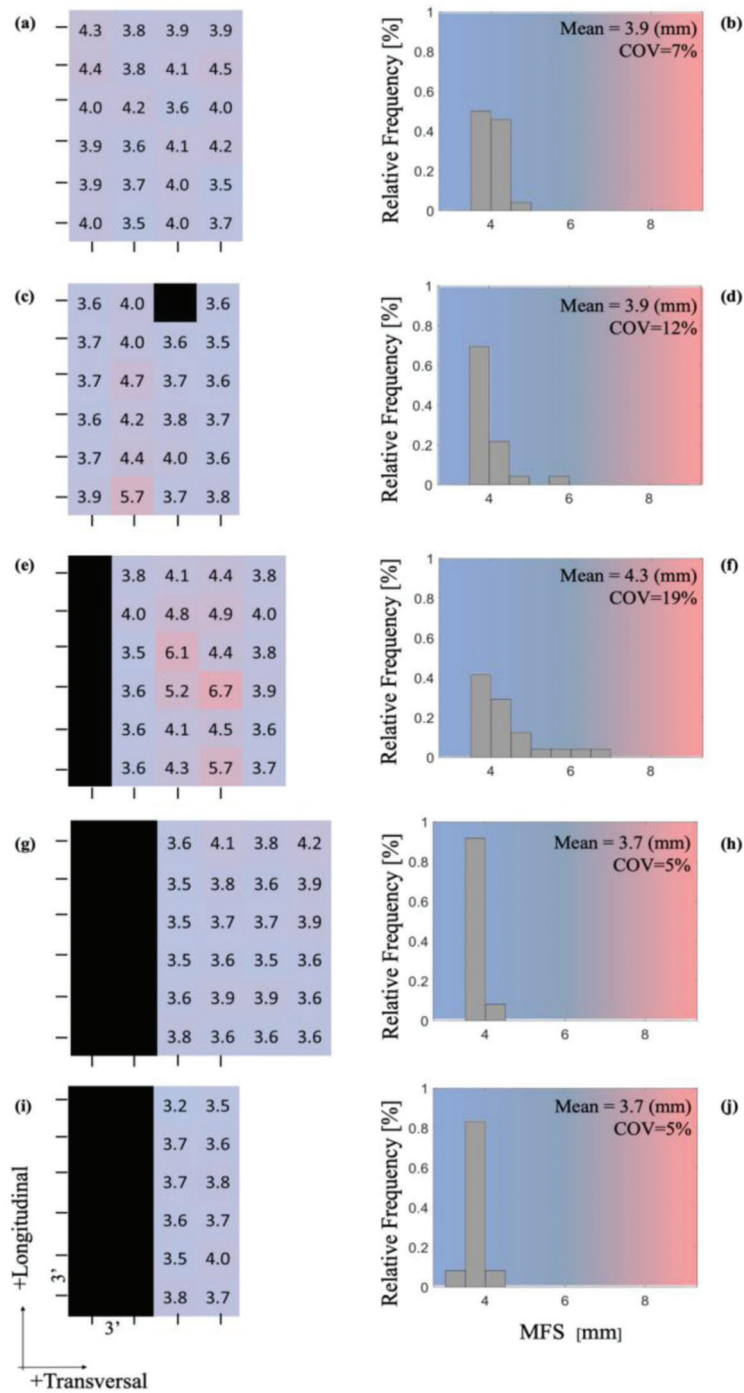


Figure 4.27 MFS data for Site 3: spatial distribution and histograms for (a–b) Pad 1, (c–d) Pad 2, (e–f) Pad 3, (g–h) Pad 4, and (i–j) Pad 5.

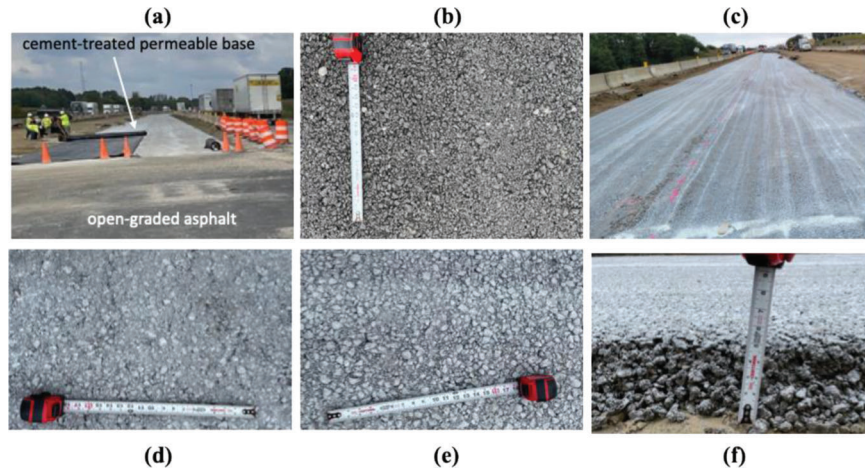


Figure 4.28 (a) View of cement-treated permeable base (CTPB) and open-graded asphalt (OGA) drainage layers at Site 3; and view of (b) OGA, (c-e) CTPB surface, and (f) thickness of CTPB layer.

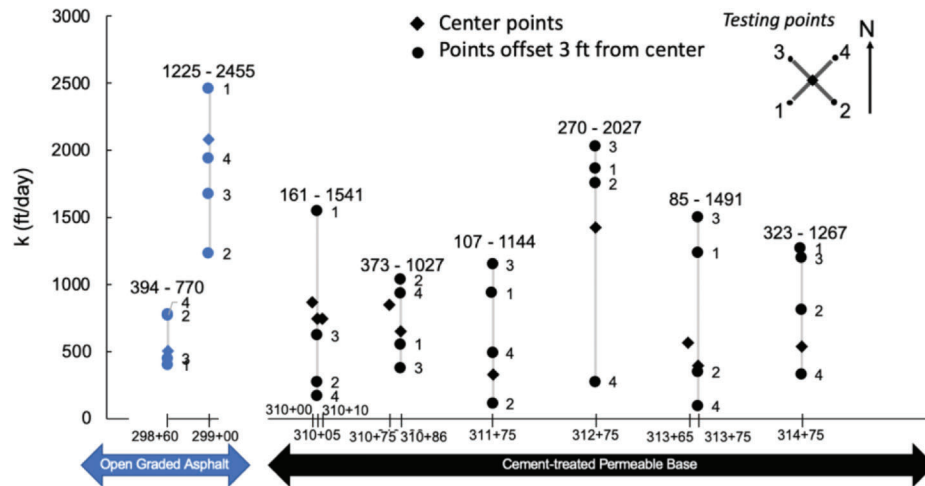


Figure 4.29 Summary of k data from APT program on open graded asphalt and cement-treated permeable base at Site 3.

TABLE 4.8
Key statistics derived from APT measurements on open graded asphalt and cement-treated permeable base at Site 3

Layer	Location	Mean (ft/day)	CV (%)	Min-Max (ft/day)	Range (ft/day)	n
Open-Graded Asphalt	298+60	573	31	394-770	376	5
	299+00	1,872	25	1,225-2,455	1,230	5
	All	1,223	62	394-2,455	2,061	10
Cement-Treated Permeable Base	310+05	665	82	161-1,540	69	5
	310+86	705	38	373-1,027	654	5
	311+75	597	72	107-1,144	1,037	5
	312+75	1,465	48	270-2,027	1,757	5
	313+75	707	87	85-1,491	1,406	5
	314+75	823	50	323-1,267	944	5
	All	818	64	85-2,027	1,942	34 ¹

¹Includes data from four additional locations where measurements were made only at the center point.

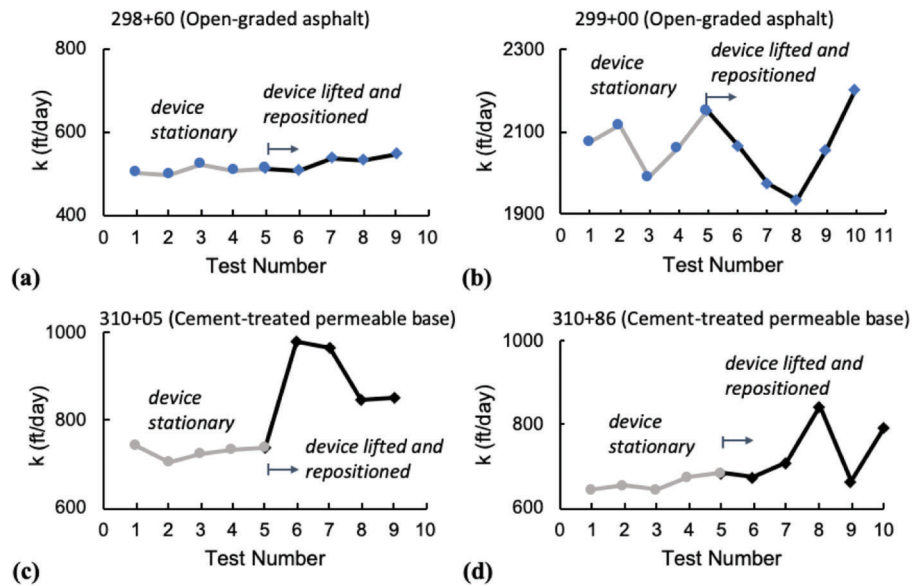


Figure 4.30 Examples of variation of k with repeat measurements at testing locations on (a–b) open graded asphalt, and (c–d) cement-treated permeable base at Site 3.

TABLE 4.9

Key statistics derived from repeat APT measurements at testing locations on open graded asphalt and cement-treated permeable base at Site 3

Layer & Station	n	Mean	CV (%)	Min	Max	Range	n	Mean	CV (%)	Min	Max	Range
OGA 298+60	5	508	2.1	496	523	27	5	528	3.1	509	547	38
OGA 299+00	5	2,079	3.0	1,989	2,150	161	6	2,064	4.9	1,934	2,201	267
CTPB 310+05	5	728	2.0	706	742	36	5	912	7.9	847	912	65
CTPB 310+86	5	660	2.7	643	683	40	6	728	10.1	665	845	180
CTPB 311+75	5	305	3.0	298	321	23	6	290	9.2	249	311	62
CTPB 312+75	5	1,443	1.6	1,423	1,475	52	6	1,575	5.5	1,456	1,680	224
CTPB 313+75	5	387	1.2	381	393	12	6	405	4.4	384	435	51
CTPB 314+75	5	522	2.0	511	534	23	6	524	3.6	505	554	49

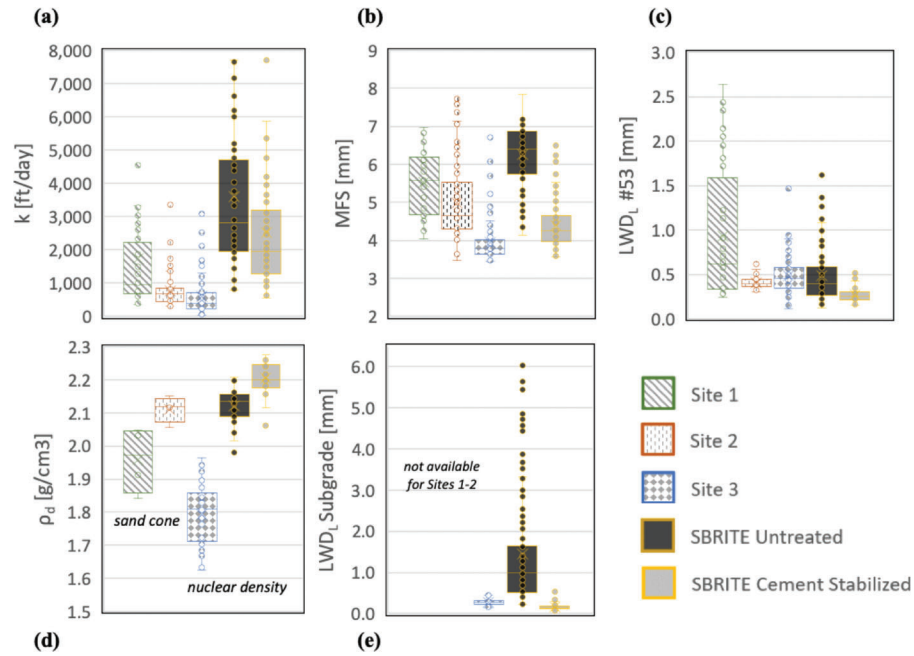


Figure 4.31 Summary of data from Sites 1–3 and from SBRITE strips: (a) k , (b) MFS, (c) LWD_L deflections, (d) dry density of IN #53 aggregate, and (e) LWD_L deflections of underlying subgrade.

TABLE 4.10

Summary of statistical indicators (mean, CV (%), minimum and maximum values, and range) of data from Sites 1–3 and from SBRITE strips

Site	IN #53 Aggregate				Subgrade
	k (ft/day) ¹	MFS (mm)	LWD_L (mm)	ρ_d (g/cm ³) ²	LWD_L (mm)
Site 1	1,751	5.7	0.93	1.96	–
	123%	16%	79%	5%	–
	353–13,133	4–8.2	0.25–2.63	1.84–2.05	–
	12,780	4.2	2.39	0.21	–
Site 2	770	5.1	0.41	2.11	–
	66%	20%	16%	2%	–
	295–3,365	3.5–8.5	0.30–0.61	2.06–2.15	–
	3,070	5.0	0.31	0.09	–
Site 3	595	3.9	0.44	1.79	0.28
	98%	14%	34%	5%	28%
	46–3,082	3.2–6.7	0.11–0.78	1.62–1.96	0.14–0.55
	3,036	3.5	0.67	0.34	0.41
SBRITE Cement Treated	2,588	4.36	0.26	2.20	0.16
	75%	15%	28%	3%	45%
	558–14,301	3.41–6.56	0.16–0.57	1.94–2.29	0.07–0.54
	13,743	3.15	0.41	0.35	0.47
SBRITE Untreated	3,600	5.97	0.48	2.09	1.44
	63%	14%	60%	4%	92%
	797–9,780	4.14–7.83	0.12–1.61	1.87–2.21	0.22–6.03
	8,983	3.69	1.49	0.34	5.81

¹ k data for Sites 1–2 derived assuming $S = 0$. Data for Site 3 and SBRITE strips corrected to account for in-situ location-specific degree of saturation.

² ρ_d values for Sites 1–2 based on a limited number of sand cone tests. Values for Site 3 and SBRITE strips based on extensive program of nuclear density tests.

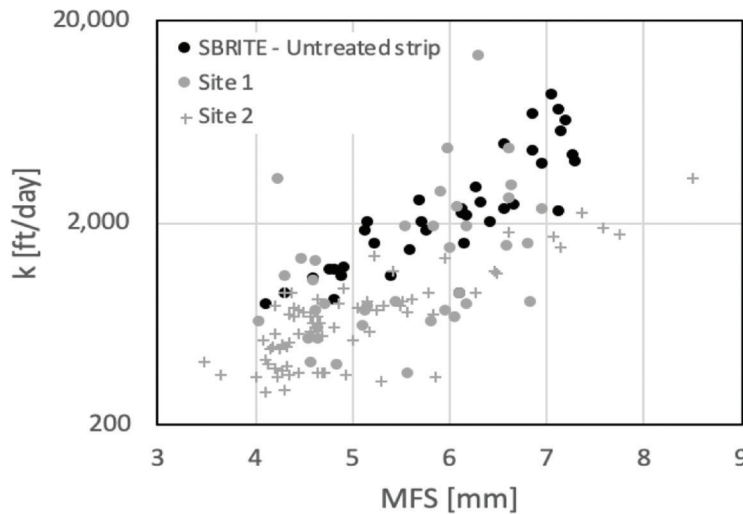


Figure 4.32 Relationship between k and MFS (only data with $S < 35\%$ from Sites 1, 2, and the untreated strip at the SBRITE site).

5. LABORATORY TESTING PROGRAM

5.1 Introduction

The laboratory testing program summarized in this chapter focused primarily on measurements of the hydraulic conductivity and was aimed at obtaining reference data for materials like those encountered in the field and at investigating aspects of the performance of the APT device. It included the following three activities.

- APT measurements on aggregate layers compacted in large crates (Section 5.2).
- Constant head and falling head tests on IN #53 aggregate using the large permeameter constructed as part of a previous project (Section 5.3). These tests were complemented by many sieve analyses.
- An APT program on pervious concrete pads (Section 5.4).

5.2 Air Permeameter Tests on Aggregate Compacted in Large Crates

Laboratory measurements using the APT apparatus were conducted in the early stages of the project to perform a preliminary evaluation of this equipment and to inform the design of the field-testing program. This section summarizes the observations and results of these tests, which were performed on aggregate compacted in large prismatic crates (cross section of 27" \times 30") (Figure 5.1). The aggregates were deposited dry in the crates and compacted using a vibratory hammer in ~ 3 –4-inch lifts. Prior to their deposition, the aggregate was mixed thoroughly in a Los Angeles Abrasion Test machine to ensure material uniformity during placement. The results from tests on five crates are presented here: three (Crates I, II, and IV) pertain to tests on one or more layers of a single aggregate; the

other two on multi-layer samples. The aggregates and the thickness of the layers are summarized in Table 5.1. Results from the five crates are presented in Table 5.2–Table 5.6. All APTs were performed using CO₂ as the permeating gas and using orifices B and/or C. Note that the dry unit weight values reported in these tables should be considered as approximate estimates as they were determined from the mass of the aggregate placed in the crate and the average thickness of the compacted sample. The latter was based on a limited number of measurements of the distance between the surface of the sample and a reference height. Given the uncertainty in the calculated ρ_{ds} , values of the relative compaction were not calculated. Instead, the samples are simply referred to as loose, dense or very dense.

Table 5.2 summarizes k values obtained from measurements at both the center and the corners of Crate I (compacted IN #53). The k values derived from measurements at the three locations are generally consistent (249–321 ft/day), and the repeat measurements at the center location are all within a few ft/day. All measured values fall at the lower end of the range reported for materials with particle size distribution like IN #53 (e.g., Getchell et al., 2020). Jones and Jones (1989) and Randolph et al. (1996), all derived from conventional laboratory methods including constant and falling head tests). They are also at the low end of the range obtained in this study from APTs performed in the field (see Chapters 3 and 4).

Additional results of APTs on IN #53 are presented in Table 5.3. In Crate II, measurements were conducted in three stages at three locations (center and two corners). The first set of measurements were made after placement and compaction of an approximately 3.6" thick layer of IN #53; additional measurements at the same location were obtained after placing a second layer (~ 1.6 " thick) of loose IN #53; the last after compaction of this last layer. The first set of measure-

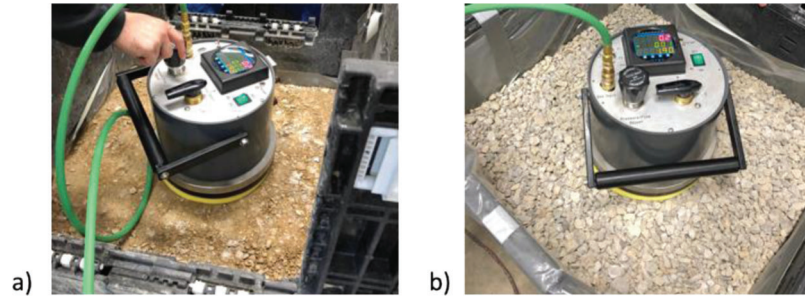


Figure 5.1 Laboratory in-crate testing of (a) IN #53, and (b) IN #8.

TABLE 5.1
Crate samples tested using APT

Crate No.	Thickness (in.)	Aggregate
I	10.8	IN #53
II	3.6	IN #53
III	5.5 (top layer)	IN #53 (top)
	6 (bottom layer)	IN #43 (bottom)
IV	9.6	IN #8
V	5.5 (bottom layer)	IN #8 (bottom)
	5.5 (bottom layer)	IN #8 (bottom)

ments (498–906 ft/day) are found to be somewhat higher than the values measured on Crate I, but still within the same order of magnitude, and in the range reported for this type of aggregate (see Getchell et al., 2020). Values approximately an order of magnitude larger are measured on the second uncompacted layer of IN #53, demonstrating the capability of the APT device to capture changes in k associated with different states of compaction. After compaction, the readings (185–867 ft/day) were again of the same order of magnitude as those previously collected for #53, albeit more scattered.

Table 5.4 summarizes the APT results for Crate III, which included a 5.5" thick layer of IN #53 over 6" of IN #43, a material with similar gradation. The data obtained from the center and the four corners of the crate fall at the low end of those measured in Crates I and II, with values less than 70 ft/day measured at three locations. Overall, despite the controlled testing conditions, the k data for compacted IN #53 obtained from Crates I–III fall in a relatively broad range. This variability may be ascribed to differences in the state of compaction, as well as to material non-homogeneity, and particularly the different percent of fines. Visual observations of the compacted aggregate surface support this hypothesis. These issues are further discussed in Section 5.3.

Data for Crate IV (compacted IN #8) are presented in Table 5.5. For this material no significant pressure could be generated in the equipment even with orifice C. According to the manufacturer, this signifies that the permeability exceeds ~20,000 ft/day. Similar difficulties were encountered using the APT to measure the

hydraulic conductivity of IN #8 in the field at the Cherry Lane site (see Figure 4.8 in Section 4.2). Collectively, these observations indicate that the APT device, in its current configuration, cannot be used to consistently measure the hydraulic conductivity of aggregates as coarse as #8.

Finally, Table 5.6 presents the APT data for Crate V, in which IN #53 aggregate was placed and compacted in two lifts (~2.7" and 2.8", respectively) over a base layer of IN #8. As shown above, this material has significantly higher permeability. k values obtained from tests on both lifts of IN #53 are compared to all other data for this same compacted aggregate in Figure 5.2. Except for Crate I, the range of k values for each crate are on the order of hundreds of feet per day. The test data for Crate V show the greatest dispersion, with a few measurements exceeding 1,000 ft/day despite the very dense conditions of the aggregate. While these data may reflect the presence of the underlying higher permeability layer, given the variability associated with the effects of density and material heterogeneity, these tests do not allow drawing definite conclusions regarding the effect of the bottom boundary. See Section 5.4 for further discussion on this point.

5.3 Hydraulic Conductivity Tests on IN #53 Aggregate

5.3.1 Falling Head Tests

Eleven falling head permeability tests were performed in 4-inch and 6-inch diameter permeameters (Karol Warner models 9110 and 9111) on IN #53. The permeameters, originally designed to test asphalt cores, consist of a thin-walled metal cylinder which holds the specimen, a manometer tube, a base which houses the permeameter pedestal and the pressure/vacuum pump and gages. The cylinder is held in place through rods and an upper clamping assembly. A rubber membrane adheres to the outside of the specimen to avoid sidewall leakage. Either vacuum (during setup) or pressure (during testing) is applied to the outside of the membrane through a line connected to a built-in hand pump. The top cap and the bottom pedestal protrude into the cylinder and O-rings around the caps create a seal. This protrusion limits the height of specimens to approximately 4 in. for both permeameters.

TABLE 5.2
Summary of APT data from tests on Crate I (compacted IN #53)

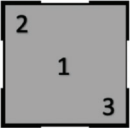
Crate 1–10.8" compacted IN #53		Orifice	γ_d (pcf) [kN/m ³]	Thickness (in) [cm]	k (ft/day) [m/s]	
	1	B	137.3	10.8	312 [1.10·10 ⁻³]	
	2		[21.6]	[27.46]	249 [8.78·10 ⁻⁴]	
	3		Dense		321 [1.13·10 ⁻³]	
	1				298 [1.05·10 ⁻³]	
Repeat measurements					300 [1.06·10 ⁻³]	
					294 [1.04·10 ⁻³]	
					292 [1.03·10 ⁻³]	

TABLE 5.3
Summary of APT data for Crate II (two layers of IN #53)

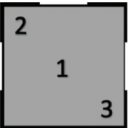

Layer	Location	Orifice	γ_d (pcf) [kN/m ³]	Thickness (in) [cm]	k (ft/day) [m/s]	
3.6" compacted IN #53	1	B	149.2 [23.4] <i>Very dense</i>	3.6 [9.2]	906 [3.20·10 ⁻³]	
	2	B			498 [1.76·10 ⁻³]	
	3	B			548 [1.93·10 ⁻³]	
	2	B			586 [2.07·10 ⁻³]	
1.6" loose #53 on top of 3.6" compacted IN #53	1	C	120.5 [18.9] <i>Loose</i>	1.6 [4.0](thickness second layer)	4,505 [1.59·10 ⁻²]	
	2	C			6,469 [2.28·10 ⁻²]	
	3	C			7,836 [2.76·10 ⁻²]	
1.6 compacted #53 on top of 3" compacted IN #53	1	B	133.6 [20.9] <i>Dense</i>	1.42 [3.6](thickness second layer)	179 [6.31·10 ⁻⁴]	
		B			185 [6.53·10 ⁻⁴]	
	2	B			867 [3.06·10 ⁻³]	
		B			846 [2.98·10 ⁻³]	
	3	B			368 [1.30·10 ⁻³]	

TABLE 5.4
Summary of APT data for Crate III (compacted IN #53 over compacted IN #43)

	Location	Orifice	γ_d (pcf) [kN/m ³]	Thickness (in) [cm]	k (ft/day) [m/s]	
5.5" of compacted IN #53 over 6" of compacted IN #43	1	B	151.5	5.5	69 [2.43·10 ⁻⁴]	
	2		[23.7]	[14]	56 [1.98·10 ⁻⁴]	
	3		Very dense		105 [3.70·10 ⁻⁴]	
	4				45 [1.59·10 ⁻⁴]	
	5				331 [1.17·10 ⁻³]	
	1				51 [1.80·10 ⁻⁴]	
	5				307 [1.08·10 ⁻³]	

To accommodate tests on the unbound aggregate IN #53 aggregate modifications were made to the permeameter. First, a 3/4-inch diameter plastic tube was added at the outlet so the exit piezometric head could be positioned above the specimen. This allowed falling head tests to be performed at lower gradients. Additionally, given the unbound nature of the material tested, a geotextile woven fabric of high permittivity was used as a filter, and a metal wire sheet was inserted below for stability.

Six-inch diameter specimens were prepared in a standard Proctor mold using vibratory hammer before transferring the mold to the permeameter. Falling head tests were performed first increasing then decreasing the starting head to cover hydraulic gradients in the 0.2–2 range. k values from the 11 tests performed are plotted

as a function of the specimen dry density in Figure 5.3. Four sets of data are shown corresponding to different ranges of the hydraulic gradient. While in all specimens, k is found to decrease with increasing gradient, except for one test, the data for $i \sim 0.2$ and $i \sim 0.4$ all fall within a few percent of each other, indicating laminar or close-to-laminar conditions. This is supported by calculations of the Reynolds number based on D_{50} of the aggregate. For larger gradients, the reduction in k is significant (e.g., for $i \sim 2$ k is approximately half of the value measured with $i \sim 0.2$) indicating non laminar conditions.

Figure 5.3 also clearly highlights the dependence of the hydraulic conductivity on the specimen's dry unit weight, with k varying by a factor of six over the range of unit weights explored in the tests. In general, the

TABLE 5.5
Summary of APT data for Crate IV (compacted IN #8)


	Location	Orifice	γ_d (pcf) [kN/m ³]	Thickness (in) [cm]	k (ft/day) [m/s]	
#8	1 center point	C	104.3 [16.4] Dense	9.6 [24.29]	>20,000 [7.04·10 ⁻²]	

TABLE 5.6
Summary of APT data for Crate V

	Location	Orifice	γ_d (pcf) [kN/m ³]	Thickness (in) [cm]	k (ft/day) [m/s]
2.75 of compacted #53 over 6" of compacted #8	1	B	146.6	2.75	231 [8.15·10 ⁻⁴]
	2	B	[23.0]	[6.98]	1,256 [4.43·10 ⁻³]
		C	Very dense		870 [3.07·10 ⁻³]
	3	B			869 [3.07·10 ⁻³]
		C			628 [2.22·10 ⁻³]
	4	C			1,618 [5.71·10 ⁻³]
	5	C			360 [1.27·10 ⁻³]
		B			586 [2.07·10 ⁻³]
	1	B			562 [1.98·10 ⁻³]
		C			385 [1.36·10 ⁻³]
5.5" of compacted #53 over 6" of compacted #8	1	B	151.4	5.53	2,018 [7.12·10 ⁻³]
	2	C	[23.7]	[14.0]	1,737 [6.13·10 ⁻³]
	3	B	Very dense		753 [2.66·10 ⁻³]
		C			467 [1.65·10 ⁻³]
	4	B			266 [9.38·10 ⁻⁴]
		C			160 [5.68·10 ⁻⁴]
	5	B			324 [1.14·10 ⁻³]
	1	B			202 [7.13·10 ⁻⁴]

values of k obtained in the falling head tests on the dense specimens ($\gamma_d > 128$ pcf) indicate the suitability of compacted IN #53 to function as a drainage layer.

5.3.2 Constant Head Tests in Large Permeameter

Additional measurements of the hydraulic conductivity of IN #53 were obtained from constant head tests performed using the large stainless steel permeameter cell designed and constructed as part of a previous research project (Getchell et al., 2020). The permeameter cell itself is built from ¼"-thick stainless-steel plates and is designed to house a prismatic soil sample with a 12" (W) × 10" (H) cross section and a 36" length. The top cover of the cell is stiffened with reinforcing bars and secured to the top of the cell with 28 bolts. Figure 5.4 summarizes the steps followed to prepare the samples for testing. The first image (Figure 5.4a) shows the empty permeameter with the screens positioned both at the upstream and downstream ends (see detail in Figure 5.4h). A thin foam layer is placed at the bottom of the permeameter prior (Figure 5.4b) to introducing the aggregate to avoid any preferential flow through the bottom of the sample. The aggregate is then placed and compacted in three lifts using a vibratory hammer placed on a wooden tamper (see Figure 5.4i). Figure 5.4c shows the final lift after compaction.

Expandable polyurethane foam is then sprayed on top of the sample.

Note that the white foam fabric shown at the ends (see asterisk on image) covers only the portion of the screen above the sample and is intended to ensure that the sprayable foam does not enter the ends of the permeameter. A thick rubber foam is then placed on top of the sprayed foam, and a second layer of polyurethane foam is sprayed on top. The expansion of the two layers of foam provides the seal between the sample and the cover and a rubber gasket (Figure 5.4f) ensures that the enclosure is watertight. Figure 5.4g shows the closed permeameter. Two stainless steel handles are welded to the cover to facilitate its lifting and placement. A port on the cover enables the application of vacuum during the saturation stage.

Two-inch flexible plastic tubing and valves connect the cell to two reservoirs. The upstream reservoir is mounted over an adjustable platform through which the upstream head and thus the hydraulic gradient are controlled. Upstream and downstream water levels are accurately and semi-continuously determined using two Banner LE250IQ laser displacement sensors which measure the distance to floating targets on each reservoir. Flowrate is determined from measurements using a precision digital scale of the mass of water coming out of the downstream end of the permeameter.

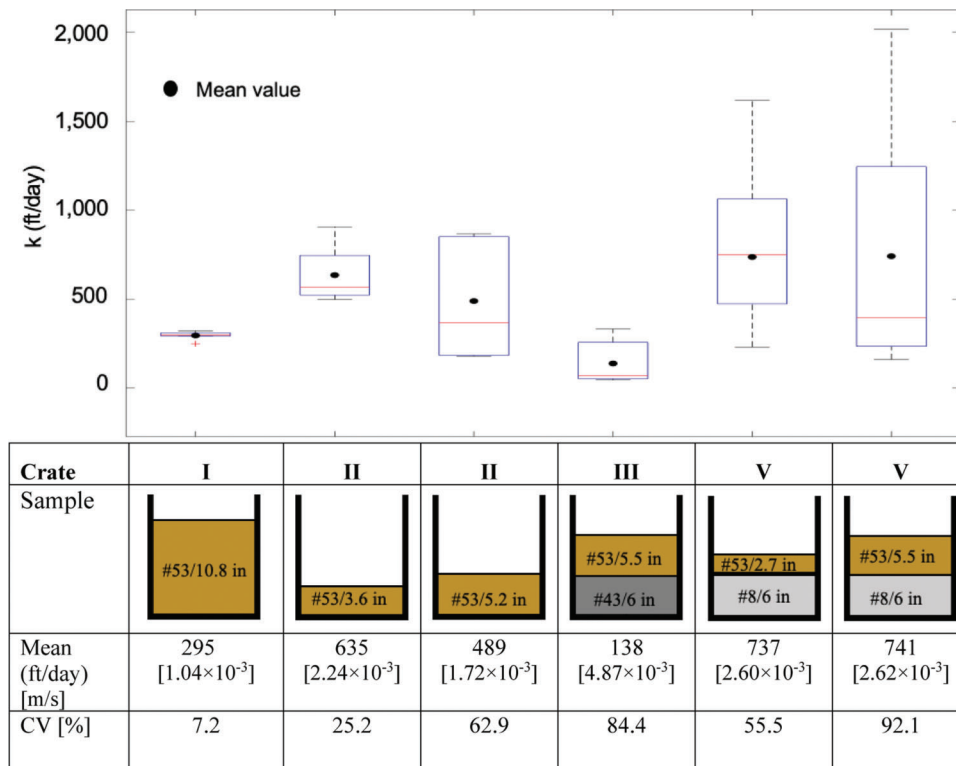


Figure 5.2 Comparison of laboratory APT data for IN #53 (Crates I, II, III, and V).

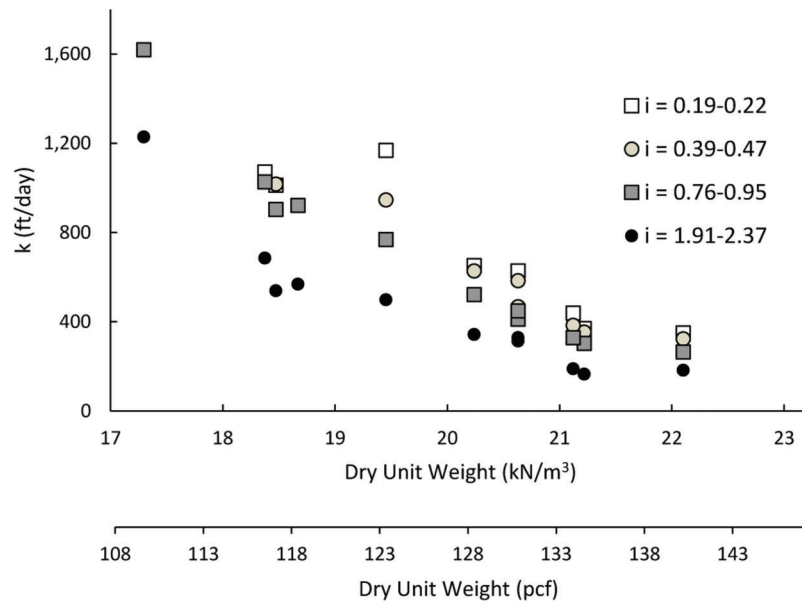


Figure 5.3 Hydraulic conductivity data from 11 falling head tests on IN #53 (for each test, the figure shows only data from measurements obtained by increasing the hydraulic gradient).

All instrumentation is collected digitally in real time using a laptop computer (Figure 5.5a).

All tests performed as part of this research project included five stages. During each stage the gradient was increased in steps to a maximum target value (nominal values of 0.05, 0.11, 0.23, 0.11, and 0.05) and then decreased back to zero (Figure 5.5b). Figure 5.5c shows

an example of the data obtained from one of these stages: the gradient calculated over each step from the laser displacement measurements of the head at the upstream and downstream ends, and the mass of water flowing through the sample. The latter measurement is used to calculate the flow rate (q) and discharge velocity (v) through the sample. Values of k can then be



Figure 5.4 (a–g) Preparation of compacted sample in large permeameter; (h) detail of screens at ends of permeameter; and (i) compaction of last aggregate lift with vibratory hammer on wooden pad.

determined from average values of v and i over each step of each stage using Darcy's law (11 values for the stage shown in Figure 5.5c).

As summarized in Table 5.7, six tests were performed following the above procedure. Five (tests I–V) were conducted on IN #53 obtained from the same source used to construct the testing strips at the SBRITE center (Chapter 4). Test VI used IN #53 from a different source. In tests I–III, the aggregate was placed and compacted dry, while in the remaining three tests it was compacted wet at a water content of $\sim 8\%$ – 9% . The latter procedure was adopted to limit segregation during placement that appeared to affect the earlier samples (see more on this below). Each test made use of new aggregate, except for test IV, which reused the same aggregate from test III. Prior to placement in the permeameter, the total aggregate required to prepare the sample was homogenized in a large concrete mixer. Values of the dry unit weight in Table 5.7 were calculated from the mass of the aggregate placed in the permeameter and of the volume occupied by the soil. Based on a γ_{dmax} value of 140 pcf derived for a similar aggregate (Getchell et al., 2020), the dry unit weights for tests I–V in Table 5.7 correspond to values of the relative compaction between 94.3% and 98.6%. A significantly lower value of relative compaction ($\sim 84\%$) was achieved in the last test, which, however, made use of aggregate from a different source.

After completion of the tests, sieve analyses were performed on five sub-samples of the aggregate extracted from different locations within the permeameter.

For tests I and II, the sieve analyses were performed dry. For the aggregate from tests IV, V, and VI, this procedure was modified to include washing of the material prior to sieving as detailed in ASTM D6913.

Figure 5.6a–c shows the results of the hydraulic conductivity tests I, II, and IV. In each of these tests, measurements across the different stages produced consistent values of k . In all cases k remained constant up to $i \sim 0.1$ (slightly smaller threshold for test IV) and reduced at higher gradients. In the other tests, however, k was found to start increasing steadily at some point during the test. As an example, Figure 5.7 shows the data obtained from test VI. In this test, the effluent appeared cloudy after the first two stages, suggesting that the increase in k was due to washing of the fines out of the sample. A similar issue was encountered in test V. In test III, the increase in k was sudden and rapidly exceeded an order of magnitude suggesting rupture of a seal. This required immediate interruption of the test. For these tests, only data from the early stages are considered reliable, as summarized in Table 5.7.

Values of k derived in the six tests from the data collected at small gradients (less than ~ 0.11) are summarized in Table 5.7. Despite the common aggregate source, and the relatively consistent values of the placement dry unit weight (132–138 pcf), the values of k derived from tests I–V vary significantly (from 16 ft/day to over 800 ft/day). At the high end of this range are the values obtained from the tests in which the aggregate was placed and compacted dry. Visual observations

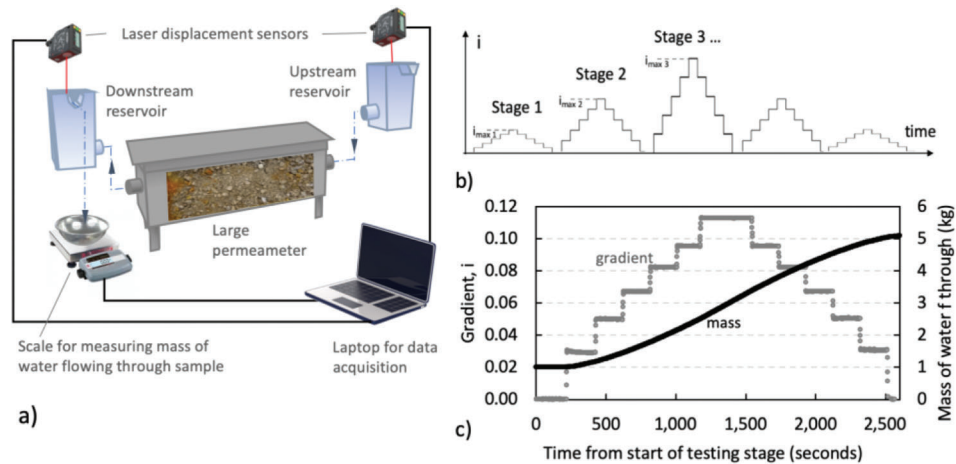


Figure 5.5 (a) Setup for constant head tests in large permeameter, (b) testing protocol, and (c) example of data from a single stage.

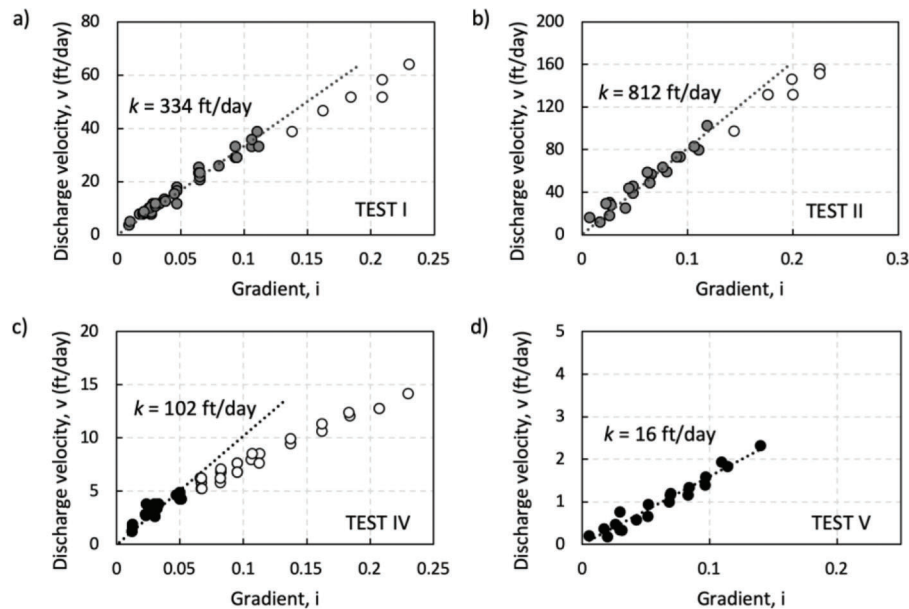


Figure 5.6 Data collected from large permeameter tests: (a) I (stages 1–5), (b) II (stages 1–5), (c) IV (stages 1–5), and (d) V (stages 1–2). Darker symbols identify data used to calculate value of k displayed.

during sample preparation (e.g., see pictures of the compacted aggregate surface in tests I and II in Figure 5.9) suggest that this procedure yielded heterogeneous samples. Note also how the coarser appearance of the aggregate surface in test II (Figure 5.9c) relative to test I (Figure 5.9b) is consistent with the higher k measured in this test (Table 5.7 and Figure 5.6).

As discussed above, sieve analyses were performed on five samples from the permeameter after completion of the test. Sample results are presented in Figure 5.8a–d for tests I, II, V, and VI. Each figure includes the particle size distributions obtained from the five subsamples, as well as the composite curve. The locations from where the subsamples were extracted are shown in Figure 5.8e. To start, the data show variability between the different tests. Focusing on the composite curve for

each test, the percentage of fines (<0.075 mm) varies significantly: 2%–4% in tests I and II versus 8%–14% in tests IV–VI (note that the upper value falls out of the range for IN #53 gradation). While this may provide an explanation for the higher conductivity measured in tests I and II, recall that for these two tests alone, the sieve analysis was performed dry. This procedure is likely to underestimate the percentage of fines. For any given test, variability in particle size distribution is also observed between subsamples. While no consistent trend with location is observed, this supports the hypothesis above that heterogeneity in the sample may have controlled the measured hydraulic conductivity.

Finally, as shown in Figure 5.9, in tests I and II, measurements were performed across the surface of the

aggregate lifts using the APT. Due to the proximity to the permeameter edges/ends, the values obtained from these tests should not be viewed as representing the hydraulic conductivity of the underlying material. They can however provide a sort of “*k* index” that can be used for comparison between and across samples. Nine measurements (three per lift) were performed on the compacted samples in tests I and II. Consistent with the values of *k* derived from the constant head tests (see Figure 5.6), at all locations measurements performed

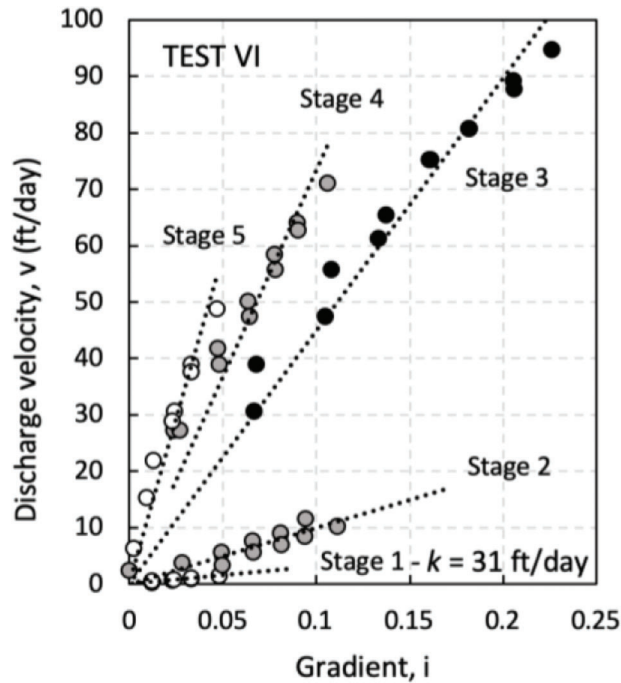


Figure 5.7 Data for test VI in which *k* increased over time. For this test only the measurements from the first stage are considered reliable.

TABLE 5.7
Summary of tests performed in large permeameter

Test	Aggregate	Placement/ Compaction Conditions	Dry Unit Weight (pcf) [kN/m ³]	<i>k</i> (ft/day) [m/s] (for <i>i</i> < ~0.11)	Test Stages for Which Data Are Considered Reliable
I	IN #53 (same source	Dry	136 [21.3]	334 [1.18·10 ⁻³]	All
II	used for SBRITE	Dry	136 [21.3]	812 [2.86·10 ⁻³]	All
III-3 (1)	strips)	Dry	138 [21.6]	245 [8.64·10 ⁻⁴]	Stages 1-2 Test interrupted due to rapid increase in <i>k</i> suggestive of rupture of a seal.
IV 3-B-3 (1)		Wet w~9%	138 [21.6]	102 [3.60·10 ⁻⁴]	All
V 4 (2)		Wet w~9%	132 [20.8]	16 [5.64·10 ⁻⁵]	Stages 1-mid-way 3 Subsequent two-fold increase in <i>k</i> suggests internal erosion
VI S5 (3)		Wet w~8%	118 [18.6]	31 [1.09·10 ⁻⁴]	Stage 1 Subsequent increase in <i>k</i> and cloudy water exiting sample suggest internal erosion.

on the test II sample exceeded those on the test I aggregate. On average the ratio between the two measurements was equal to 2.8, comparable to the ratio (3.4) based on the data from the large permeameter (Figure 5.6a-b).

5.4 Tests on Pervious Concrete Pads

Two pervious concrete pads (Figure 5.10) were manufactured and tested using the APT to investigate select aspects of the performance of the APT device under more repeatable and controlled conditions that could be achieved when testing aggregate samples.

Materials and support for mixing and casting were generously provided by Irving Materials. Two independent batches were prepared using cement, silica fume, pea gravel (maximum diameter = 0.5") and water and the same mix design (w/c = 0.34, gravel/cement = 5.1, cement/silica fume = 21) to cast the two pads. The pads with dimensions of 2' × 2' × 4" and 1.4' × 1.4' × 4" were cast in wooden frames placed on a rigid base covered by an impermeable plastic sheet. Falling head tests were performed on cylinders cast from each batch. *k* values derived from these tests show significant variation even for cylinders obtained from the same batch, and a strong dependence on the hydraulic gradient. At the lowest gradient examined (0.20), *k_{sat}* varied between ~2,000 and ~5,000 ft/day, at the high end of the range of interest to this research. Values 2–2.3 times smaller were measured for *i*~2.

Tests using the APT apparatus were performed on the pads at two different stages of the research project by different operators. The first set of tests was performed in March 2022; the second in October 2023. Given the time lag between the tests, the results from these two sets of tests are not directly comparable.

The APT testing program was designed to quantify the repeatability and accuracy of the device, and to

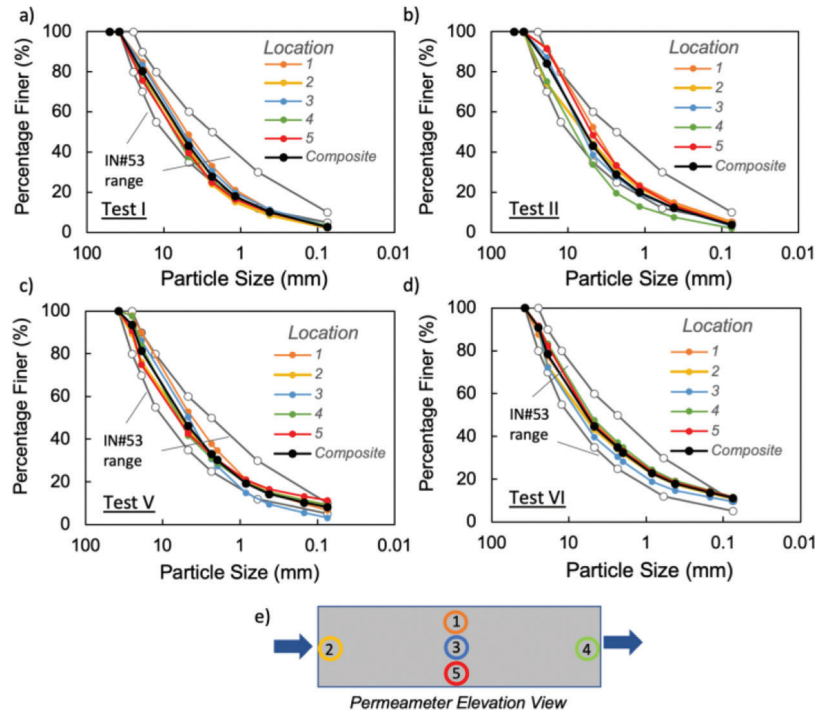


Figure 5.8 (a–d) Example of particle size distributions of aggregate retrieved from locations shown in (e) after completion of flow tests.

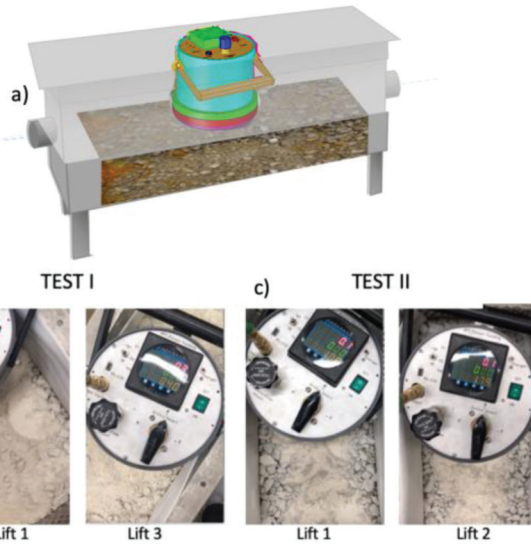


Figure 5.9 APT testing of compacted aggregate inside large permeameter: (a) schematic of setup, (b) view of aggregate surface in Test I, and (c) view of aggregate surface in Test II.

explore the impact of the boundary conditions. With these goals in mind, it included the following.

- *Repeat measurements at a fixed location* both keeping the device stationary, and lifting and repositioning it, carefully targeting the same testing point, like the field experiments described in Sections 3.4.5 and 4.4.2.
- Tests at the center and at the corners (8" from the edges) of the pads *modifying the lower and lateral boundary*

conditions to explore the impact of the boundary drainage conditions.

- *Tests at different locations on the pads* to collect data that could be directly compared to those derived from falling head tests performed on cylinders cored from the pads and thus support the accuracy of the device.

5.4.1 Tests Examining Repeatability of APT

To quantify the repeatability of the device, repeat measurements were performed at the same location point, both keeping the device stationary, and lifting and repositioning it, carefully targeting the same testing point. The first set of tests (see select results in Figure 5.11 [data from March 2022] and Figure 5.12 [data from October 2023]) were intended to measure the inherent repeatability of the measurement. As illustrated by Figure 5.11 and Figure 5.12, they yielded values of the coefficient of variation (CV) less than 2.5%, and in most cases less than 1%. This is consistent with the data reported in Table 4.9 from tests performed in the field.

Also consistent with previous field experience, CV values derived from repeat measurements performed after lifting and repositioning the APT device were consistently higher (e.g., see Figure 5.11a–b) regardless of the testing location (center or corners of the pad) and the bottom and side boundary conditions (further discussed below) but remained below ~8% (see also additional data in Table 5.8). This increased scatter is thought to reflect slight differences in the manner the pad and the APT device are positioned and local

material variability. Note that while use of the pervious concrete was thought to minimize material variability, as discussed below, this was not necessarily found to be the case, as differences in permeability were measured between the two pads and across each pad.

5.4.2 Tests Examining Effect of Boundary Conditions

Table 5.8 summarizes tests performed on the large pad in March 2022. Tests were performed with three different configurations.

1. Pad in casting form resting on rubber foam (i.e., seal at both sides and bottom boundary).

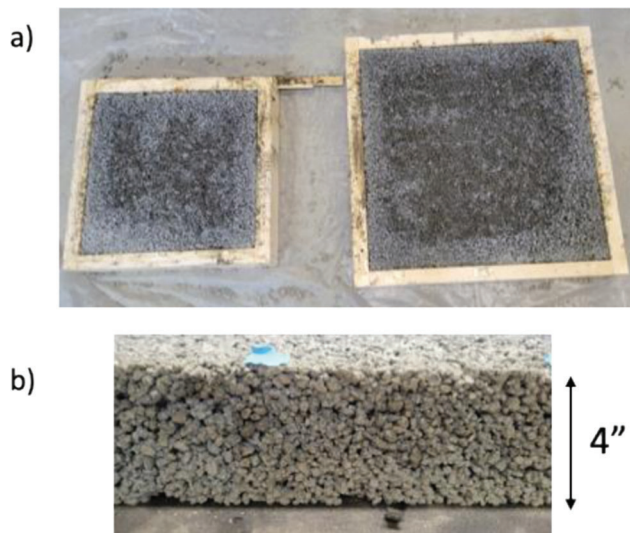


Figure 5.10 (a) Concrete pads in forms, and (b) side view of pad thickness.

2. Pad in form lifted on blocks (i.e., seal only at sides, open bottom boundary).
3. Pad out of form resting on rubber form (i.e., seal only at bottom boundary).

The first three rows in the table refer to tests performed at the center of the pad (Figure 5.13). Data for these same tests are shown in Figure 5.15. The data from the first two sets of measurements are found to be statistically different (p -value from t -test $< 10^{-3}$), with higher values of k measured with the pad in the lifted position (open bottom boundary). This indicates that the bottom boundary may affect APT measurements performed on layers as thick as 4". Note that this result was not replicated in the tests performed at the center of the small pad (Table 5.9), i.e., for this pad no statistical difference was observed between tests performed with the pad lifted or resting on the rubber foam.

Comparison of first and third testing conditions shows that the edge boundary conditions did not impact the data collected at the center of the pad. In contrast, measurements at the corners of the large pad (see testing position in Figure 5.13b and data in bottom rows of Table 5.8 and in Figure 5.15) were affected by the boundary conditions at the edges, all exhibiting an over 50% increase in hydraulic conductivity when the formwork was removed. The data in Figure 5.15 also highlight the variability in k measured on the pads. This is discussed further below.

Additional tests to explore the impact of the boundary conditions were performed in October 2023. Tests were performed with four different configurations, as summarized below. In two of these, a sprayable polyurethane foam (designed to expand for sealing cracks and gaps as large as 1") was used to treat the surface of the pad (the bottom face and the sides) to create a seal.

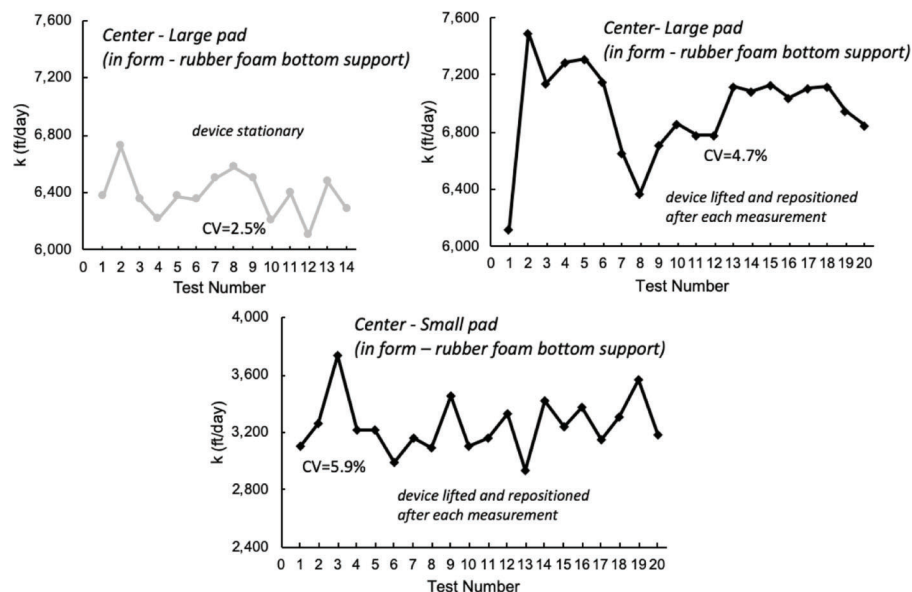


Figure 5.11 Examples of results of repeat APT measurements on pervious concrete pads (tests from October 2022—all with identical boundary conditions).

TABLE 5.8
Summary of APT data from tests performed on a 2 ft × 2 ft pervious concrete pad in March 2022

Location and Boundary Conditions				No. Tests ¹	Mean (ft/day)	SD (ft/day)	CV (%)	Range (ft/day)
Pad	Location	Edges	Bottom					
2 × 2	Center	In form	Rubber foam	20	6,955	325	4.7	6,119–7,492
2 × 2	Center	In form	Open (lifted)	10	7,507	420	5.6	7,078–8,206
2 × 2	Center	Open (form removed)	Rubber foam	5	6,795	527	7.8	6,013–7,434
2 × 2	Corner A	Form	Foam	5	2,515	102	4.1	2,417–2,642
2 × 2	Corner A	Open	Foam	5	4,104	215	5.2	3,895–4,443
2 × 2	Corner B	Form	Foam	5	4,064	189	4.6	3,828–4,352
2 × 2	Corner B	Open	Foam	5	6,786	188	2.8	6,542–6,975
2 × 2	Corner C	Form	Foam	5	2,768	116	4.2	2,632–2,862
2 × 2	Corner C	Open	Foam	5	4,471	274	6.1	4,264–4,870
2 × 2	Corner D	Form	Foam	5	4,313	165	3.8	4,077–4,447
2 × 2	Corner D	Open	Foam	5	6,613	179	2.7	6,381–6,839

¹Repeat measurements were performed lifting and repositioning the APT device.

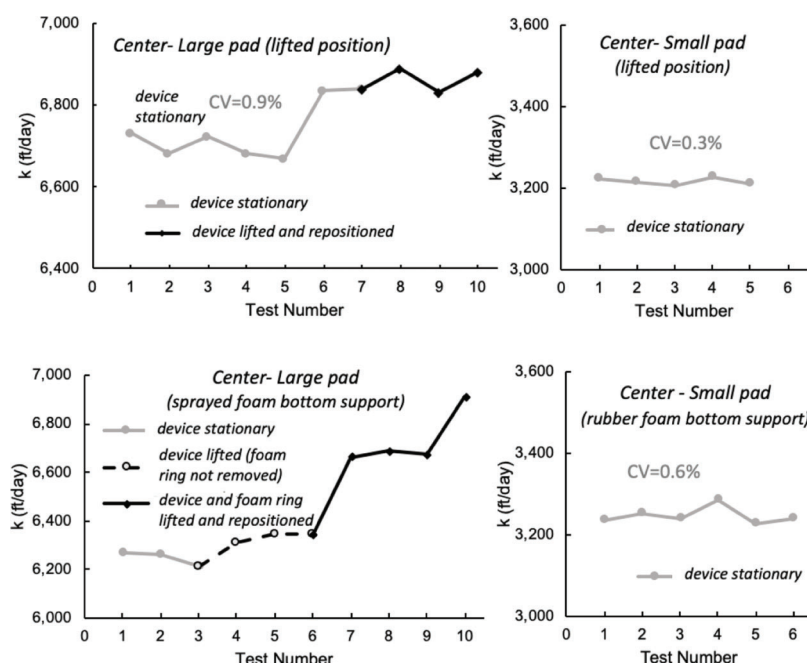


Figure 5.12 Examples of results of repeat APT measurements on pervious concrete pads (tests performed in October 2023).

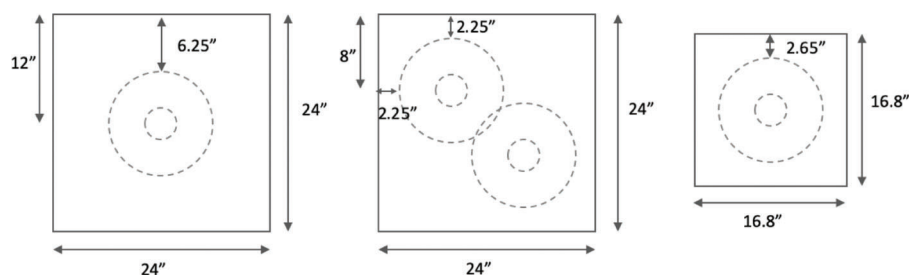


Figure 5.13 Position of APT apparatus when testing (a) center of large pad, (b) corners of large pad, and (c) center of small pad (refer to Figure 2.2 for dimensions of apparatus).

TABLE 5.9
Summary of APT data from tests performed on a 1.4 ft × 1.4 ft pervious concrete pad in March 2022

Location and Boundary Conditions				No. Tests ¹	Mean (ft/day)	SD (ft/day)	CV (%)	Range (ft/day)
Pad	Location	Edges	Bottom					
1.4' × 1.4'	Center	Form	Rubber foam	20	3,250	191	5.9	2,935–3,733
1.4' × 1.4'	Center	Open	Rubber foam	5	2,957	45	1.5	2,908–3,026
1.4' × 1.4'	Center	Form	Open	10	3,225	177	5.5	2,995–3,490

¹Repeat measurements were performed lifting and repositioning the APT device.

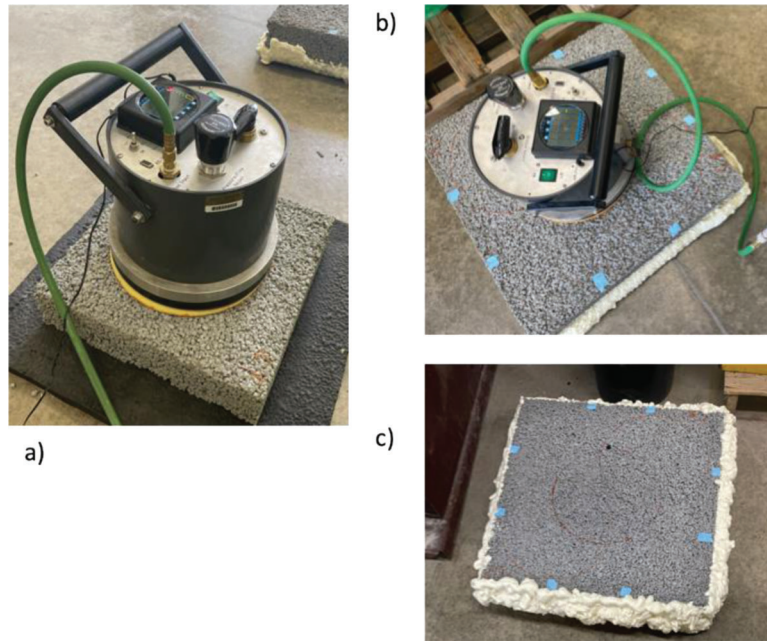


Figure 5.14 Air permeameter testing of (a) small pad on rubber foam; (b) large pad with sprayed foam bottom support; and (c) large pad after treatment of base and sides with spray foam (note: marking on pad ensured consistent positioning of APT device).

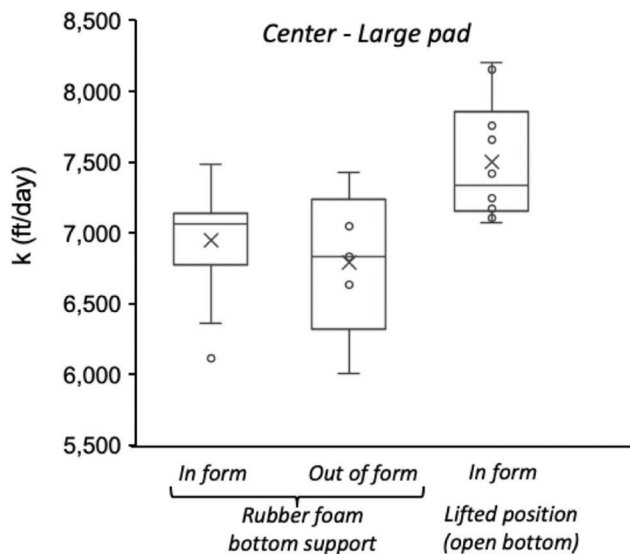


Figure 5.15 APT measurements on large pad with different bottom and edge boundary conditions (tests from March 2022, see statistics in Table 5.8).

Except for the last testing configuration, the edges of the pads were left open.

- Pad lifted on blocks (i.e., open bottom and open edge boundaries).
- Pad resting on rubber foam (i.e., seal at bottom boundary but open edges) (Figure 5.14a).
- Bottom of pad treated with spray foam (i.e., seal at bottom boundary but open edges) (Figure 5.14b).
- Bottom and sides of pad treated with spray foam (i.e., seal at both sides and bottom boundary) (Figure 5.14c).

Table 5.10 and Figure 5.16 summarize the data from these tests, which again show a statistically significant difference between the data obtained with the open bottom boundary and those from the other three testing configurations (p-values from t-test < 10⁻³).

5.4.3 Comparison of APT and direct measurements of k

Cores 5.25 inches in diameter were obtained 8" from the edges of the large pad and at the corners of the small pads (see Figure 5.19c). Falling head tests were

TABLE 5.10
Summary of APT data from tests performed on a 2 ft × 2 ft pervious concrete pad in October 2023

Location and Boundary Conditions				No. Tests ¹	Mean (ft/day)	SD (ft/day)	CV (%)	Range (ft/day)
Pad	Location	Edges	Bottom					
2' × 2'	Center	Open	Open	10	6,777	87	1.3	6,671–6,891
2' × 2'	Center	Open	Rubber foam	3	6,490	–	–	6,470–6,520
2' × 2'	Center	Open	Spray foam	10	6,433	190	2.9	6,212–6,686
2' × 2'	Center	Spray foam	Spray foam	3	6,470	–	–	6,404–6,592

¹Repeat measurements were performed lifting and repositioning the APT device.

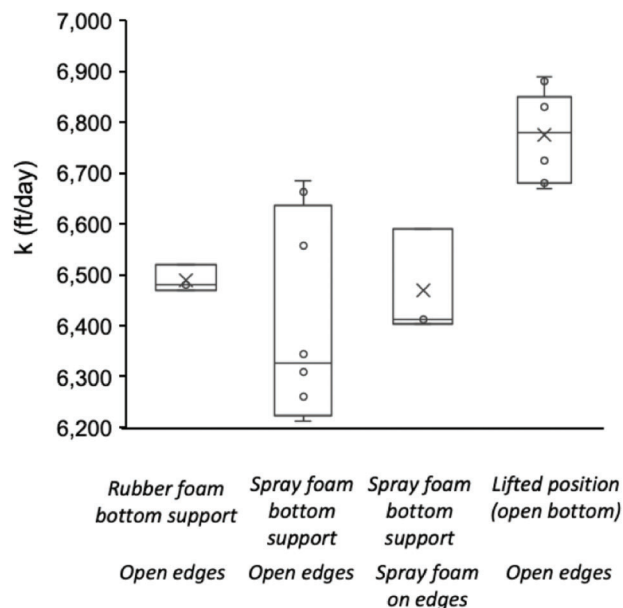


Figure 5.16 APT measurements on large pad with different bottom and edge boundary conditions (tests from October 2023, see statistics in Table 5.10).

performed on all the cores using the 6-inch diameter setups used for the tests on the IN #53 aggregate (Section 5.3.1).

Figure 5.17 shows results for the cores obtained from the center locations on the two pads. For both cores k is found to decrease with increasing gradient throughout the range of gradients investigated (~ 0.25 – 4). As observed in the APT tests, the hydraulic conductivity of the core from the large pad exceeds that of the core from the small pad by a factor of 1.5–1.9. The gray bars in the figure depict the range of k values derived from the APT tests conducted at the center of the pads. They are observed to be generally consistent with the falling head measurements at low gradients. Note that exact

correspondence between the APT and falling head test values should not be expected because of the different flow conditions in terms of gradient and geometry (in the APT flow occurs both vertically and radially) occurring in the two tests. Moreover, in the APT, the measurement is affected by the characteristics of a much larger volume of material and thus local variability in k plays a role. While the use of pervious concrete was thought to minimize variability, k values from falling head tests across the two pads varied significantly as illustrated in Figure 5.18 which summarizes values derived for all the cores in correspondence to gradients of 0.3–0.34 and 1.4–1.7. For a given gradient, the k values determined from the cores vary by a factor of 2 to 3 (e.g., for $i = 0.30$ – 0.34 , $k = 3,633$ – $10,263$ ft/day). APT tests performed near each other also showed evidence of significant local variability. For example, tests at six locations offset from the center of the large pad by less than 2" yielded k values differing by over 2,000 ft/day.

Considering these factors, it is preferable to compare the APT and falling head data as a whole. This is done in Figure 5.19, which presents boxplots for both falling head (lowest gradient, $i \sim 0.3$) and APT results for all pads (Figure 5.19a) and for the large pad only (Figure 5.19b). Testing locations on the two pads are shown in Figure 5.19c. Note that the APT values reported in the figure represent mean values from repeat measurements under different boundary conditions at 14 different locations, and the mean and coefficient of variation values reported are derived from these mean values. This was deemed preferable as the number of measurements at the center of the pads greatly exceeded the number of tests at the other locations. All data are from October 2023. The k values from the APT are found to be generally consistent with those directly measured on the cores. Moreover, the two sets of data display similar scatter as measured by the coefficient of variation. Overall, the APT measurements reflect the measured values and capture the variability in the results.

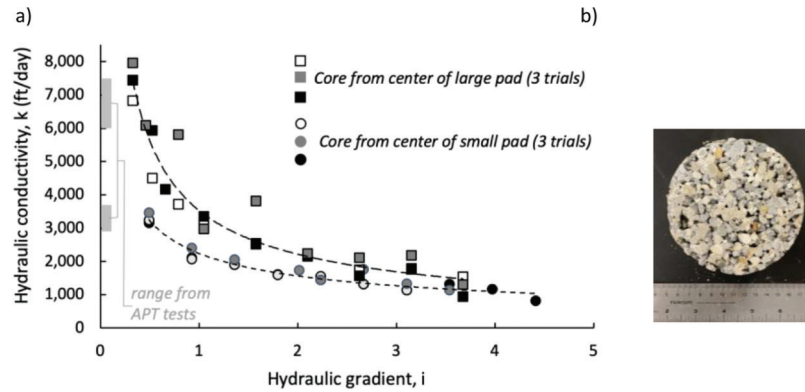


Figure 5.17 (a) Results of falling head tests on cores from center of pervious concrete pads, and (b) view of cross-section of one of the cores.

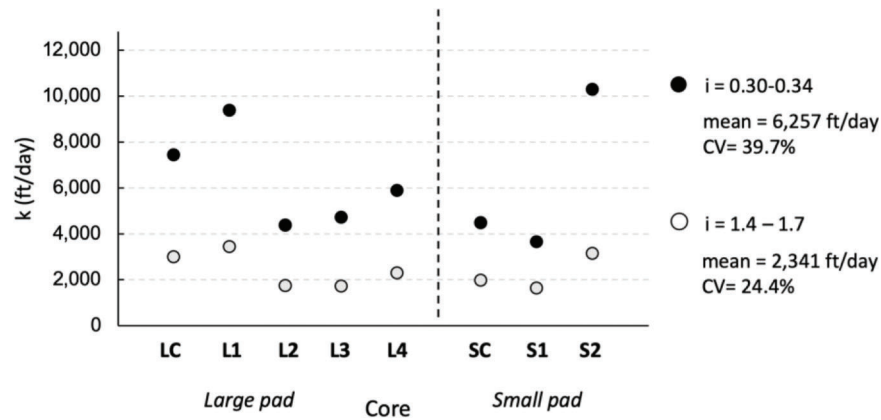


Figure 5.18 The k values from falling head tests on all cores obtained from pervious concrete pads (see core locations in Figure 5.19).

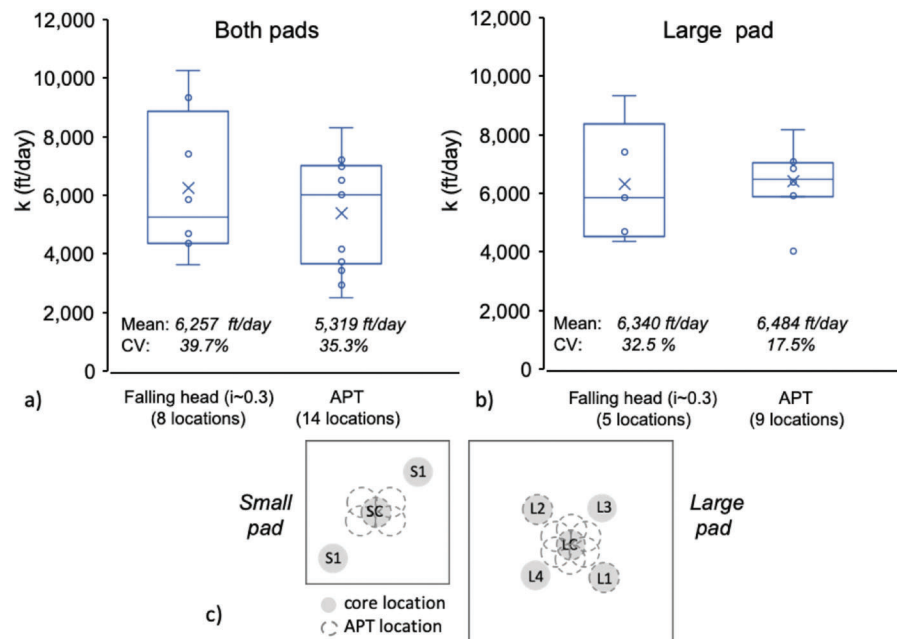


Figure 5.19 Comparison of falling head and APT k data for (a) both pads, (b) large pad only, and (c) testing locations on two pads.

6. SUMMARY AND CONCLUSIONS

6.1 Overview of Work

This research project aimed to evaluate methods for measuring performance parameters of aggregate drainage layers in-situ and provide INDOT guidance for developing performance-based specifications for these layers. The work focused on two experimental methods, the LWD and APT.

The work performed included the following.

- An extensive field-testing program presented in Chapter 3 conducted on two 60 ft × 20 ft experimental testing strips constructed at Purdue University's SBRITE facility. The strips were comprised of a coarse aggregate (IN #53) layer constructed over either the compacted natural soil, a clayey sand with ~48% fines (untreated strip) or the cement-treated subgrade (cement-treated strip). Testing on the two aggregate layers was performed with high spatial density on a 3 ft × 3 ft grid and included over 500 LWD tests with two plate sizes, ~150 APTs, imaging of the aggregate surface and measurements of the layer thickness at all grid points. In addition, over 80 nuclear density tests were performed to map variations in dry density, water content and degree of saturation of the aggregate layer across the two strips. These data also allowed correction of the APT measurements to account for the partially saturated conditions of the aggregate. Finally, over 250 LWD tests were performed on the same testing grid on the underlying subgrade layers. Following completion of the testing program, samples of the geotextile underlying a portion of the aggregate layers were exhumed and examined for damage.
- Testing at three construction sites as described in Chapter 4: the Cherry Lane extension project in West Lafayette, IN, the reconstruction of SR 46 in proximity to Bloomington, IN, and the widening of I-65 in Lebanon, IN. At all three sites LWD (two plate sizes) and APT testing focused primarily on the layer of compacted IN #53 aggregate constructed over the cement-treated subgrade, which, per INDOT specifications, was intended to function as a separator layer. These measurements were complemented by imaging of the aggregate surface at all testing points. At the Cherry Lane site additional LWD tests and APTs were performed on the overlying IN #8 layer; at the I-65 site, the testing program also included LWD tests on the cement-treated subgrade and APTs on two bound drainage layers: a cement treated base and an open graded asphalt.
- An extensive program of laboratory tests, summarized in Chapter 5, which included: APT measurements on aggregate layers compacted in large crates; APTs on pads manufactured from pervious concrete; falling head and constant head tests on compacted IN #53 aggregate. Falling head tests were performed in 4-inch and 6-inch diameter permeameters, while a custom large (12" × 12" × 36") permeameter was used for the constant head tests.

6.2 Summary and Conclusions

The trove of data collected over the course of this project provided the opportunity to do the following:

- quantify and compare spatial variability in the measured properties,

- evaluate the materials and methods used to construct the aggregate layers,
- examine the performance of the field test methods under consideration, and
- highlight some limitations in current quality assurance approaches.

The conclusions drawn from this research are presented below organized in four subsections to reflect findings in the above areas. A fifth subsection briefly summarizes additional conclusions pertaining to items that fall outside of the above categories.

6.2.1 Spatial Variability

Statistical analyses of the data collected at the SBRITE site (Section 3.4.1), enabled by the large size of the statistical sample, show that the parameters measured on the two strips exhibit different dispersion, as measured by the coefficient of variation (CV). Out of all the parameters measured at the site, LWD deflections from tests on the untreated subgrade are characterized by the greatest variability.

Of the data collected on the aggregate layers, the greatest dispersion is observed in the hydraulic conductivity (k) values (CV = 63% to 75%), followed by the LWD deflections (CV = 28% to 65%). Dry density data measured on both strips reveal the lowest CV values (3% and 4%). Similar observations are drawn from the tests performed on the aggregate layers at the three construction sites, i.e., greatest dispersion for the k data (CV = 66% to 123%), followed by LWD deflections (CV = 16% to 79%) and ρ_d (CV < 5%). At all sites the range of the k data exceeds a few thousand ft/day.

While reflecting the reduced variability that characterizes constructed materials versus natural deposits, the above CV values are generally consistent with those reported by other researchers (Amundaray, 1994).

Of significance is the reduced variability in dry density data across all sites compared to the LWD_L deflections, which suggests that factors other than the state of compaction affect the LWD_L results. This raises questions regarding the use of the LWD for verification of the state of compaction of aggregate layers, as discussed further below.

The observed spatial variability in the properties of the compacted aggregate can be, at least in part, ascribed to material heterogeneity, produced by segregation during transport and construction, which in this work was quantified through a parameter termed MFS extracted from images of the aggregate surface. For the data collected on the untreated strip at the SBRITE site (Section 3.4.2), linear correlation analyses demonstrate a strong correlation between the MFS and the in-situ hydraulic conductivity (k) (for the cement-treated strip the correlation is weaker likely due to the additional uncertainty introduced by the correction for S , see below). Data for Sites 1 and 2 follow the same trend, supporting the hypothesis that the MFS parameter is

an indicator of local material heterogeneities that drive variability in hydraulic conductivity at the local scale.

For the SBRITE untreated strip alone, the variability in the LWD deflections measured on the IN #53 aggregate surface is largely controlled by the variability in the conditions of the underlying subgrade (Section 3.4.2).

6.2.2 Materials and Construction Methods for Aggregate Layers

6.2.2.1 Subgrade treatment. Tests performed at the SBRITE site, which specifically sought to investigate the impact of the subgrade, show that, as expected, cement-treatment reduces subgrade LWD deflections (by a factor of ~ 10 relative to the measurements on the untreated subgrade). Of the 126 LWD tests performed on the cement-treated subgrade less than 5% exceed the maximum (0.31 mm) deflection required by INDOT specifications (INDOT, 2024), and the mean value is approximately 40% lower than the allowable mean deflection (0.27 mm). Cement stabilization also leads to a reduction in the deflections measured on the overlying aggregate layer (by a factor of ~ 2 relative to the measurements on the untreated strip).

In addition, the data collected on the two strips at the SBRITE site indicate that cement treatment facilitates compaction of the aggregate and, as a result, promotes more homogenous conditions. This is reflected in lower values of CV derived for LWD deflections measured not only on the subgrade but also on the overlying aggregate (two-fold reduction in CV for cement-treated strip compared to untreated strip).

6.2.2.2 Compaction procedures. Focusing on the SBRITE cement-treated strip, which more closely represents INDOT construction, the extensive program of nuclear density tests demonstrates that the procedure used to compact IN #53 (small lifts, static passes, followed by vibratory and additional static passes) allows reaching satisfactory values of relative compaction (mean value of relative compaction estimated at 97%, with only two of the 37 measurements below 95%).

LWD_L deflections measured on the aggregate surface of this strip confirm the effectiveness of the compaction procedure as the mean deflection (0.08 mm) obtained from 133 measurements falls well below the allowable value (0.27 mm) identified by INDOT specifications (INDOT, 2024), and less than 20% of the measurements exceed the maximum deflection (0.31 mm). Comparison to the LWD data collected on the aggregate layer at Sites 1–3 (all involving cement-treatment of the subgrade) demonstrates better performance of the SBRITE strip in terms of deformability (and dry density).

6.2.2.3 Suitability of IN #53 aggregate as drainage layer. Regarding the potential use of compacted IN #53 as a drainage layer, the k values measured in the field using the APT (mean values of $k = 595\text{--}3,600$ ft/

day across the sites) indicate the potential suitability of this material for exercising a drainage function. In select constant head laboratory tests, however, significantly smaller values of k were measured (less than 250 ft/day and as low as 16 ft/day) (Section 5.3.2). Sample heterogeneity, resulting from material segregation, and variation in the percentages of fines may explain these values. Laboratory tests also suggest that in materials such as IN #53 laminar conditions occur only for very small gradients ($I < 0.2\text{--}0.4$, depending on material and testing conditions). This implies that the applicability of Darcy's law to these materials is also limited to small gradients.

The hydraulic conductivity of IN #53 also depends, as expected, on the state of compaction, as demonstrated by a small number of APTs performed at the Cherry Lane site before and after compaction, and laboratory falling head tests on samples compacted at different dry densities (Section 5.3.1). However, APT measurements with concurrent imaging of the compacted aggregate surface at the testing location indicate that, once compacted, k of IN #53 is controlled by particle size, as measured by the MFS (reflected in the above-mentioned correlation), to a greater degree than by local variations in dry density. This is observed to be true across the four sites examined in this work. Differences in MFS also explain differences in the values of k measured at the different sites (Section 4.5).

The analysis of images of the surface conditions collected across all sites also indicates that IN #53 may be prone to segregation during transport, placement and compaction. While use of a spreader box for placing aggregate is generally recommended as part of best handling procedures (Getchell et al., 2020), this procedure was not adopted at any of the sites and may have contributed to exacerbating the issue. The tendency of IN #53 to segregate was also observed in the laboratory, where difficulties were encountered in achieving uniform large samples used for the in-crate APTs ($\sim 1.5\text{--}5$ ft³) and the constant head (~ 3 ft³) tests. For the constant head samples, in general, placement and compaction of the aggregate in non-dry conditions ($w \sim 8\%\text{--}9\%$) was found, at least at the lab scale, to mitigate segregation.

Likely related to the non-uniformity of the samples is the steady increase in k with continued flow under relatively small gradients (< 0.2) observed in a select number of the constant head tests, which was ascribed to internal erosion. This aspect of the performance of IN #53 requires further investigation.

6.2.3 Methods Used for Quality Control of Aggregate Layers

6.2.3.1 LWD for control of state of compaction. While both LWD deflections and nuclear density measurements are being used in practice for quality assessment of compacted subbase granular layers, across both testing strips at the SBRITE site the two measurements are not found to be strongly correlated.

Moreover, the LWD data show significantly greater dispersion than the ρ_d measurements. This reflects the fact that LWD deflections provide a composite response of the underlying layers.

For the untreated strip, measurements performed on the aggregate layer are found to be controlled by deformations in the underlying subgrade, with weak information provided on the state of compaction of the aggregate layer. Similarly, at Site 1 LWD deflections measured on the top IN #8 layer were found to be strongly correlated to those measured at the same locations on the underlying, more deformable, IN #53 subbase.

LWD tests appear, however, effective in identifying “weak” areas (see higher deflections measured in correspondence to the left side of the testing strips at Site 1, and multiple examples of weak “pockets” at all sites). Additionally, data from Site 3 shows that where values of the relative compaction from the nuclear density tests fell significantly below the requirements, this was reflected in higher LWD deflections.

6.2.3.2 APT for control of hydraulic conductivity.

Given the very limited experience with the use of the APT in the field, tests performed for evaluating of this apparatus/method had much broader scope than for the LWD. As discussed in detail in the subsections below, the following performance aspects were specifically addressed:

- ease of operation,
- suitability for testing different materials,
- impact of in-situ degree of saturation,
- repeatability and accuracy,
- effect of boundary conditions, and
- calibration.

Ease of Operation. As summarized above, testing programs with the APT were conducted at both the SBRITE experimental site and at the three construction sites, the latter allowing evaluation of the performance of the apparatus in field relevant conditions. The sturdy and compact design of the apparatus, which is mounted on a cart for easy deployment and mobility across a construction site, and the simplicity of operation are well suited for rapid and frequent measurements in the field.

Suitability for Testing Different Materials. Extensive testing at all sites investigated in this project indicates that measurements using the APT can be consistently performed on compacted IN #53 aggregate (with k in the 50 to 14,000 ft/day range) (Sections 3.4, 4.2, 4.3, and 4.4.1). Provided that the reservations discussed below are addressed, the APT can be considered worthy of consideration for measuring the hydraulic conductivity of this type of aggregate.

Based on a limited investigation conducted at Site 3 on a cement-treated permeable base (CTPB) and an open graded asphalt (OGA) layer, both with k in the 100–2,500 ft/day range, similar conclusions apply to the use of the APT for testing these materials (Section 4.4.2).

Both in the field (Cherry Lane site, Section 4.2) and in the laboratory (Section 5.2), the pressure generated by the APT apparatus was often insufficient to perform measurements on materials such as IN #8 characterized by much higher saturated hydraulic conductivity. As a result, it is concluded that in its current configuration, the APT cannot be reliably used to test materials with $k > 15,000$ ft/day.

Impact of In-Situ Degree of Saturation. As a reminder, the APT does not directly measure the hydraulic conductivity of the tested medium. Rather, it measures the flux of gas in a material that is partially saturated with water. Calculation of the equivalent hydraulic conductivity corresponding to full saturated conditions requires calculation of the relative permeability to gas. Values of saturated hydraulic conductivity derived from the APT are highly sensitive to the degree of saturation of the aggregate. Correction of the raw data to account for partially saturated conditions is based on the Brooks and Corey (1964) relationship and requires input of values of the pore size distribution index (λ), the residual water saturation (S_r) and the degree of saturation (S) of the tested material. The correction becomes significant for S greater than ~ 0.35 , and for $S > 0.60$ can lead to an order of magnitude increase in k . At the SBRITE site, where nuclear density measurements were performed with high spatial density, despite the controlled conditions (same aggregate stockpile and equipment, single-day construction for each of the strips, consistent compaction procedures), the degree of saturation varied significantly ($S = 0.28$ – 0.45 and 0.36 – 0.76 across the untreated and cement-treated strip, respectively, with $CV > 20\%$ – 28%). Under these conditions, which are not unusual. White and Vennapusa (2014) report that for granular pavement base materials, on average, S ranges between 16% and 62%), correction for the in-situ degree of saturation leads to an increase in the value of k by more than one order of magnitude at locations with S greater than ~ 0.65 (Section 3.4.1).

Further evidence of the importance of correctly accounting for the in-situ degree of saturation is provided by the results of tests performed on compacted IN #53 at 29 locations on the SBRITE strips over a period of 4 months (Section 3.4.5). At 20 of these locations, the range of the uncorrected values of k exceeded 350 ft/day, and was as high as 1,103 ft/day, reflecting changes in S occurring over that period because of weather patterns. It is concluded that when using the APT, concurrent measurements of the degree of saturation are therefore needed to map spatial variability of the in-situ degree of saturation. In absence of these measurements, the APT can provide, at best, lower bound estimates of k , which, however, may be off from actual values by over an order of magnitude.

Related to the correction for the degree of saturation, it is observed that, even after applying the recommended procedure (White et al., 2007, 2014) for deriving the saturated hydraulic conductivity from APT measurements, the results are still not statistically

independent from the in-situ degree of saturation, as they should be (Section 3.4.2). This suggests that the procedure for correcting the measurement for the in-situ degree of saturation requires improvement.

Repeatability and Accuracy. The repeatability of the APT was examined through field measurements on compacted IN #53 (SBRITE site, Section 3.4.5) and bound drainage layers (Site 3, Section 3.4.7), by performing repeat measurements at the same location point in rapid sequence (i.e., with no change in the environmental conditions and/or in the state of the material), both keeping the device stationary, and lifting and repositioning it, carefully targeting the same testing point. The first set of tests, which were intended to measure the inherent repeatability of the test yielded measurements generally within 25–50 ft/day, with values of the coefficient of variation (CV) less than 3%, and in most cases less than 1%. The second set of tests produced coefficients of variation as large as 14% and ranges (maximum - minimum value of a string of measurements) in most cases between 200 and 600 ft/day. This increased scatter is thought to reflect slight differences in the manner the pad and the APT device are positioned and local (<1-inch radius) material variability. Similar values of CV were derived from repeat tests performed in the lab following the same two procedures on pads of pervious concrete with k between 2,500 and 10,000 ft/day (Section 5.4.1).

Due to observed variability in the hydraulic conductivity of samples of compacted aggregate, the accuracy of the APT was evaluated through a testing program on pervious concrete (Section 5.4.3) that included: APTs at different locations on two 4" thick concrete pads (2' × 2' and 1.4' × 1.4' in cross section) and falling head tests on eight cores obtained from the pads after completion of the APTs. While the selection of this manufactured model material was intended to reduce the effects of material variability, k values from the falling head tests vary from core to core by a factor of 2 to 3 (depending on the gradient) (e.g., for $I = 0.30$ – 0.34 , $k = 3,633$ – $10,263$ ft/day) and APT tests performed on the pads in close proximity to each other also show evidence of significant local variability (with differences of up to 2,000 ft/day for measurements performed just a few inches apart). In addition, exact correspondence between the results of the two tests cannot be expected because of the different flow conditions (gradient and geometry), and the fact that the APT measurement is affected by the characteristics of a much larger volume of material. Nevertheless, values of k values derived from the APTs are generally consistent with those measured under low gradients (≤ 0.3) on the cores. Moreover, the two sets of data display similar scatter as measured by the coefficient of variation. Overall, it can be concluded that the APT measurements reflect the values of k obtained from direct measurements on the pervious concrete pads and capture the variability in the results.

The above discussed difficulties in preparing uniform and repeatable samples did not allow quantifying the

sensitivity of the APT. However, measurements performed pre and post compaction both in the field (Site 1, Section 4.2) and in the lab (in-crate samples, Section 5.2) on IN #53 aggregate demonstrate the capability of the APT to capture the reduction in k (by a few hundred ft/day or more) associated with the transition from loose to dense conditions.

The observed relationship between the value of k derived in the field using the APT and the MFS represents an additional indication of the sensitivity of the test.

Effect of Bottom Boundary. As the project sought to explore the deployment of the APT on multi-layer systems (e.g., drainage layer over subbase), the effect of the bottom boundary condition was explored through a program of APTs on 4" thick pervious concrete pads (Section 5.4.2). Measurements were performed with the pad lifted on blocks (open bottom boundary representing infinitely permeable layer), resting on an impermeable foam layer and after treatment of the bottom surface of the pad with a spray foam. The data from the last two sets of measurements are found to be statistically different from the first, with higher values of k measured with the pad in the lifted position. This indicates that the bottom boundary may affect APT measurements performed on layers as thick as 4".

Calibration. In the first stage of this project consistent differences were observed between the values of k derived from measurements performed with orifices B and C of the APT. This issue was eventually attributed to erroneous factory calibration of orifice C (Section 4.3), and a procedure for in-house calibration and/or verification was developed and is presented in this report (Section 2.2.3.3). With appropriate calibration, the results are found to be independent of the orifice.

6.2.4 Quality Assurance

Stochastic analysis of the LWD_L data collected at the SBRITE experimental site on both the subgrade and the aggregate layer demonstrates that statistically small samples are generally not reliable for quality control, and that the estimate of the population mean based on such samples carries great uncertainty. The degree of uncertainty is dependent on the distribution of the population, and increases for datasets characterized by greater variability (higher CV) (Section 3.4.3).

Moreover, data collected at all sites clearly demonstrates that information pertaining to local problematic areas, which are often the source of damage in pavement systems, is not captured when utilizing QA/QC criteria based on the mean of a sample, compromising efforts invested in quality assessment. These observations highlight the importance during a quality assessment campaign of assessing uncertainty evidenced by the dispersion in the data. In practice this would require investing in rapid non-destructive tests that can be performed in large number and at high spatial density, and formulating guidelines in probabilistic

terms (e.g., by placing a parameter-dependent limit on the coefficient of variation).

Finally, the observed variability in the measured values of k and the repeatability of the APT do not support the implementation of excessively stringent criteria for hydraulic conductivity.

6.2.5 Additional Conclusions

6.2.5.1 Geotextile performance. While beyond the original scope of the research project, samples of the nonwoven geotextile fabric used as a separator layer over a portion of the two SBRITE strips were exhumed following the completion of the testing program (including additional cyclic tests part of project SPR-4547). Analysis of the samples (Section 3.4.6) allows evaluating the performance of the fabric (which meets Class 2 survivability requirements based on (Holtz et al., 2008) and qualifies as a Type 2A geotextile per INDOT 918.02(b)). Given the level of damage, in the form of bursts, perforations and abrasion, observed on the exhumed samples, it is concluded that the geotextile did not survive and could, therefore, not fulfill its intended functions as separator/filter.

6.2.5.2 Compaction vibratory effects. The experimental program performed at the SBRITE site also included measurements, by means of earth pressure cells embedded in the cement-treated subgrade immediately under the aggregate layer, of the stresses generated by a CAT CS44B smooth drum roller compactor during both static and vibratory passes at maximum centrifugal force (with $f = 30$ Hz) (Section 3.4.7). Analysis of these measurements yielded a value of the force ratio (FR) equal to 3.1. The FR can be used to account for compactor vibratory effects through an equivalent static force when evaluating the stability of granular layers during compaction (Getchell et al., 2020). While the above value applies specifically to this compactor, the instrumentation and procedure can be readily applied to measure values of the force ratio for other compactors.

6.2.5.3 Hydraulic conductivity of cement-treated permeable base and open graded asphalt. As discussed above, a program of APTs was performed at Site 3 on two bound layers: a cement-treated permeable base (CTPB) and an open-graded asphalt (OGA) layer (Section 4.4.2). This was the first INDOT site where these materials were used as drainage layers.

The APTs yielded k values of 85–2,027 ft/day (CTPB) and 394–2,455 ft/day (OGA) (all derived assuming $S = 0$), of the same order of those measured on the compacted IN #53 aggregate. These values indicate the potential suitability of these materials, as constructed at Site 3; to function as drainage layers (this conclusion cannot be extended to other mix-designs/compositions).

6.3 Recommendations

Based on the work performed, the following recommendations for implementation are provided.

6.3.1 Construction Procedures

- Under conditions similar to those encountered at the SBRITE site, cement-treatment of the subgrade is recommended to obtain better performance in terms of reduced LWD deflections and less variable conditions. The results from the S-BRITE site also suggest that the presence of the stiffer cement treated layer promotes more effective compaction of the overlying aggregate.
- Compaction of aggregates in the field should be performed using vibratory rollers, which provide the most effective compaction, with early and final passes in static mode.
- This project also reinforces previous recommendations provided as part of SPR-4116 (Getchell et al., 2020) pertaining to the importance of controlling material segregation during placement and compaction of the aggregate. Therefore, construction methods to limit segregation of the aggregates in the field should be enforced.
- A higher-class geotextile product compared to the one used in this project is recommended for use between subgrade and aggregate to provide separation and filtration functions.

6.3.2 Testing Methods for In-Situ Control of Aggregate Layers

- Based on previous research (Pajo et al., 2023), deflection-based criteria are recommended when using the LWD for QA/QC.
- The use of the LWD is recommended for testing aggregate layers constructed on cement-treated subgrade to quantify compressibility and homogeneity, the latter provided that the number of tests performed is sufficient to map spatial variability.
- The use of the LWD is also recommended for QA/QC of both untreated and cement-treated subgrades.
- The LWD is not recommended for QA/QC of aggregate layers constructed on untreated subgrades given the interference on the surface deflections by the deformation of the underlying subgrade.
- In the current state of development of the test and its method of interpretation for deriving the saturated hydraulic conductivity, the APT cannot be implemented to provide reliable results with sufficient accuracy. An additional hurdle to the practical implementation is the requirement of extensive joint testing for mapping the degree of saturation of the whole section of material that is under consideration. The two series of tests (nuclear probe for degree of saturation and APT for permeability) would have to be performed according to a very tight schedule so that there is no time for the degree of saturation to change during the process.
- Because of the potential interference of the bottom boundary, the test is questionable when performed on relatively thin aggregate layers and the underlying layer or subgrade is permeable.

6.3.3 QA/QC of Aggregate Layers

- As this work has shown that small statistical samples are generally not reliable for quality control, the use of rapid non-destructive tests (e.g., LWD) that can be performed in large number and at high spatial density is recommended. These may be complemented by more sophisticated field or laboratory tests against which they can be calibrated.
- Moreover, because information pertaining to local problematic areas is not captured when utilizing QA/QC criteria based solely on the mean value of a statistical sample, assessing uncertainty as measured by the dispersion of the data should be a key element of any QA/QC campaign.
- QA/QC guidelines should be reformulated in probabilistic terms (e.g., by placing a parameter-dependent limit on the coefficient of variation), while defining context-dependent acceptable risk levels that consider economic, environmental and user-related consequences of failure and/or miss-assessment of the quality of work.
- Consideration should be given to assessing material segregation as part of a QA/QC protocol. In this case, a quantitative criterion, for example based on imaging of the aggregate surface (see below), should be identified.

The study also highlighted areas where *additional research* is warranted, as summarized below.

6.3.4 Improvement in Data Interpretation and Further Validation of the Air Permeameter Test

Conversion of gas flow through the partially saturated material, measured by the APT, to a value of the saturated hydraulic conductivity requires accounting for the in-situ degree of saturation. In the approach put forth by the developers of the APT (White et al., 2007, 2014) this correction relies on the work by Brooks and Corey (1964). However, analysis of the SBRITE data using this approach (Section 3.4.2) shows that this procedure may require improvement. It is recommended that future research examine other, more advanced models (e.g., the one by Van Genuchten, 1980). The extensive data collected as part of this project can be readily used for model evaluation, recognizing that model selection will ultimately depend not only on performance but also on implementation requirements (e.g., number of parameters and tests needed for their determination).

An additional aspect of APT interpretation that requires further verification is the effect of the bottom boundary condition. Future work should explore the impact of the presence of bottom layers of different permeability using both experiments and numerical modeling.

Finally, further validation of the accuracy and sensitivity of the test is required. Given the challenges with preparing large uniform aggregate samples, various reference materials covering a broad range of k values should be tested to supplement the data

collected in this project on pervious concrete. Preliminary tests suggest permeable low-density cellular concrete as a potential reference material.

6.3.5 Advancement of LWD Test Interpretation

While in this project the analysis of the LWD data focused exclusively on measured deflections, in practice, a value of the modulus is commonly derived assuming static loading conditions and using the theory for a rigid plate on a homogeneous, isotropic, linear-elastic half-space. However, several studies (e.g., Mooney & Miller, 2009) highlight that this approach leads to unrealistic values of the modulus. Better interpretation of the LWD as a dynamic test would provide the opportunity to derive fundamental constitutive material parameters (e.g., see the derivation of the low strain modulus from LWD-induced seismic analysis in the work by (Ryden & Mooney, 2009) and should be the focus of future research.

6.3.6 Further Investigation of IN #53 (and/or Other Candidate Aggregates)

Based on the work performed for this research, the susceptibility of IN #53 to segregation during transport, placement and compaction and to internal erosion under even relatively small hydraulic gradients requires further study. It is recommended that investigation of both issues be approached combining experiments and advanced numerical methods. In particular, the Discrete Element Method (DEM) has shown great promise for studying these processes (e.g., see O'Sullivan, 2014). Such a study, which may be extended to other candidate aggregates, will allow defining gradations and construction procedures that minimize segregation and guarantee internal stability.

6.3.7 Advancement of Image Analysis Method for Segregation Quality Control

The image processing routine employed in this project for the characterization of coarse aggregate layers provided the means to map and quantify material variability. There is an opportunity by building on this work to develop a quality control method for evaluating segregation of aggregate layers in the field. Key necessary advances include: improving the algorithm and the code, with specific focus on updating the segmentation routine; extending the code to process data from video scans instead of still images (for rapid image collection from a moving vehicle); calibrating the method in the laboratory with reference materials to establish accuracy, repeatability, and the effect of other parameters, such as lighting, wetness, and aggregate color; further validating the method in the field at INDOT construction sites.

6.3.8 Development of Risk-Informed QA/QC

A more general question raised by this study is that of the potential risk resulting from insufficient or inadequate QA/QC. The notion of risk represents, in this context, the expected monetary or economic consequence of incorrectly assessing the constructed aggregate layers quality and is defined by the probability of incorrect assessment multiplied by quantified consequences of the error. A primary step while envisioning probability-based QA/QC protocols would be to decide on the level of acceptable risk.

REFERENCES

- AASHTO. (2015). *Mechanistic-empirical pavement design guide: A manual of practice*, 2nd ed. American Association of State Highway and Transportation Officials. <https://www.standards-global.com/wp-content/uploads/pdfs/preview/1900604>
- ACPA. (2007). *Subgrades and subbases for concrete pavements* (Engineering Bulletin EB204P). American Concrete Pavement Association. <https://www.cement.org/docs/default-source/cement-concrete-applications/eb204p-subgrades-and-subbases-for-concrete-pavements.pdf>
- ACPA. (2010). *Subbase specification trends* (Concrete Pavement Technology Series TS204.12P). American Concrete Pavement Association. <https://www.acpa.org/download/1130/information-sheet/22369/subbase-specification-trends.pdf>
- Akoglu, H. (2018). User's guide to correlation coefficients. *Turkish Journal of Emergency Medicine*, 18(3), 91–93.
- Amundaray, J. I. (1994). *Modeling geotechnical uncertainty by bootstrap resampling* [Doctoral dissertation, Purdue University]. <https://docs.lib.purdue.edu/dissertations/AA19512923/>
- Andrei, D. (1999). *Development of a harmonized test protocol for the resilient modulus of unbound materials used in pavement design* [Master's Thesis, University of Maryland–College Park].
- Applied Research Associates, Inc. (2014). *Drainage requirements in pavements (DRIP 2.0)*. [Computer software]. <https://me-design.com/MEDesign/DRIP.html?AspxAutoDetectCookieSupport51>
- Bourdeau, P. L., & Amundaray, J. I. (2005). Non-parametric simulation of geotechnical variability. *Géotechnique*, 55(2), 95–108.
- Briaud, J.-L. (2013). *Geotechnical engineering: Unsaturated and saturated soils*. John Wiley & Sons, Inc.
- Brooks, R. H., & Corey, A. T. (1964, March). *Hydraulic properties of porous media* (Hydrology Paper No. 3). Colorado State University. https://wipp.energy.gov/library/cra/2009_cra/references/Others/Brooks_Corey_1964_Hydraulic_Properties_ERMS241117.pdf
- Chou, Y.-L. (1969). *Statistical analysis, with business and economic applications*. Holt, Rinehart & Winston, Inc.
- Clyne, T. R., Voller, V. R., & Birgisson, B. (2001). *Evaluation of a field permeameter to measure saturated hydraulic conductivity of base/subgrade materials* (MN/RC-2001-19). Minnesota Department of Transportation.
- Doyle, G. (2003, August). *Major types of transportation construction specifications: A guideline to understanding their evolution and application*. American Association of State Highway and Transportation Officials.
- Efron, B. (1979a). Bootstrap methods: Another look at the jackknife. *The Annals Statistics*, 7(1), 1–26.
- Efron, B. (1979b). Computers and the theory of statistics: Thinking the unthinkable. *SIAM Review*, 21(4), 460–480.
- Fannin, R. J., & Moffat, R. (2006). Observations on internal stability of cohesionless soils. *Géotechnique*, 56(7), 497–500.
- Fredlund, D. G., Rahardjo, H., & Fredlund, M. D. (2012). *Unsaturated soil mechanics in engineering practice*. John Wiley & Sons, Inc.
- Garzon-Sabogal, L. E., Bourdeau, P. L., & Santagata, M. (2024). Grain portraits: Quantifying heterogeneity of aggregate layers through image analysis. In *Geo-Congress 2024* (pp. 329–339).
- Getchell, A., Garzon Sabogal, L., Bourdeau, P. L., & Santagata, M. (2020). *Investigation of design alternatives for the subbase of concrete pavements* (Joint Transportation Research Program Publication No. FHWA/IN/JTRP-2020/03). West Lafayette, IN: Purdue University. <https://doi.org/10.5703/1288284317114>
- Goggin, D. J., Thrasher, R. L., & Lake, W. L. (1988). A theoretical and experimental analysis of minipermeameter response including gas slippage and high velocity flow effects. *In Situ*, 12(1–2), 79–116.
- Gupta, S., Singh, A., & Ranaivoson, A. (2004, December). *Moisture retention characteristics of base and sub-base materials* (Report No. MN/RC-2005-06). Minnesota Department of Transportation.
- Hardin, B. O., & Black, W. L. (1966). Sand stiffness under various triaxial stresses. *Journal of the Soil Mechanics and Foundations Division*, 92(2), 27–42.
- Hardin, B. O., & Drnevich, V. P. (1972a). Shear modulus and damping in soils: Design equations and curves. *Journal of the Soil mechanics and Foundations Division*, 98(7), 667–692.
- Hardin, B. O., & Drnevich, V. P. (1972b). Shear modulus and damping in soils: Measurement and parameter effects. *Journal of the Soil Mechanics and Foundations Division*, 98(6), 603–624.
- Hein, D., Rao, S., Tayabji, S. D., & Lee, H. (2017). *Bases and subbases for concrete pavements* (Tech Brief No. FHWA-HIF-16-005). Federal Highway Administration.
- Hilf, J. W. (1991). Compacted fill. In H.-Y. Fang (Ed.), *Foundation Engineering Handbook* (pp. 249–316). Chapman & Hall.
- Holtz, R. D., Christopher, B. R., & Berg, R. R. (2008). *Geosynthetic design and construction guidelines: Reference manual* (Publication No. FHWA NHI-07-092). Federal Highway Administration.
- INDOT. (2013). *Design procedures for soil modification or stabilization*. Indiana Department of Transportation.
- INDOT. (2020, November 5). *Test sections for aggregates and recycled materials: ITM No. 514-20*. Indiana Department of Transportation Division of Materials and Tests. https://www.in.gov/indot/doing-business-with-indot/files/514_testing.pdf
- INDOT. (2024). *Indiana Department of Transportation standard specifications 2024*. Indiana Department of Transportation. <https://www.in.gov/dot/div/contracts/standards/book/sep23/2024%20Standard%20Specifications.pdf>
- INDOT. (2025, May 9). *Field determination of deflection using light weight deflectometer: ITM No. 508-19*. Indiana Department of Transportation Division of Materials and Tests.
- Jones, H. A., & Jones, R. H. (1989). Horizontal permeability of compacted aggregates. In R. H. Jones and A. R. Dawson (Eds.), *Proceedings of the 3rd International Symposium on*

- Unbound Aggregates in Roads* (pp. 70–77). Butterworths Scientific.
- Lamarre, M., Townshend, B., & Shah, H. C. (1992). Application of the bootstrap method to quantify uncertainty in seismic hazard estimates. *Bulletin of the Seismological Society of America*, 82(1), 104–119.
- Léger, C., Politis, D. N., & Romano, J. P. (1992). Bootstrap technology and applications. *Technometrics*, 34(4), 378–398.
- Li, C., Ashlock, J., White, D., & Vennapusa, P. (2017). Permeability and stiffness assessment of paved and unpaved roads with geocomposite drainage layers. *Applied Sciences*, 7(7), 718.
- Mitchell, J. K., & Soga, J. (2005, May). *Fundamentals of soil behavior, Third edition*. John Wiley & Sons Inc.
- Mooney, M. A., & Miller, P. K. (2009). Analysis of lightweight deflectometer test based on in situ stress and strain response. *Journal of Geotechnical and Geoenvironmental Engineering*, 135(2), 199–208.
- Moulton, L. K. (1980, August; reprinted, July 1990). *Highway subdrainage design* (Report No. FHWA-TS-80-224c). Federal Highway Administration.
- Ng, C. W. W., & Menzies, B. (2007). *Advanced unsaturated soil mechanics and engineering (1st ed.)*. CRC Press.
- O’Sullivan, C. (2014). Advancing geomechanics using DEM. In K. Kumar, K. Biscontin, G. Kuo, & M. Soga (Eds.), *Geomechanics from Micro to Macro Proceedings - IS-Cambridge, I*, 21–32. CRC Press.
- Oztoprak, S., & Bolton, M. D. (2013). Stiffness of sands through a laboratory test database. *Géotechnique*, 63(1), 54–70.
- Patriot Engineering and Environmental, Inc. (2014). *Report of geotechnical engineering investigation* (Patriot Project No. 6-14-0015). Purdue University.
- Pajo, B., Becker, P. J., Bourdeau, P. L., & Santagata, M. (2023). *Data interpretation of automated plate load test (APLT) for real-time in situ determination of unbound layer resilient modulus* (Joint Transportation Research Program Publication No. FHWA/IN/JTRP-2023/22). West Lafayette, IN: Purdue University. <https://doi.org/10.5703/1288284317653>
- Randolph, B., Cai, J., Heydinger, A., & Gupta, J. (1996). Laboratory study of hydraulic conductivity for coarse aggregate bases. *Transportation Research Record: Journal of the Transportation Research Board*, 1519(1), 19–27. <https://doi.org/10.1177/0361198196151900103>
- Ryden, N., & Mooney, M. A. (2009). Analysis of surface waves from the light weight deflectometer. *Soil Dynamics and Earthquake Engineering*, 29(7), 1134–1142.
- Van Genuchten, M. T. (1980). A closed-form equation for predicting the hydraulic conductivity of unsaturated soils. *Soil Science Society of America Journal*, 44(5), 892–898.
- Vennapusa, P. K. R., & White, D. J. (2015). Field assessment of a jointed concrete pavement foundation treated with injected polyurethane expandable foam. *International Journal of Pavement Engineering*, 16(10), 906–918.
- White, D. J., Vennapusa, P. K., Suleiman, M. T., & Jahren, C. T. (2007). An in-situ device for rapid determination of permeability for granular bases. *Geotechnical Testing Journal*, 30(4), 282–291.
- White, D., Vennapusa, P., Becker, P., Rodriguez, J., Zhang, Y., & White, C. (2018). *Central Iowa Expo pavement test sections: Pavement and foundation construction testing and performance monitoring* (IHRB Project TR-671). Iowa State University Center for Earthworks Engineering Research.
- White, D. J., Vennapusa, P., & Zhao, L. (2014). Verification and repeatability analysis for the in situ air permeameter test. *Geotechnical Testing Journal*, 37(2), 365–376.
- Witczak, M. W. (2004). *Harmonized test methods for laboratory determination of resilient modulus for flexible pavement design*. The University of Maryland – College Park.
- Xiao, Y., Tutumluer, E., & Moaveni, M. I. (2013). In-situ hydraulic properties of unbound aggregate layers measured using gas permeameter test (GPT) device. *Airfield and Highway Pavement 2013: Sustainable and Efficient Pavements* (pp. 1370–1385).

APPENDICES

Appendix A. Data Sheet for Geotextile Used at SBRITE Site

Appendix B. Plots for Correlation Analyses of SBRITE Data

Appendix C. Photos Documenting Geotextile Damage

APPENDIX A. DATA SHEET FOR GEOTEXTILE USED AT SBRITE SITE



Product Data

GEOTEX® 601

GEOTEX® 601 is a polypropylene, staple fiber, needle-punched nonwoven geotextile produced by Propex, and will meet the following Minimum Average Roll Values (MARV) when tested in accordance with the methods listed below. The fibers are needled to form a stable network that retains dimensional stability relative to each other. The geotextile is resistant to ultraviolet degradation and to biological and chemical environments normally found in soils.

GEOTEX® 601 conforms to the property values listed below¹. Propex performs internal Manufacturing Quality Control (MQC) tests that have been accredited by the Geosynthetic Accreditation Institute – Laboratory Accreditation Program (GAI-LAP). This product is NTPEP tested for AASHTO standards.

MARV ²			
PROPERTY	TEST METHOD	ENGLISH	METRIC
ORIGIN OF MATERIALS			
% U.S. Manufactured		100%	100%
MECHANICAL			
Grab Tensile Strength	ASTM D-4632	160 lbs	712 N
Grab Elongation	ASTM D-4632	50%	50%
CBR Puncture	ASTM D-6241	410 lbs	1824 N
Trapezoidal Tear	ASTM D-4533	60 lbs	267 N
ENDURANCE			
UV Resistance at 500 hrs	ASTM D-4355	70%	70%
HYDRAULIC			
Apparent Opening Size (AOS) ³	ASTM D-4751	70 US Std. Sieve	0.212 mm
Permittivity	ASTM D-4491	1.5 sec ⁻¹	1.5 sec ⁻¹
Water Flow Rate	ASTM D-4491	110 gpm/ft ²	4482 l/min/m ²
ROLL SIZES ⁴			
		12.5 ft x 360 ft	3.81 m x 109.8 m
		15 ft x 300 ft	4.57 m x 91.5 m

NOTES:

1. The property values listed above are effective 12/17/2018 and are subject to change without notice.
2. Values shown are in weaker principal direction. Minimum average roll values (MARV) are calculated as the typical minus two standard deviations. Statistically, it yields a 97.7% degree of confidence that any samples taken from quality assurance testing will exceed the value reported. Values represent testing at time of manufacture.
3. Maximum average roll value.
4. Contact your local Territory Business Manager (TBM) for custom widths and colors. Lead times may vary depending on customer requirements and volume requested.



ENGINEERED EARTH SOLUTIONS™

www.propexglobal.com

Propex Operating Company, LLC • 4019 Industry Drive Chattanooga, TN 37416 • ph 800 621 1273 • ph 423 855 1466

ARMORMAX®, PYRAMAT®, LANDLOK®, X3®, PYRAMALL®, SCOURLOK®, GEOTEX®, PETROMAT®, PETROTAC®, REFLECTEX®, and GRIDPRO™ are registered trademarks of Propex Operating Company, LLC.

This publication should not be construed as engineering advice. While information contained in this publication is accurate to the best of our knowledge, Propex does not warrant its accuracy or completeness. The ultimate customer end user of the products should assume sole responsibility for the final determination of the suitability of the information and the products for the contemplated and actual use. The only warranty made by Propex for its products is set forth in our product data sheets for the product, or such other written warranty as may be agreed by Propex and individual customers. Propex specifically disclaims all other warranties, express or implied, including without limitation, warranties of merchantability or fitness for a particular purpose, or arising from provision of samples, a course of dealing or usage of trade.

© 2019 Propex Operating Company, LLC

Figure A.1 Datasheet for Geotex 601 nonwoven geotextile.

APPENDIX B. PLOTS FOR CORRELATION ANALYSES OF SBRITE DATA

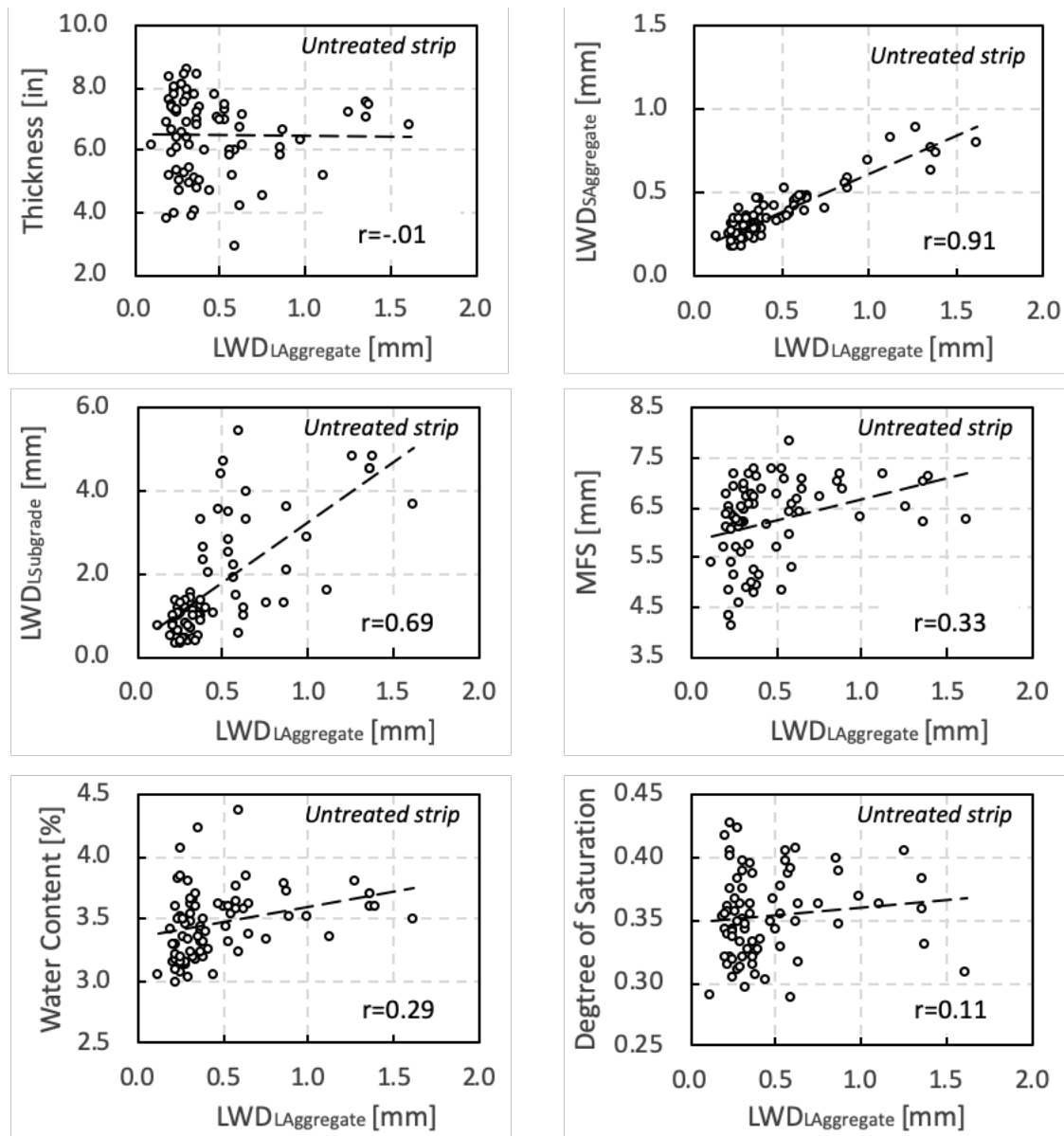


Figure B.1 Plots for untreated strip.

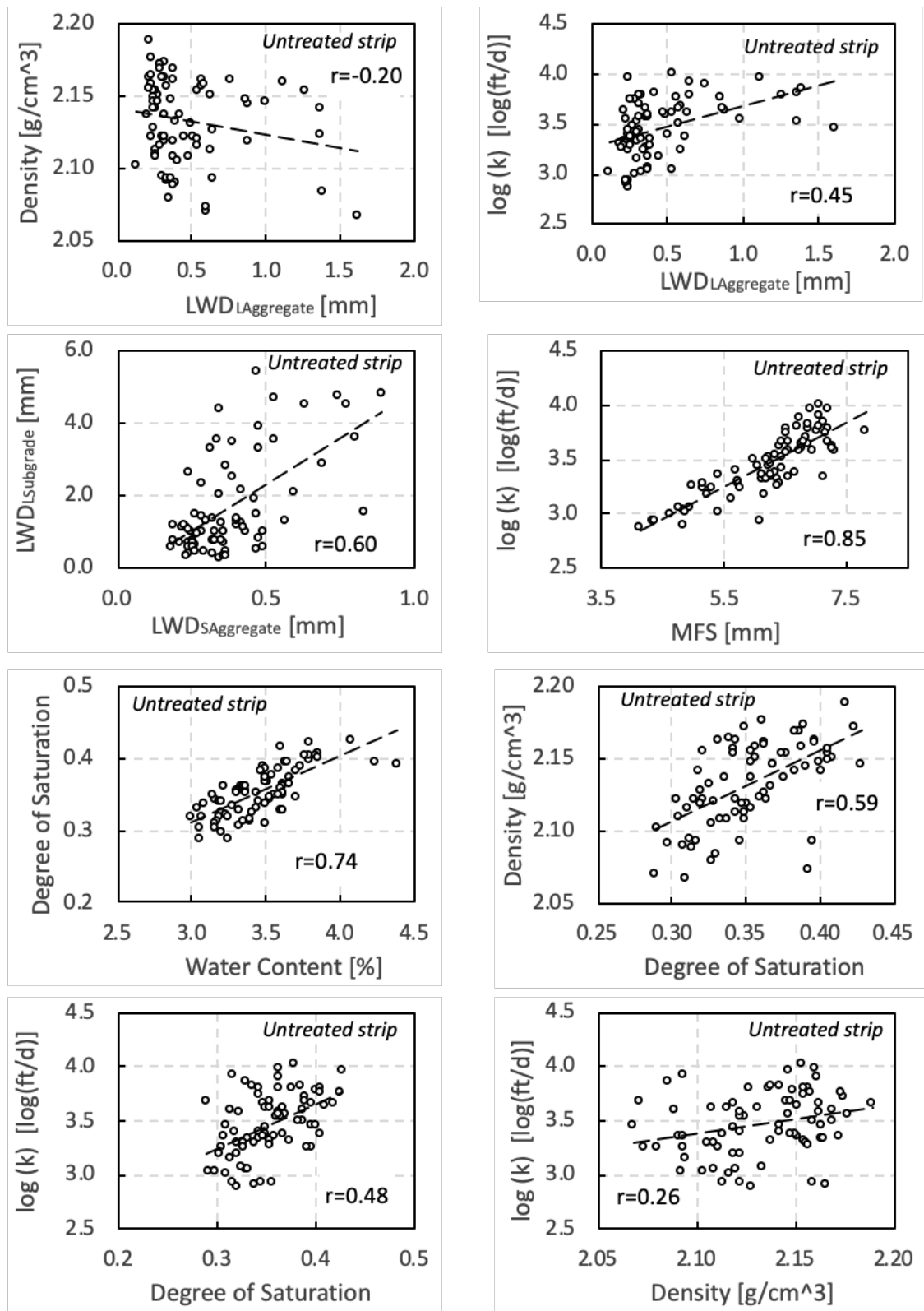


Figure B.1 (cont.) Plots for untreated strip.

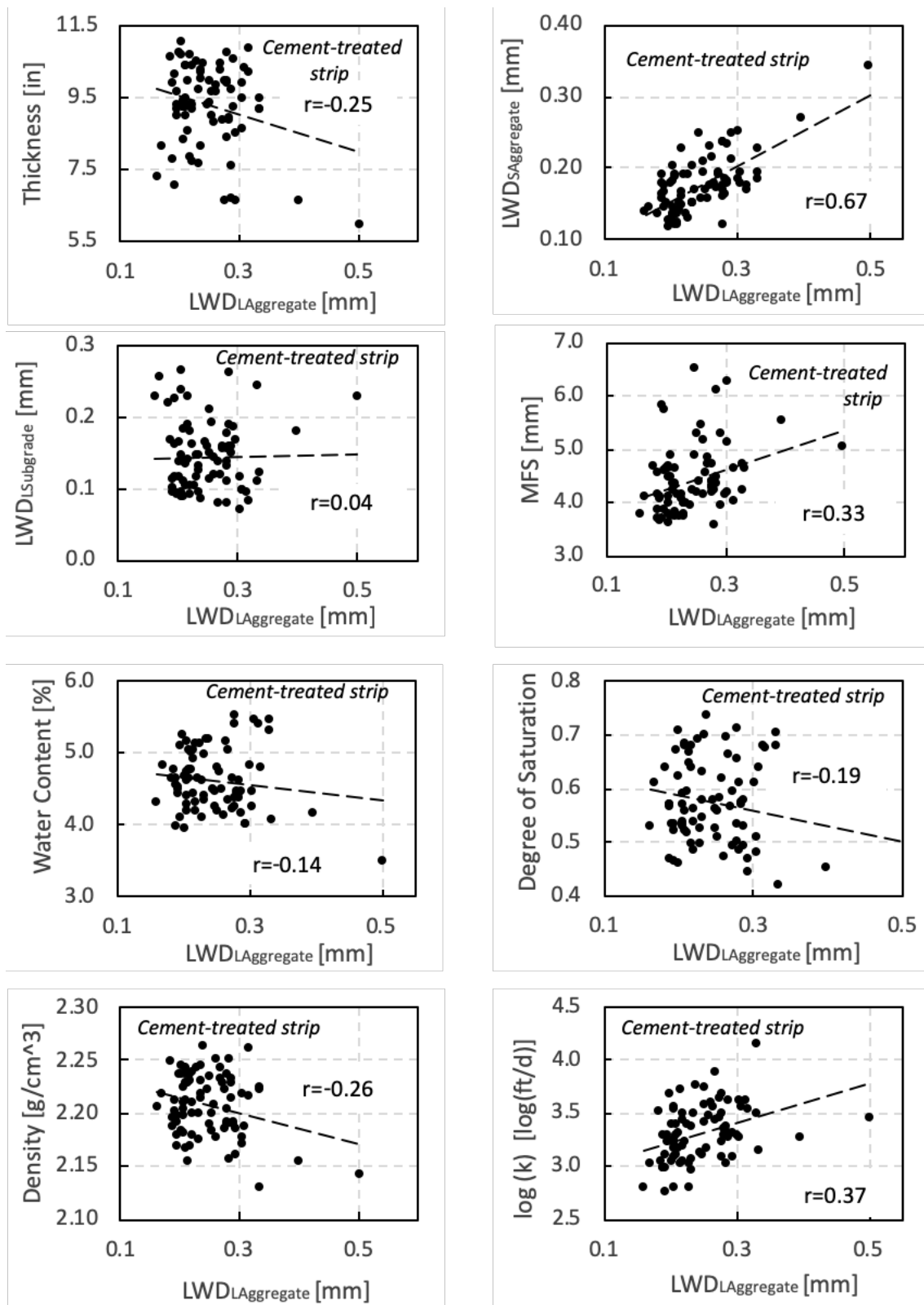


Figure B.2 Plots for cement-treated strip.

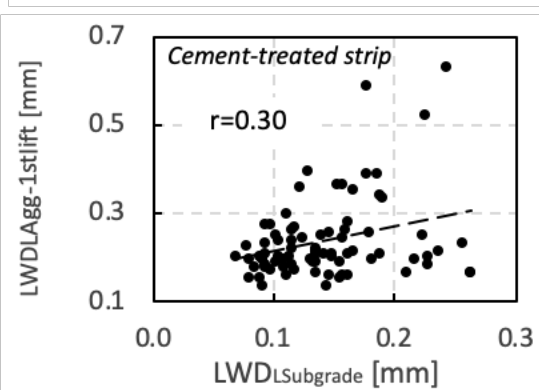
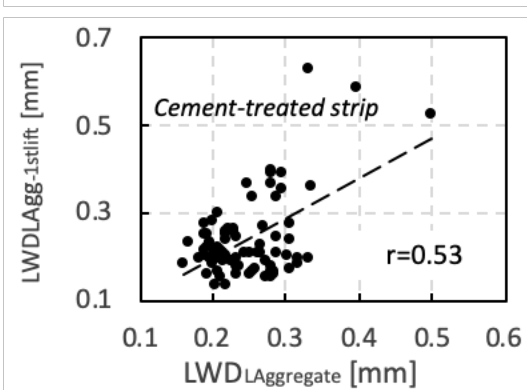
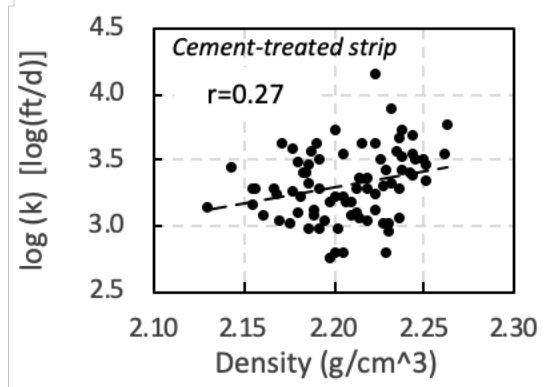
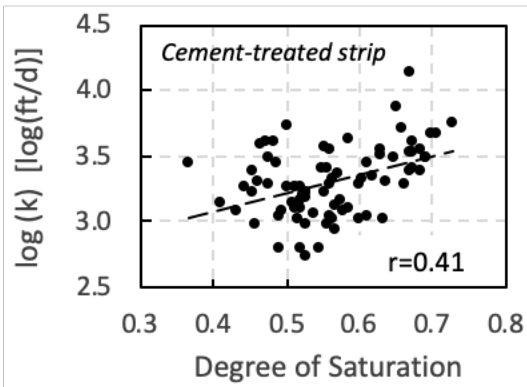
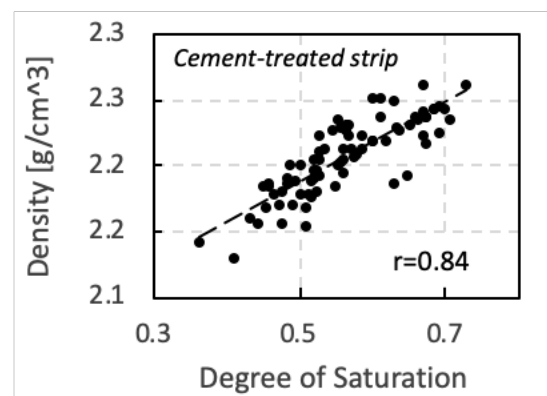
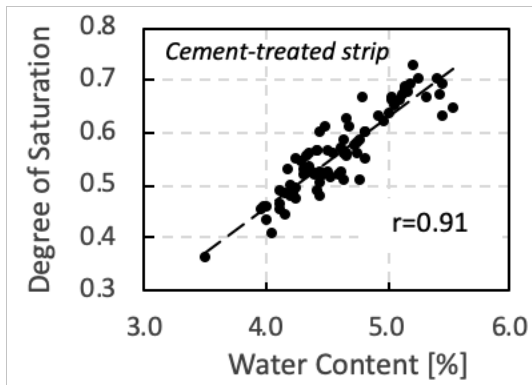
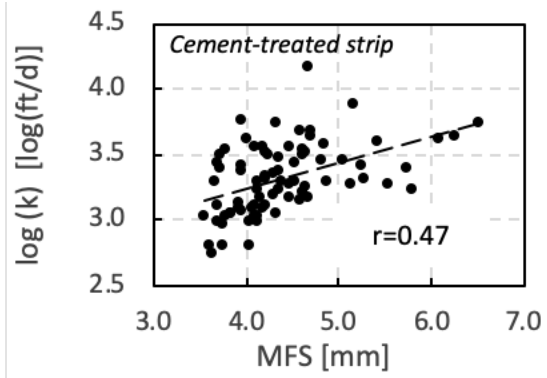
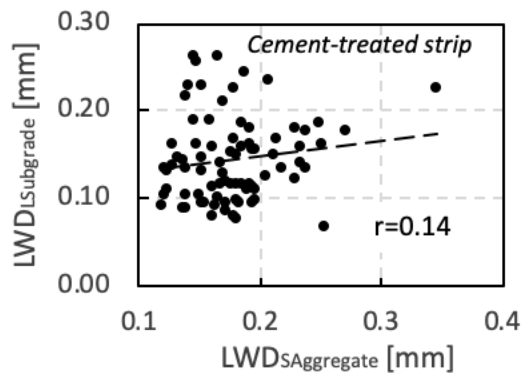


Figure B.2 (cont.) Plots for cement-treated strip.

APPENDIX C. PHOTOS DOCUMENTING GEOTEXTILE DAMAGE

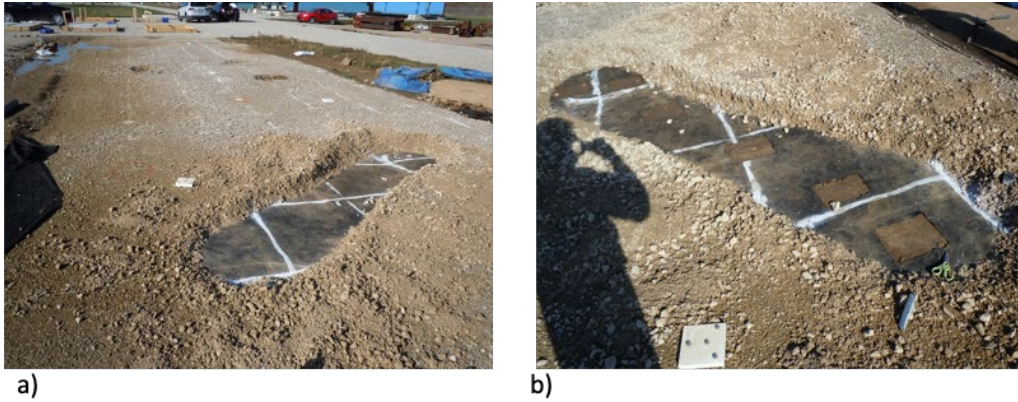


Figure C.1 Sampling trench on untreated strip a) prior and b) after taking samples GX1-GX6 on 11/20/20.

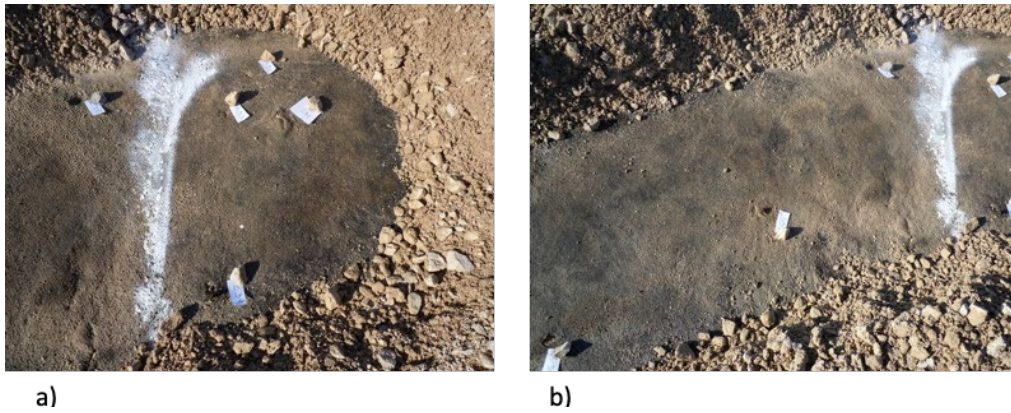


Figure C.2 Identification of damage areas on geotextile on untreated strip.

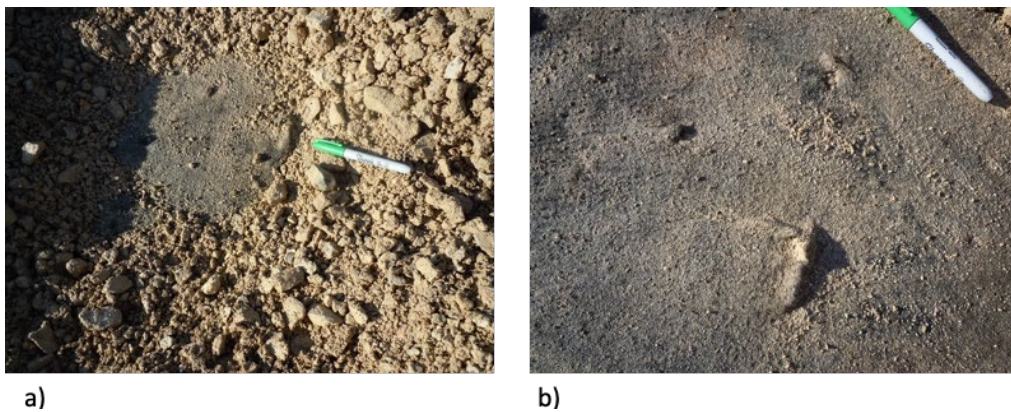


Figure C.3 (a–b) Damage of geotextile at location of cyclic test on untreated strip.

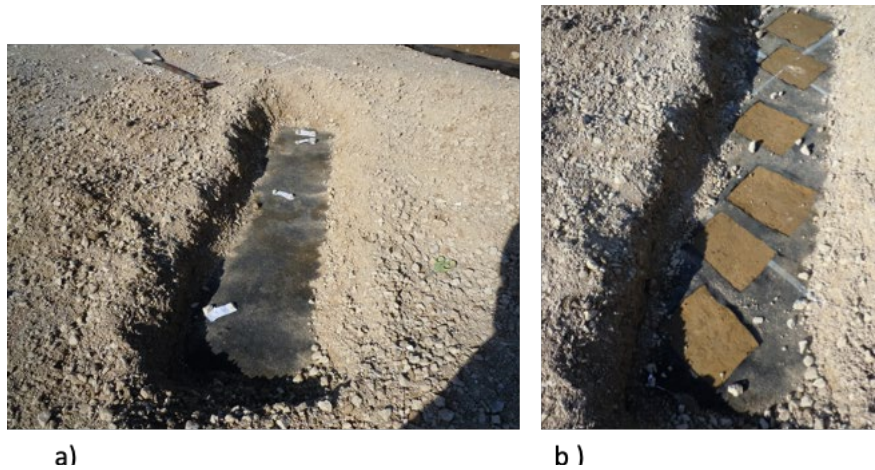


Figure C.4 Sampling trench on cement-treated strip (a) before and (b) after taking samples GX7-GX12 on 11/20/20.

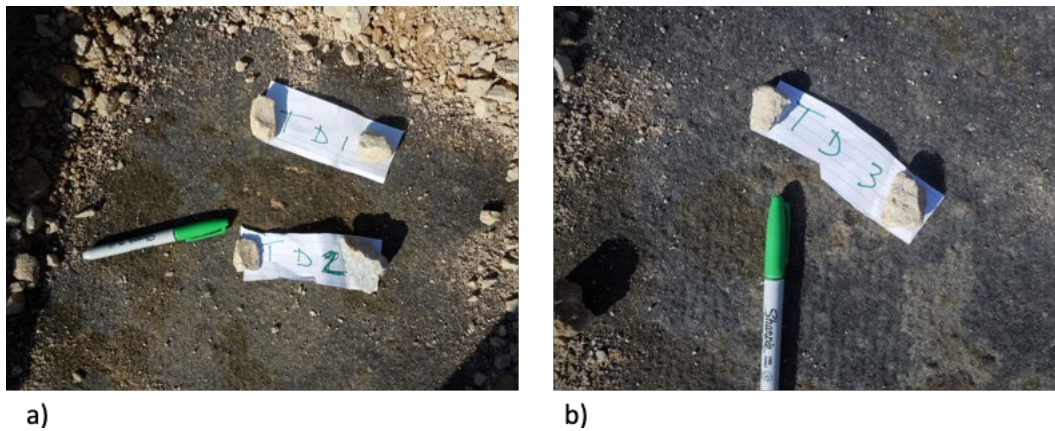


Figure C.5 Identification of damage on geotextile on cement-treated strip (TD# notation refers to damage inventory).

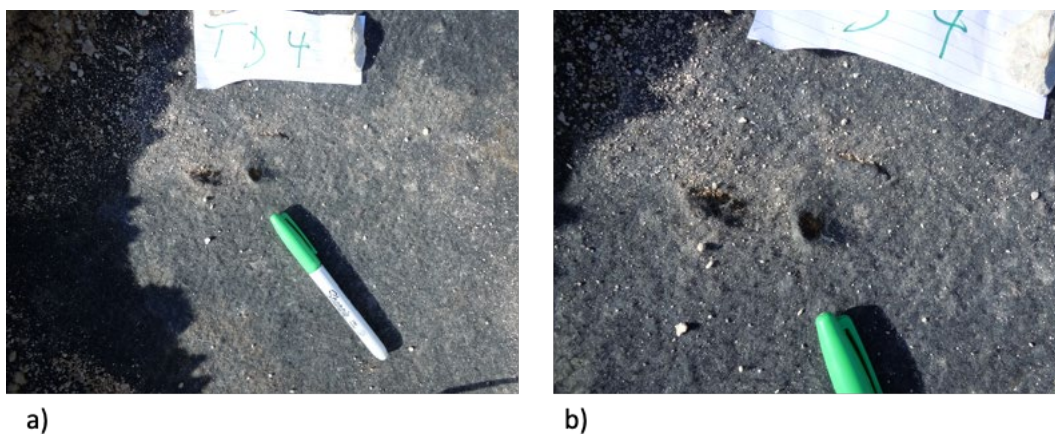


Figure C.6 (a–b) Damage of geotextile at location of cyclic test on cement-treated strip.

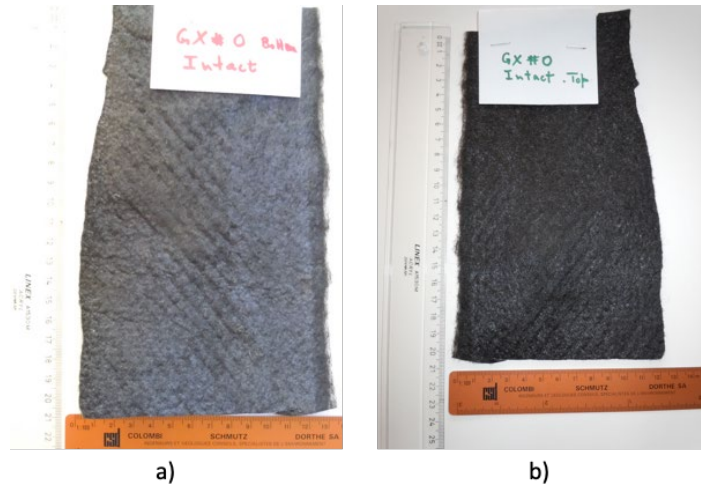


Figure C.7 (a) Bottom and (b) top view of intact geotextile.

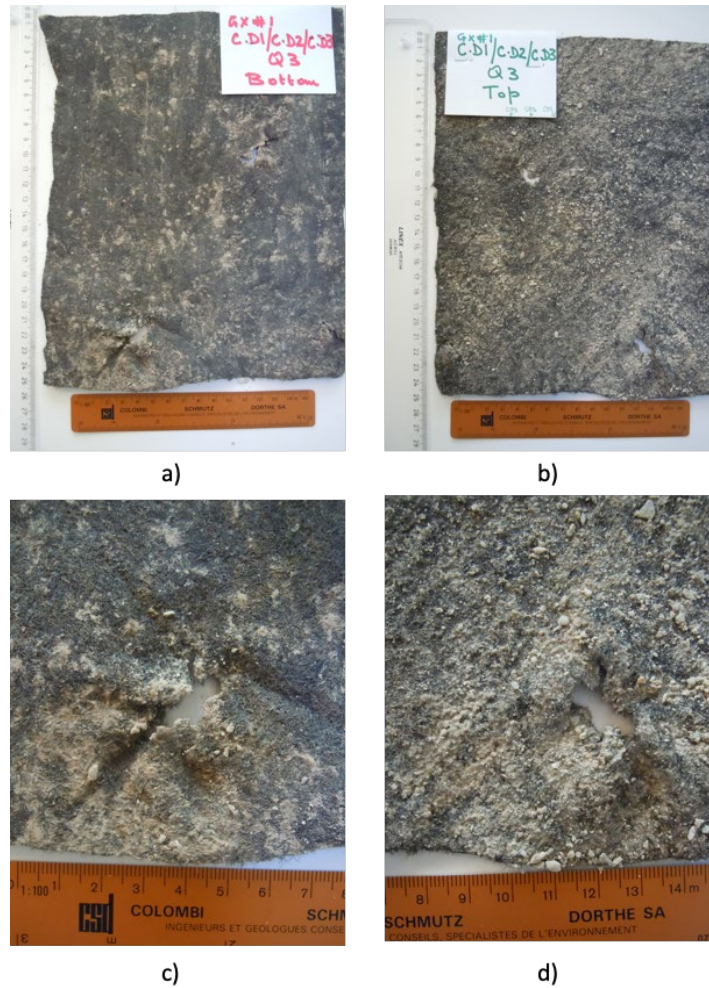


Figure C.8 Sample GX#1 exhumed under location of cyclic test on untreated strip: (a) top (textile face in contact with aggregate); (b) bottom (textile face in contact with subgrade) view; and (c–d) detail of one damage feature (top and bottom view).

Note: In Figures C.8–C.11, the labels indicate sample number, identified damage numbers (CD#), and location on strip and face.

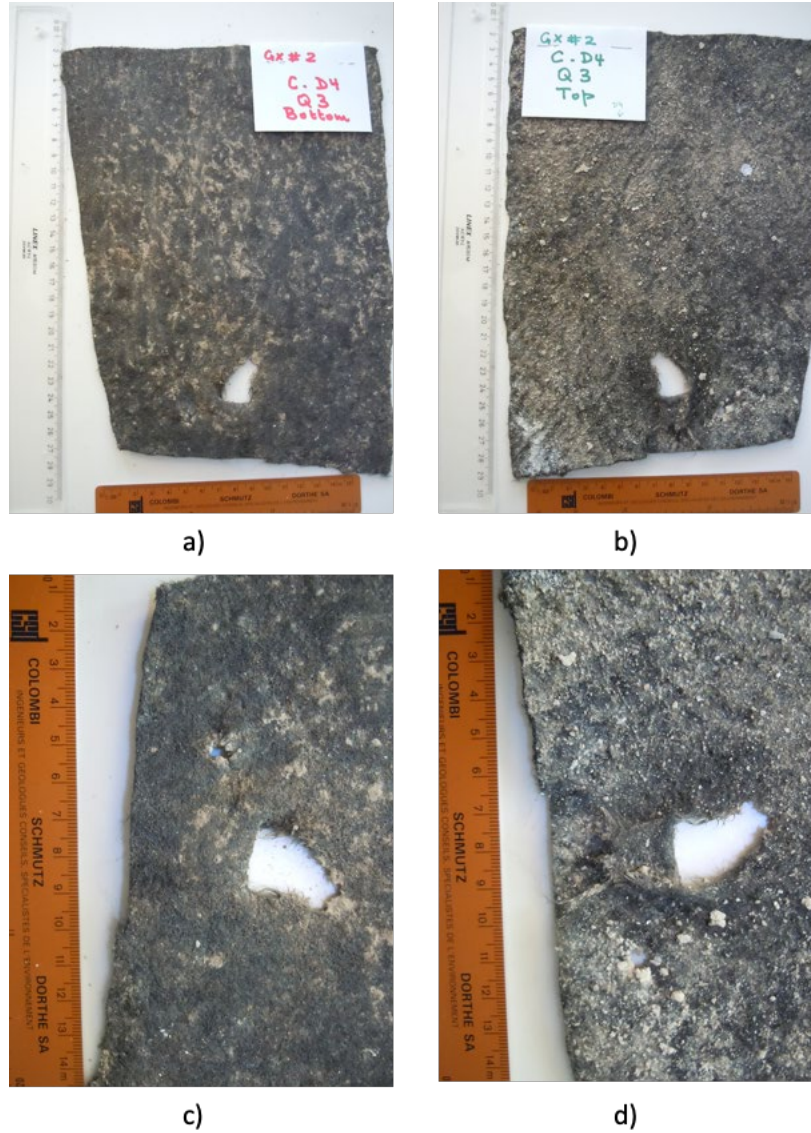


Figure C.9 Sample GX2 exhumed under location of cyclic test on untreated strip: (a) top (textile face in contact with aggregate); (b) bottom (textile face in contact with subgrade) view; and (c–d) detail of one damage feature (top and bottom view).

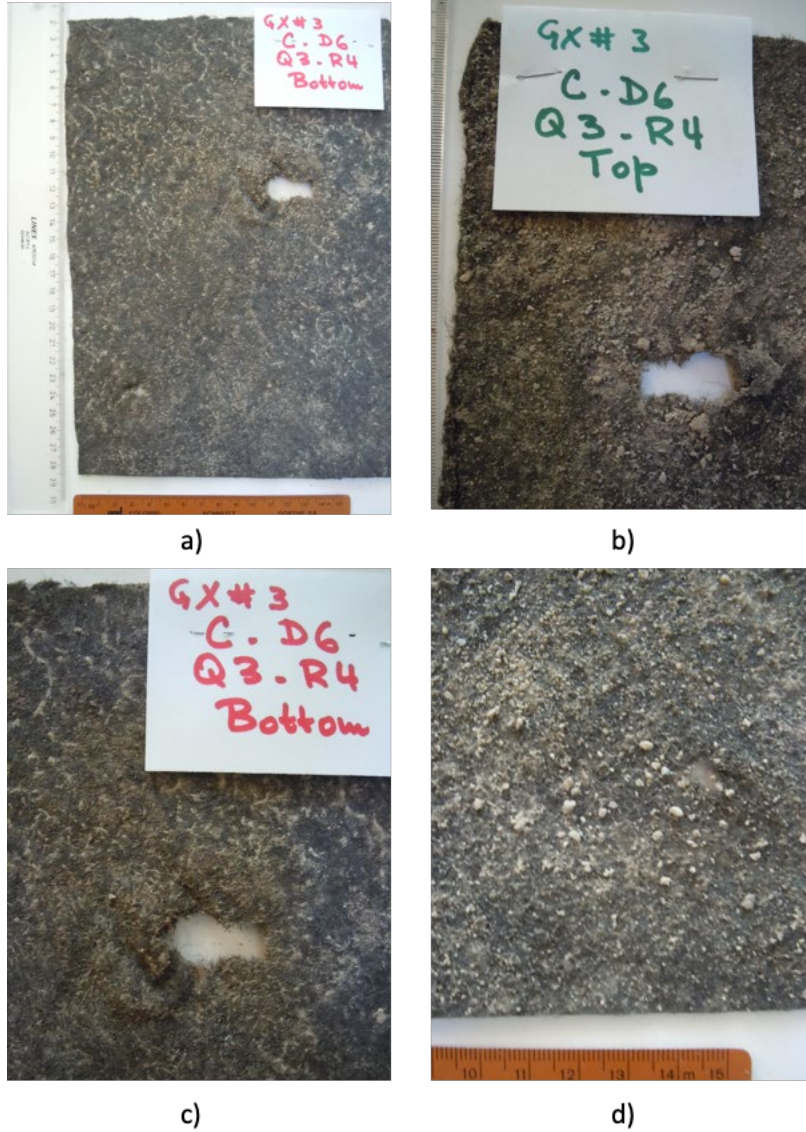


Figure C.10 Sample GX3 exhumed outside of location of cyclic test on untreated strip: a) top (textile face in contact with aggregate); (b) bottom (textile face in contact with subgrade) view; and (c–d) detail of one damage feature (top and bottom view).

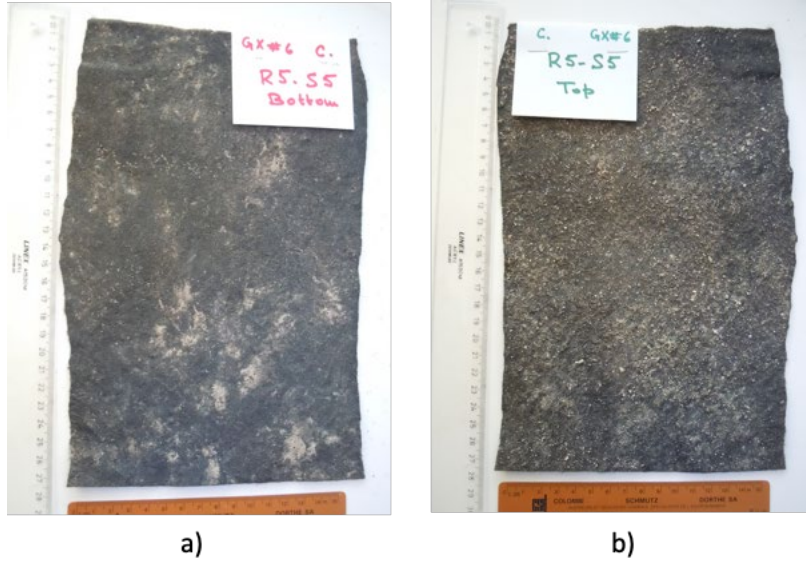


Figure C.11 Sample GX6 exhumed outside of location of cyclic test on untreated strip: (a) top (textile face in contact with aggregate); and (b) bottom (textile face in contact with subgrade) view.

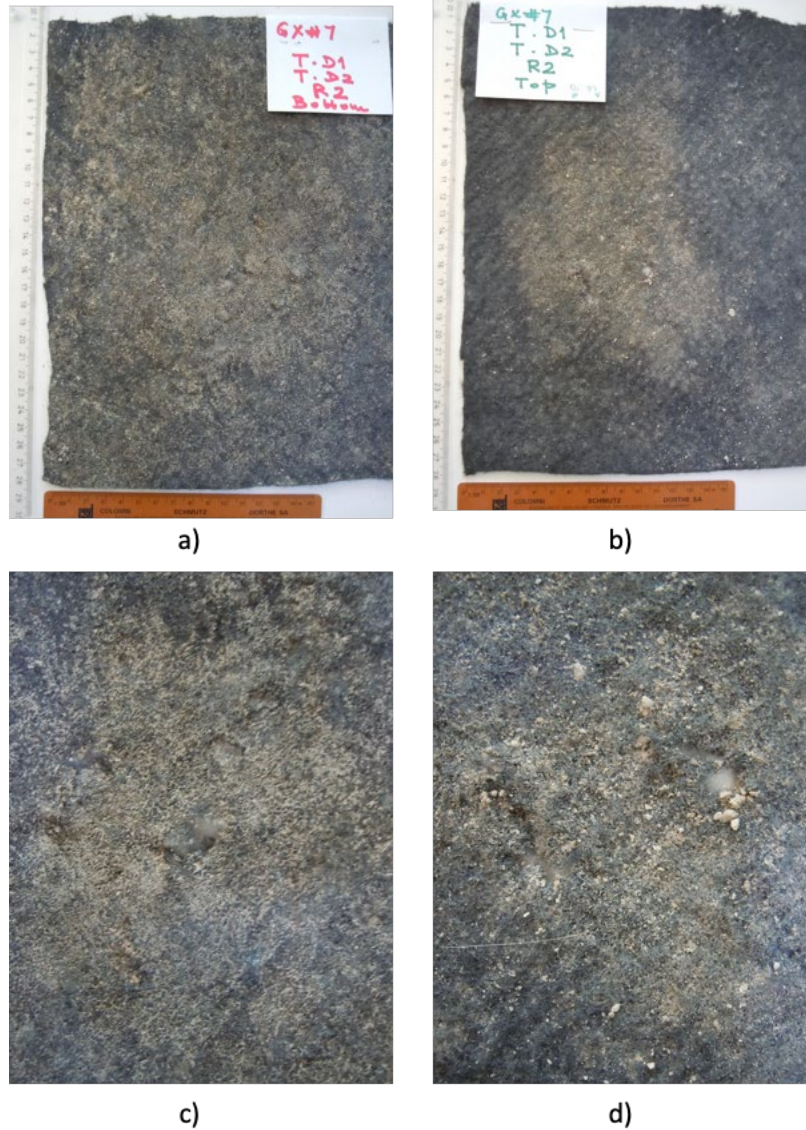


Figure C.12 Sample GX7 exhumed outside of location of cyclic test on cement-treated strip: a) top (textile face in contact with aggregate); (b) bottom (textile face in contact with subgrade) view; and (c–d) detail of one damage feature (top and bottom view).

Note: In Figures C.12–C.16, the labels indicate sample numbers, identified damage numbers (TD#), and location on strip and face.

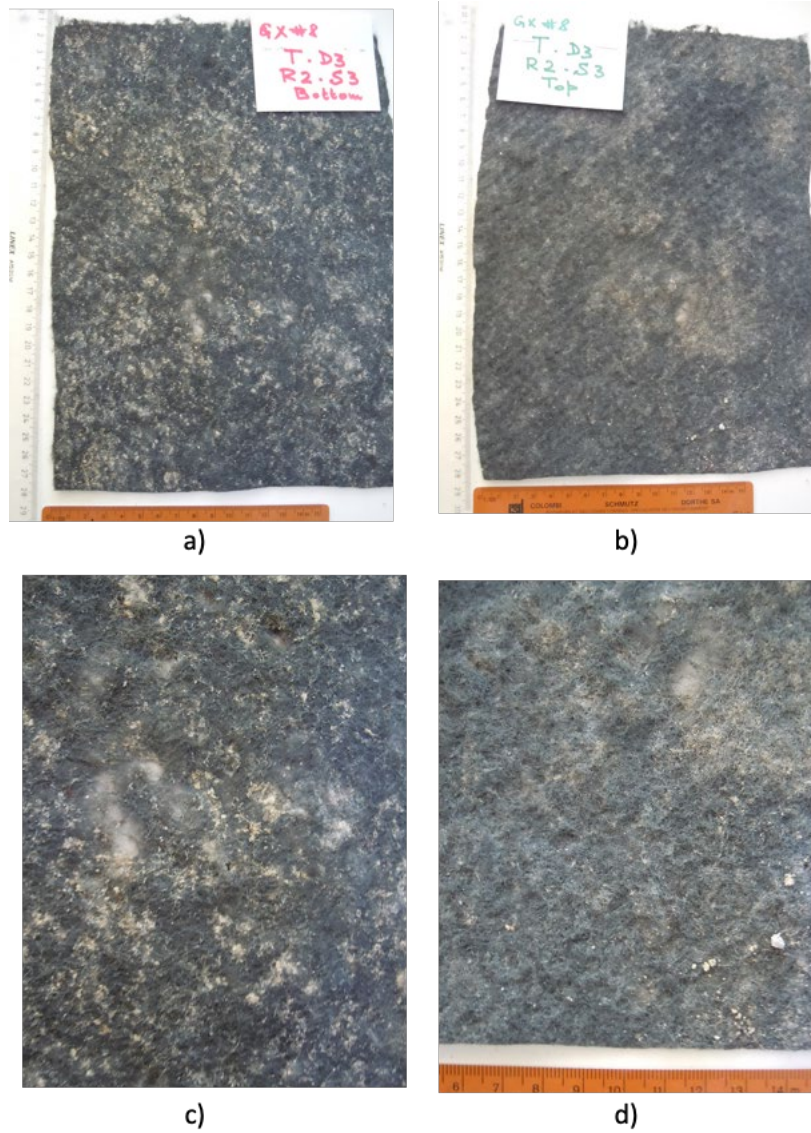


Figure C.13 Sample GX8 exhumed outside of location of cyclic test on cement-treated strip: (a) top (textile face in contact with aggregate); (b) bottom (textile face in contact with subgrade) view; and (c–d) detail of one damage feature (top and bottom view).

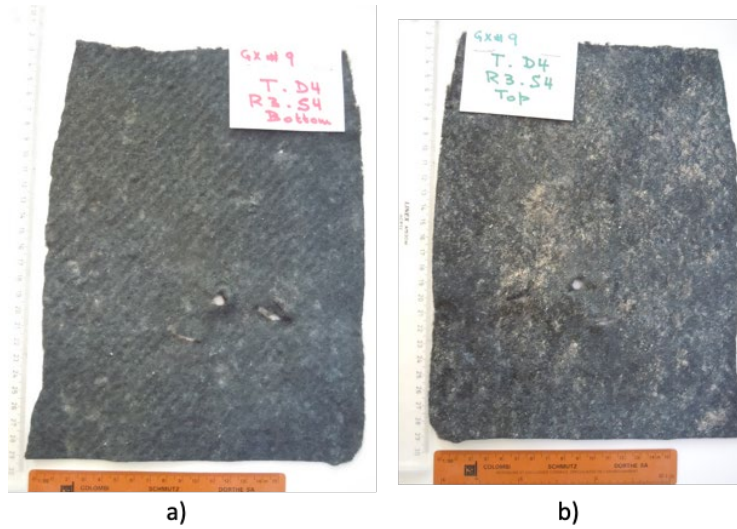


Figure C.14 Sample GX9 exhumed outside of location of cyclic test on cement-treated strip: (a) top (textile face in contact with aggregate); and (b) bottom (textile face in contact with subgrade) view.

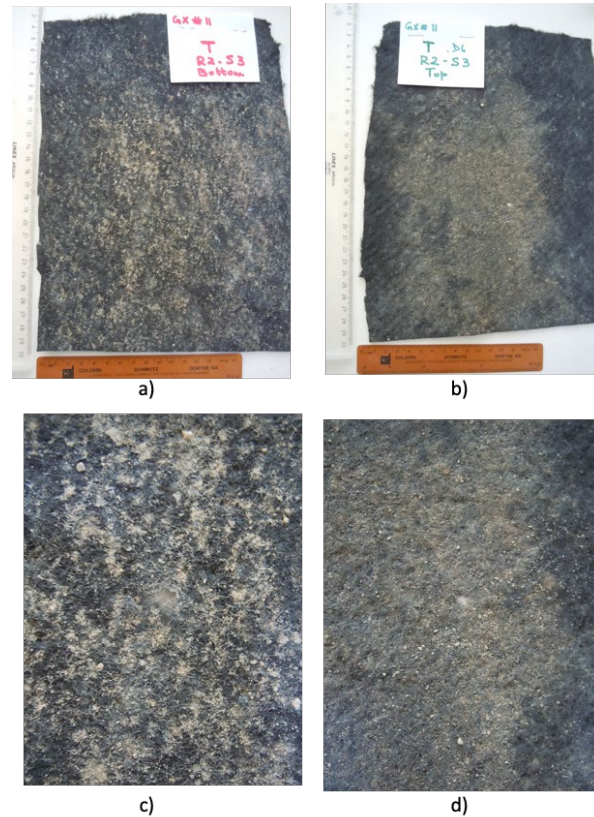


Figure C.15 Sample GX11 exhumed outside of location of cyclic test on cement-treated strip: (a) top (textile face in contact with aggregate); (b) bottom (textile face in contact with subgrade) view; and (c–d) detail of one damage feature (top and bottom view).

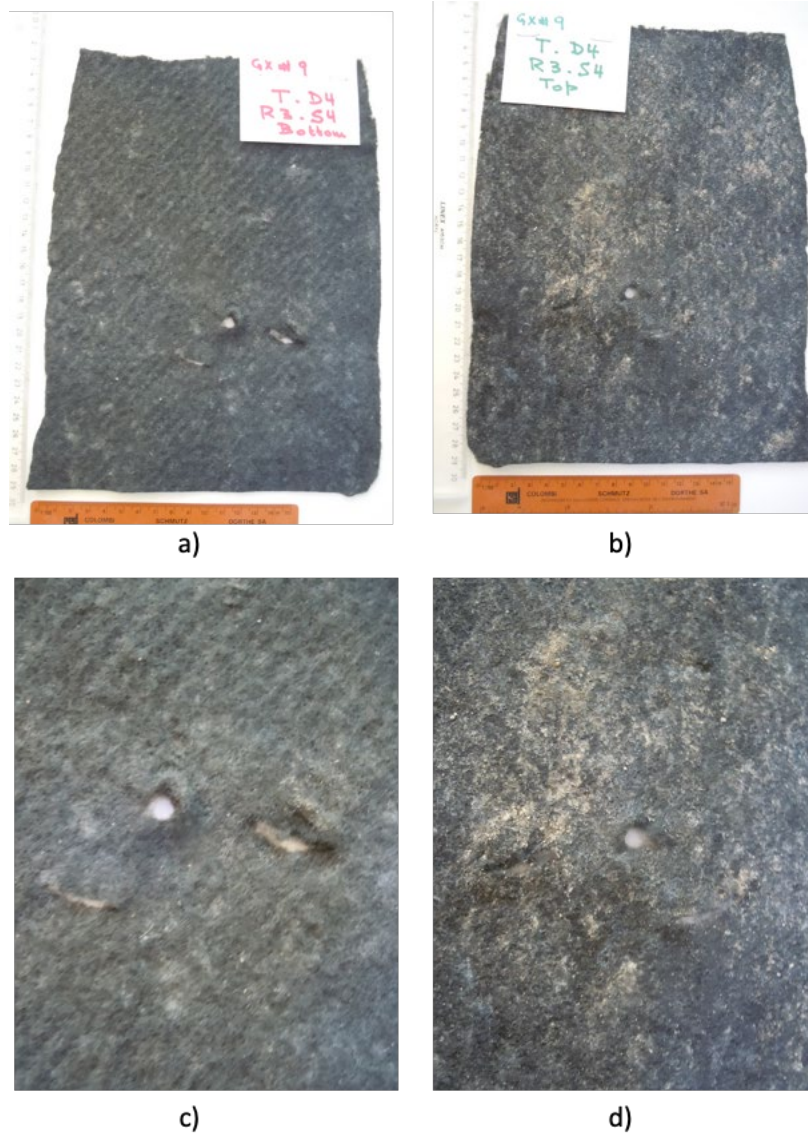


Figure C.16 Sample GX12 exhumed outside of location of cyclic test on cement-treated strip: (a) top (textile face in contact with aggregate); and (b) bottom (textile face in contact with subgrade) view.

About the Joint Transportation Research Program (JTRP)

On March 11, 1937, the Indiana Legislature passed an act which authorized the Indiana State Highway Commission to cooperate with and assist Purdue University in developing the best methods of improving and maintaining the highways of the state and the respective counties thereof. That collaborative effort was called the Joint Highway Research Project (JHRP). In 1997 the collaborative venture was renamed as the Joint Transportation Research Program (JTRP) to reflect the state and national efforts to integrate the management and operation of various transportation modes.

The first studies of JHRP were concerned with Test Road No. 1 — evaluation of the weathering characteristics of stabilized materials. After World War II, the JHRP program grew substantially and was regularly producing technical reports. Over 1,600 technical reports are now available, published as part of the JHRP and subsequently JTRP collaborative venture between Purdue University and what is now the Indiana Department of Transportation.

Free online access to all reports is provided through a unique collaboration between JTRP and Purdue Libraries. These are available at <http://docs.lib.purdue.edu/jtrp>.

Further information about JTRP and its current research program is available at <http://www.purdue.edu/jtrp>.

About This Report

An open access version of this publication is available online. See the URL in the citation below.

Garzon-Sabogal, L., Getchell, A., Becker, P. J., Bourdeau, P. L., & Santagata, M. (2024). *Control guidelines for aggregate drainage layers and evaluation of in-situ permeability testing methods for aggregates* (Joint Transportation Research Program Publication No. FHWA/IN/JTRP-2024/28). West Lafayette, IN: Purdue University. <https://doi.org/10.5703/1288284317769>